Radio frequency exposure analysis in 5G massive MIMO systems

Maarouf Al Hajj

INSTITUT POLYTECHNIQUE DE PARIS

NNT : 2022IPPAT003

Thèse de doctorat

Radio Frequency Exposure Analysis in 5G Massive MIMO Systems

Thèse de doctorat de l'Institut Polytechnique de Paris
préparée à Télécom Paris

École doctorale n°626 École doctorale de l'Institut Polytechnique de Paris (EDIPP)
Spécialité de doctorat : Information, communications, electronique

Thèse présentée et soutenue à Palaiseau, le 13/01/2022, par

MAAROUF AL HAJJ

Composition du Jury :

Philippe De Doncker Professeur, Université Libre de Bruxelles	Président
Laurent Clavier Professeur, IMT Nord Europe	Rapporteur
Christian Person Directeur du Lab-STICC, IMT Atlantique	Rapporteur
Philippe Martins Professeur, Télécom Paris	Examinateur
Lina Mroueh Professeur, Institut Supérieur d'Electronique de Paris	Examinateur
Emmanuelle Conil Ingénieure de recherche, Agence Nationale des Fréquences	Examinateur
Marceau Coupechoux Professeur, Télécom Paris	Examinateur
Joe Wiart HDR, Titulaire de la Chaire C2M, Télécom Paris	Directeur de thèse

Acknowledgements

First of all, I would like to express my sincerest gratitude towards my supervisor Joe Wiart for his support and advice throughout this PhD.

I also thank the ANFR team, and especially Dr. Emmanuelle Conil, for the valuable collaboration during this PhD. The priceless expertise, and the great perspective they shared with me paved the way towards completing this PhD.

My thanks also go towards Prof. Philippe Martins and Prof. Laurent Clavier for evaluating this dissertation. Also to Prof. Lina Mroueh, Prof. Marceau Coupechoux, and Dr. Emmanuelle Conil for examining the dissertation.

Furthermore, I thank Dr. Shanshan Wang for her valuable advice and input, and also my other colleagues that I have known throughout the years at C2M, for their help and support: Amirreza, Bader, Nihal, Seyedfaraz, Sirine, Soumaya, Taghrid, Xi, Yuanyuan, and Zicheng. And to my friends back at home and abroad who are too many to list.

And finally, I am forever grateful to my parents, Sana and Anas, to my siblings, Noema, Hassan, and Mariam, and to my fiancee Maryame, for being by my side throughout this journey.

Abstract

Assessment of electromagnetic field (EMF) exposure is key in the deployment of wireless systems, and it has been grabbing more attention in the context of future wireless systems, mainly fifth generating (5G) and massive multiple-input multiple-output (MIMO) cellular networks. This is due to network densification, high-gain transmitting devices, and usage of high frequencies with higher bandwidth. Both measurement procedures and analytical models are being developed and tested for 5G and massive MIMO wireless networks to properly characterize their induced exposure.

In this dissertation, we estimate and study the EMF exposure in 5G massive MIMO antenna networks. We first present the different characteristics of 5G, relevant to the EMF exposure, specifically the downlink signaling and transmission, and we also present the different measurement procedures to measure the EMF. We show that using current measurement methods, measuring the exposure in a 5G network may result in a significant information loss, due to the large sweep time required to measure the whole 5G band in comparison to the transmission beam allocation. We also show that the 5G synchronization signal block (SSB) can be measured in zero-span, and used to extrapolate its power to the whole bandwidth. However, this signal alone is not sufficient for the estimation of the EMF exposure, due to beam refinement, channel boosting, and multi-user communication.

We then analytically analyze the 5G massive MIMO network in the millimeter wave (mmWave) band by modeling it as a Poisson point process (PPP) and using stochastic geometry tools to determine the total power received which is modeled as a shot-noise process with a modified power law. We fit the mmWave channel model into statistical distributions with data obtained from the NYUSIM channel simulator [1]. The fitted distributions, e.g., exponential and gamma distribution for antenna and channel gain respectively, were then implemented into an analytical framework. We obtain the closed-form expression of the moment-generating function (MGF) for the total power received in the network at the typical MT. The framework is then validated by numerical simulations and a sensitivity analysis is carried out to investigate the impact of key parameters, e.g., BS density, path loss exponent, and transmission probability. We then prove and quantify the significant impact the transmission probability on global exposure, which indicates the importance of considering the network usage in 5G exposure estimations.

And finally we develop a statistical model for both the exposure and the ratio of the exposure to SIR at the nearest MT to its serving BS in a multi-user massive MIMO network deploying MRT and max-min fairness downlink power control. We determine the closed-form expression of the exposure and the expression of the exposure to SIR ratio for MTs being in LoS/NLoS of the BS with LoS probability, p_L. We show that the exposure at the nearest MT to the serving is higher in denser cells, however it decreases with the number of served MTs if the MT density remained constant. It also increases with the number of antenna elements, M due to the increase in the transmission gain. We also show that the exposure strictly increases with the density of the BSs in the network and that the rate of increase is higher in networks with higher p_L in all scenarios. As for the ratio between the exposure and the SIR, we confirm that it increases linearly with the transmit power, and with the BS density, meaning that the exposure increases more than the SIR in these scenarios. However, we show that it decreases with the increase of number of antenna elements in mostly NLoS environments, and that at sufficiently large number of antenna elements, the ratio between the exposure and the SIR would be practically independent from the number of served MTs. This shows that the system is more efficient in terms of coverage considering the EMF exposure in NLoS and less so in increasingly LoS environments.

Résumé

L'évaluation de l'exposition aux champs électromagnétiques (CEM) est de plus en plus importante pour les futurs systèmes sans fil, principalement les réseaux cellulaires de cinquième génération (5G) et les réseaux Multiple Input Multiple Output (MIMO). Cela est à cause de la densification du réseau, des dispositifs de transmission à gain élevé et de l'utilisation de hautes fréquences de transmission. Des procédures de mesure et des modèles analytiques sont développés et tests afin d'assurer une charactérisation précise de l'éxposition des réseaux 5G.

Dans cette thèse, nous estimons et étudions l'exposition aux CEM dans les réseaux 5G massive MIMO . Nous présentons d'abord les différentes caractéristiques pertinentes de la 5G pour l'exposition aux CEM, surtout la signalisation et la transmission de liaison descendante, ainsi que les différentes procédures de mesure CEM. Nous montrons qu'en utilisant les methodes de mesure actuelles, la mesure de l'exposition dans un réseau massive MIMO entraînera une perte d'informations importante, en raison du temps de balayage requis pour mesurer l'ensemble de la bande 5G qui est large par rapport à l'allocation des faisceux de transmission. Nous montrons également que la synchronization signal block (SSB) 5G peut être mesurée à l'aide de mesures zero-span et utilisée pour extrapoler sa puissance pour toute la bande passante. Cependant, ce signal seul ne peut pas être suffisant pour l'estimation de l'exposition aux champs électromagnétiques en raison du raffinement du faisceau, de l'amplification des canaux, et de la communication multi-utilisateurs.

Nous analysons ensuite, analytiquement, le réseau 5G massive MIMO dans la bande des ondes millimétriques (mmWave) en le modélisant comme un processus de point de Poisson (PPP) et en utilisant des outils de géométrie stochastique pour déterminer la puissance totale reçue, modélisée comme un processus de bruit de grenaille avec un loi de puissance modifiée. Nous adaptons le modèle de canal mmWave à des distributions statistiques avec des données obtenues à partir du simulateur de canal NYUSIM [1]. Les distributions sont ajustées à la distribution exponentielle et gamma pour le gain d'antenne et de canal respectivement, et ils ont ensuite été mises en œuvre dans un cadre analytique. Nous obtenons l'expression sous forme fermée de la fonction génératrice des moments (MGF) pour la puissance totale reçue dans le réseau au MT typique. Le cadre est ensuite validé par des simulations numériques et une analyse de sensibilité est

effectuée pour étudier l'impact de la densité des BSs, l'exposant de perte de trajet et la probabilité de transmission. Nous prouvons et quantifions ensuite l'impact significatif de la probabilité de transmission sur l'exposition globale, ce qui indique l'importance de prendre en compte l'utilisation du réseau dans les estimations d'exposition 5G.

Et enfin, nous développons un modèle statistique pour l'exposition et le rapport de l'exposition au SIR au MT le plus proche à sa BS de service dans un réseau massive MIMO multi-utilisateurs déployant maximum-ratio transmission (MRT) et le contrôle de puissance de liaison descendante max-min fairness. Nous déterminons l'expression de forme fermée de l'exposition, et l'expression du ratio exposition/SIR pour les MT étant en LoS/NLoS de la BS avec une probabilité de LoS p_L. Nous montrons que l'exposition augmente avec le nombre de MT desservis, K, en raison de cellules plus denses, et avec le nombre d'éléments d'antenne, M. Nous montrons également que l'exposition augmente strictement avec la densité des BS dans le réseau et que le taux d'augmentation est plus élevé dans les réseaux avec des p_L plus élevés dans tous les scénarios. Nous montrons également que le rapport augmente linéairement avec la puissance d'émission, et avec la densité des BSs, signifiant que l'exposition augmente plus que le SIR dans ces scénarios. Cependant elle diminue avec l'augmentation du nombre d'éléments d'antenne.

Contents

List of Figures

List of Tables

Acronyms

5G fifth generation

BPP binomial point process

BS base station

CCDF complementary cumulative distribution function

CDF cumulative distribution function

CSI channel state information

CSI-RS channel state information-reference signal

DL downlink

EMF electromagnetic field

EPRE energy per resource element

FCC federal communication commission

FD full dimension

fidi finite-dimensional distribution

i.i.d. independent and identically distributed

ICNIRP international commission on non-ionizing radiation protection

IEEE Institute of Electrical and Electronics Engineers

LoS line-of-sight

LTE Long Term Evolution

MGF moment generating function

MIMO multiple-input multiple-output

mmWave millimeter-wave

MRT maximum-ratio transmission

MT mobile terminal

MU multi-user

NLoS non-line-of-sight

NR New Radio

NSA non-standalone

OFDM orthogonal frequency division multiplexing

PBCH Physical broadcast channel

PDF probability density function

PDSCH physical downlink shared channel

PGFL probability generating functional

PL path loss

PPP Poisson point process

PPRE power per resource element

PSS Primary synchronization signal

RAN radio access network

RB resource block

RBW resolution bandwidth

RF radio frequency

SA standalone

SAR specific absorption rate

SCC standards coordinating committees

SIR signal to interference ratio

SSB synchronization signal block

SSS Secondary synchronization signal

TTI transmission time interval

ZF zero-forcing

Chapter 1

Introduction

Contents

1.1 Background

Throughout the last few decades, communication systems have been rapidly evolving with new technologies being developed at an accelerating pace to accommodate the increasing demand on communication technologies [2]. This demand has pushed the industry towards high spectrum usage, paired with an increase of transmitting elements to achieve capacity requirements. However, not only that the transmitting elements are being deployed more densely, but the mechanisms of the new generations of wireless communication systems are significantly different than previous ones [3]. For these reasons, the already existing concerns have increased with regards to the effect of EMF radiation on the public health [4]. Therefore, regulatory bodies, alongside constructors and operators, have already started testing their newly developed antennas for compliance with EMF regulations like what's presented in [5]. Measurement procedures of the EMF exposure have been already put in place to use for older communication systems, however, the fundamental difference between newer and older technologies calls for revisiting these procedures to ensure their reliability [6].

Moreover, cellular networks based on large (macro) base stations are expected to not be sufficient in fulfilling the additional demands of high-data-rate users. Instead, technologies like small-cells and distributed antenna networks, are expected to be deployed, creating ultra-dense networks.

In addition to that, in 5G and beyond systems, new frequency bands, like millimeter-wave (mmWave) bands, are being investigated to exploit their large available spectrum, largely increasing the data rate and capacity of the transmission. However, higher frequency channels have different characteristics than lower frequency ones. Penetration loss, propagation loss, and antenna design will have significant impact on the communication channel at higher frequencies. The effect of these characteristics need to be considered during exposure assessment.

One of the most promising technologies for 5G systems, in mmWave bands, and lower, is massive MIMO antennas. Beamforming, being the act of concentrating the transmitted signal towards the served user is one of the key solutions to meet the demands of future wireless networks and overcome the high path loss of higher frequency bands, however, it proved to be one of the main challenges for EMF regulation bodies. Using a large number of transmitting and/or receiving antennas transforms the omnidirectional radiation of a classical antenna onto a lobe pattern that is both time and space varying. This spatio-temporal variation needs to be accounted for when evaluating the EMF exposure of newer generation systems to ensure its accuracy.

1.2 Objectives and outline

Methods developed in this dissertation serve the purpose of characterizing the downlink exposure in a 5G massive MIMO network. It also serves to analyze the exposure as function of network and MT parameters. This characterization will aid direct the regulatory efforts by giving a more realistic scenario of studying 5G exposure even before its deployment.

Chapter 2 introduces the 5G New Radio (NR) radio access technology and its characteristics relevant for the exposure estimation. We present the massive MIMO array structure which is one of the most prominent technologies for 5G then we discuss the different beamforming techniques for different types of antennas. We also discuss the network architecture, propagation in mmWave frequencies and the physical layer and frame structure alongside the signaling and data transmission channels in 5G.

Chapter 3 presents in-situ measurements of a 5G massive MIMO antenna's downlink transmission using a PXA signal analyzer. We present measurements in the time domain (zero-span), in the frequency domain (spectrum measurement) and in the demodulation domain. We measure the received signal's entire spectrum and also measure the signaling channel separately and show the beam selection process and its mapping to the synchronization signal block (SSB). We show different transmission scenarios and compare them while also discussing the benefits and shortcomings of each measurement method.

Chapter 4 introduces the concepts of stochastic geometry in wireless communication systems. It presents the mathematical background of modeling the base station (BS)s and the MTs as point processes, the different path loss models used, and introduces the essential tools of the mathematical formulation. In it we also present a simple case of determining the closed-form equation of the exposure's distribution in a cellular network.

Chapter 5 addresses the analytical modeling of the total power received in a mmWave massive MIMO 5G network using stochastic geometry. The BSs are modeled following a PPP and the total power received is considered at the typical MT. The mmWave channel was estimated using the NYUSIM mmWave channel simulator and the 3GPP antenna array model, and their values were fitted into statistical distributions then integrated into the framework to get the distribution of the total power. A sensitivity analysis of the power received is also performed to assess the importance of different network characteristics on the exposure.

Chapter 6 investigates both the analytical EMF exposure and its relation to the performance, by considering the exposure to signal to interference ratio (SIR) ratio, of the 5G MU massive MIMO network where the scheduled MTs are being served in the same time-frequency block. The exposure and the SIR in this chapter, however, are considered at the nearest MT to its serving BS, not at the typical MT in the cell. The model considers both LoS and NLoS scenarios and their respective beamforming patterns. We

also consider max-min fairness power control that ensures fair resource allocation between simultaneously scheduled MTs to guarantee equal SIR for all MTs. The expressions of the total power received and the exposure to SIR ratio are then verified and analyzed for different network deployment scenarios.

Chapter 7 concludes the dissertation and suggests future research directions following the work accomplished during this PhD.

Chapter 2

Introduction To 5G New Radio

Contents

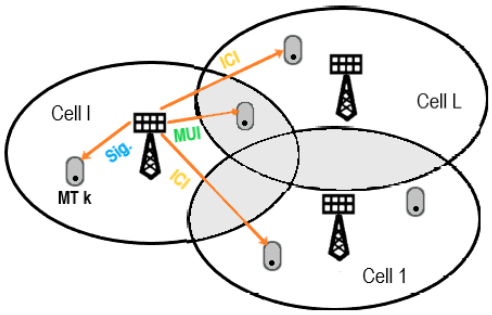

Figure 2.1: Multi-Cell MU MIMO Model

Since 5G networks are fundamentally different than previous generations, it is important to distinguish the differences between them in order to have representative measurements of the EMF. In this section we present and explain the parameters that are necessary in the characterization of the 5G exposure.

2.1 5G massive MIMO

MIMO antenna is a technology in which multiple antenna elements are used at the transmitter and receiver side of the communication channel. Using multiple antenna elements can increase the capability of the RF system by virtue of spatial diversity, spatial multiplexing, or MU transmission.

A MIMO antenna can be called full dimension (FD) MIMO, meaning that it can form beams in both horizontal and vertical directions so it can focus on anywhere in the 3D space. The antenna is basically a rectangular array with dimensions typically 8x8 or more. FD-MIMO is designed to operate in lower frequency bands (sub 6 GHz) [7].

The MIMO is called multi-user (MU), if more than 2 MTs can be served simultaneously. The difference between the already available MU-MIMO and the MU-MIMO for 5G NR systems is that it will be on a much higher scale, thus, massive.

Massive MIMO, also called path-loss MIMO, is an array system with a large set of antennas. The number of antennas required for the system to be called Massive depends on the receiver (equalizer) algorithm. But typically, a system consisting of 64 antennas (8x8) can be considered massive. Massive MIMO is becoming more and more important in both bands of 5G NR deployment (Below and above 6 GHz). It generally aims to serve multiple users in the same time-frequency resource block (RB). When a network is communicating simultaneously with multiple users in a cell, as illustrated in Figure 2.1, the signal would various types of interference from other MTs within the same cell and interference from neighboring cells. Transmission algorithms usually aim to optimize transmission parameters (Tx power, Resource Allocation) for each MTs to maximize the total throughput of a cell.

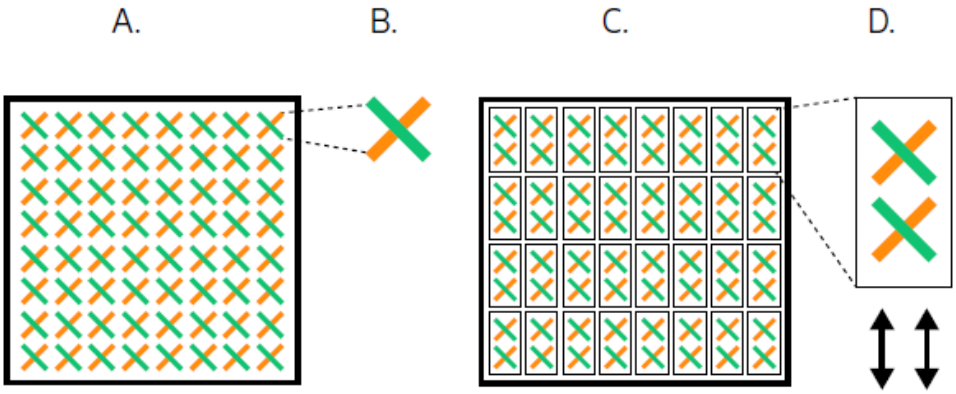

Figure 2.2: Massive MIMO Array Structure [8]

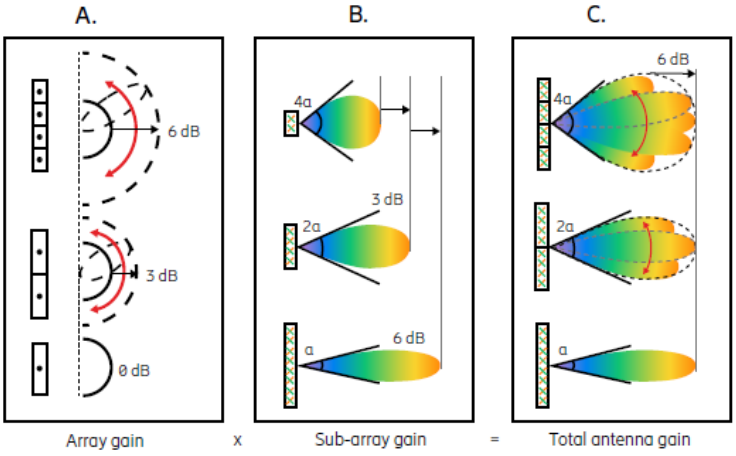

Figure 2.3: Massive MIMO Array Gain [8]

2.1.1 Array structure

The massive MIMO array structure is typically that of a rectangle as shown in Figure 2.2, to enable high gain beamforming and to allow the steering of the beams [8]. The gain is constructed by combining the signals from the different antenna elements. The more antenna elements in the array, the higher is the gain of the beams formed. The offset angle of the beams is formed by controlling the amplitude and the phase of smaller parts of the antenna array. The antenna is divided into sub-arrays (group of non-overlapping elements), and by applying one RF chain per polarization for each sub-array, multiple beams can be formed containing independent data streams.

The total number of elements determines the maximum gain and the sub-array partitioning allows steering of the high-gain beams over the range of angles as shown in Figure 2.3. The sub-array radiation pattern determines the envelope of the narrow beams. It is important to consider the division of the array since extra RF chains impose important additional computational and construction costs.

Even with the same number of served MTs and the same number of Tx/Rx, different modes of implementation can be used. Some of the factors affecting implementation:

1. Number of MTs covered.

2. Number of Tx and Rx antennas used.

3. Receiver design.

4. Precoding algorithm.

Antenna architecture in 5G systems are generally divided into three types, analog, digital, and a hybrid of both. To model the radiation of the antennas, different characteristics affect the radiated power in different ways.

Analog massive MIMO antennas, use phased antenna array elements to create a single steerable beam towards a certain angular direction in the azimuth, elevation, or both. The steering dimensions depend on the antenna construction, which is explained in 2.1.1. Analog massive MIMO also uses a precoding, also called beamforming, codebook [9] as shown in figure 2.21, in which a predefined array of beamforming vectors are stored, and where a vector is chosen based on the estimated channel between the BS and the MT. This channel estimation is performed following a procedure called beam steering, in which the BS sends the signaling frames to all served MTs successively, and on different beams. The BS then estimates the beam that best serves each MT based on a feedback signal from it. The number of precoded beams is not onlt dependent on the antenna's architecture, but also on the numerology that is chosen for transmission. The numerology specifies the sub-carrier spacing, i.e. the separation in frequency between sub-carriers, which affects the number of signaling blocks used when estimating the serving beam. Moreover, the numerology also affect the transmission time interval (TTI), which is the minimal transmission duration between the BS and the MT.

On the other hand, digital and hybrid massive MIMO antennas are more complicated to characterize than analog ones. This type of antennas can simultaneously create multiple beams for each antenna element in the array. The precoded beams are also more likely than not to not be directed, especially in NLoS scenarios. The channel is estimated using uplink pilots sent from the MT and the beams are formed using precoding techniques like zero-forcing (ZF) [10] or maximum-ratio transmission (MRT) [11]. The transmission resources are then distributed according to a power control scheme like max-min fairness. Other characteristics present in analog massive MIMO antennas are also present in digital and hybrid ones, like numerology. Each of these characteristics will be discussed in its own section.

Massive MIMO is not necessarily a way to increase throughput by MIMO/Spatial Multiplexing, but massive MIMO in 5G has the purpose of implementing beamforming to help increase the gain in the direction of transmission and reduce the interference in other directions.

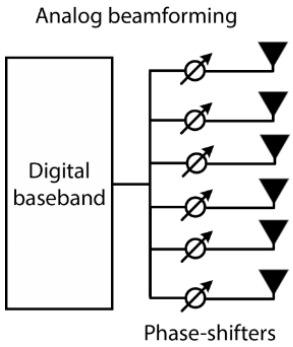

Figure 2.4: Analog Beamformer

The implementation of Massive MIMO/Beamforming is not specified in the 3GPP specifications for 5G NR. The implementation remains up to each equipment constructor/vendor. There are multiple methods for the implementation of massive MIMIO, but it will be most likely the Hybrid mode that will be dominant in the future.

2.1.2 Analog beamforming

Analog beamforming, illustrated in Fig. 2.4, has the advantage of having a simple RF chain for the transmitter system. Lots of antenna test papers and bibliography items focused on the analog transmitters instead of the more complex hybrid. It functions by shifting the phase of the emitted signal in the RF domain at each antenna element to create an effect similar to a phased antenna array and thus changing the directivity/pattern of the antenna.

Analog beamformers are limited in terms of beamforming, they have fixed precoded beams and can emit only one beam per time slot. Some research suggests that analog beamforming will be used for one dimensional sweeping and transmission and for implementations with a lower number of beams (<6 GHz). But in the previously mentioned papers, Ericsson has performed its measurements in 14.5, 15.2 GHz [12] and 28 GHz [13].

2.1.3 Digital beamforming

In digital beamforming (also known as precoding), illustrated in Fig. 2.5, the signals are shifted in phase/amplitude in the baseband before the RF transmission which requires an A/D converter for each element, making a full high dimension digital massive MIMO expensive to implement. Amplitudes and phases and also frequency bands (subcarriers) can be assigned to each antenna element thus enabling higher flexibility. Digital beamforming is particularly desirable for spatial multiplexing where the system transmits a superposition of signals with different directivities (channel conditions) especially in wideband scenarios (frequency-selective fading). The two most popular precoding methods

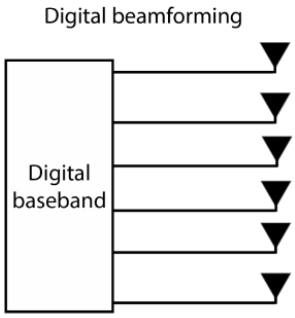

Figure 2.5: Digital Precoder

are zero-forcing and maximum ratio processing.

Zero-forcing, also called null-steering, nominally eliminates the multi-user interference among the multiplexed signals in a multi-user MIMO. In the condition of perfectly-known CSI at the transmitter, the precoding matrix can be expressed as the pseudo-inverse of the channel matrix [10]. As a general rule, an antenna having N elements, can create N-1 independent nulls in the radiation pattern.

As for maximum ratio processing, also called maximum-ratio transmission (MRT) [11], is an implementation of the maximum-ratio combining technique used at the receiver side to exploit diversity. MRT aims to maximize the power received at the MT by exploiting channel diversity. This can be explained by focusing the transmit power in specific directions so that it adds up at the receiver. in LoS, it can be equated to analog beamforming where the transmitted power is directed towards the LoS path.

2.1.4 Hybrid Beamforming

Hybrid beamforming can allow, at the cost of a more complex system, the formation of multiple transmission beams while maintaining a level of multiplexing/multiple access. The power emitted from the antenna is divided by the beams formed. Typically, and as seen in some presentations by constructors/operators, the hybrid antennas can have up to 8 transceiver units (TXRUs) in the case of cross polarization [14] and 4 TRXUs when using a single polarization [15], to emit simultaneously to four MTs in the case of MU-MIMO, or transmit four beams to a single MT in the case of SU-MIMO, or one beam per panel, and will be most likely used for applications in the spectrum above 6 GHz [15].

In over-6 GHz channels, antennas are usually separated into multiple, widely separated, panels. And the characteristics are not in specifications and can vary depending on the constructor.

2.1.5 Beam management

The defining characteristics of the 5G NR and its challenges reside in its deployment in the mmWave frequency band (while its deployment in sub 6 GHz is possible and very likely). The management can be separated into multiple parts depending on the state of connection (cell search/initial access, connected state...). Beam management for specific connection phases are explored in its own sections. Here is the discussion of the general idea. The most general scenarios for BS-MT connection, illustrated in figure 2.6 can be summarized by four examples:

1. MT and Network are connected through a single TRP (Tx/Rx Point) and a single beam.
2. MT and Network are connected through multiple TRP (Tx/Rx Point) and a single beam for each TRP.
3. MT and Network are connected through a single TRP (Tx/Rx Point) and multiple beams
4. MT and Network are connected through multiple TRP (Tx/Rx Point) and multiple beams for each TRP

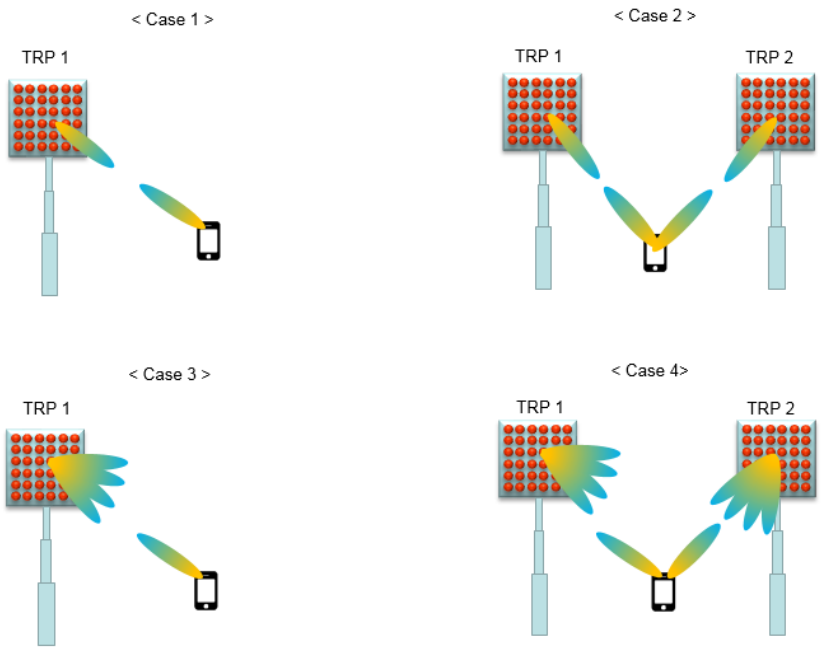

Figure 2.6: 5G BS-MT Connection scenarios [16]

2.2 5G network

Generally, the network will either be homogeneous where 4G and 5G cells are co-located or heterogeneous where 5G will be deployed on small cells managed by the 4G network (or vice versa) as shown in figures 2.8, 2.9, and 2.10. The exposure in a network is affected mostly by network structure and density, the type of antennas used in the network and the distribution and density of the MTs.

The densification of the network will undoubtedly result in an increase in the total received power and consequently the exposure. However, it is important to estimate the effect this densification on the total received power, especially since the network will have many small cells being added. The same behaviour can be expected by increasing the number of antenna elements on the serving BS which has to be also studied.

5G NR networks can be deployed as standalone (SA) and non-standalone (NSA). The first phase of 5G deployment will be the NSA, where the 5G connection will be dependent on the already established Long Term Evolution (LTE) network. Regarding cell layout, there are two general cases of deployment, homogeneous and heterogeneous.

NSA NR is a deployment method of NR in its early stages, when it's dependent on the already present LTE network. The MT communicates with both LTE eNB and NR gNB in the site. While the LTE core network is used for signaling/data, the gNB and eNB will use each their own PHY/MAC layer. The overall network architecture will be equivalent to Figure 2.7. In NSA, the MT communicates with the gNB for data-throughput improvement (User Plane) but still use 4G for control and signaling (Control Plane).

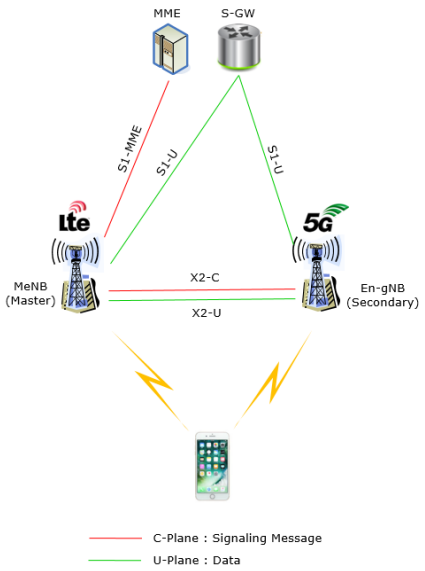

Figure 2.7: Non-standalone 5G Network [17]

Even though the gNB will be dependent on the LTE core, the radio interface should

not be any different from the standalone deployment. The difference in the radio interface between the standalone and the non-standalone deployment of NR can be introduced if each deployment used different frequency bands (sub 6 GHz for NSA and mmWave for SA) which can heavily affect the usage of the radio channel.

Homogeneous deployment, presented in figure 2.8, is when LTE, and NR cells cover the same areas. This also implies that the NR and LTE systems are operating in the same frequency bands and have co-located cells.

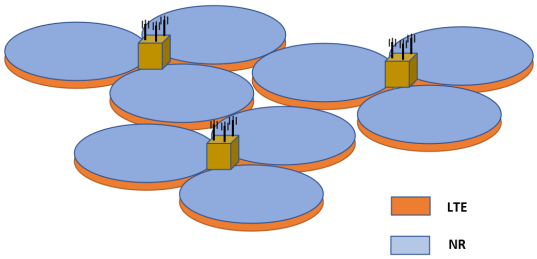

Figure 2.8: Homogeneous deployment of the 5G network

Heterogeneous deployment, presented in figures 2.9 and 2.10, has two scenarios, NR small cells, or NR macro cells. In this kind of deployment LTE cell is large cell size to meet coverage requirement while NR cell size is small to meet the capacity requirements. Here the NR cell can be deployed as a co-located cell or a non-located cell as a hot spot.

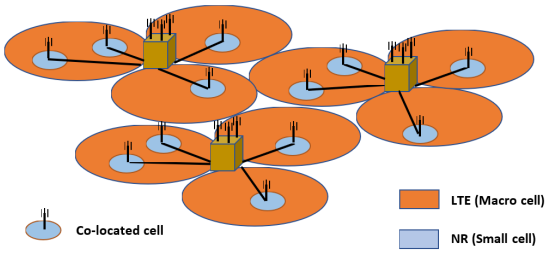

Figure 2.9: Heterogeneous 5G Network with NR Small Cells

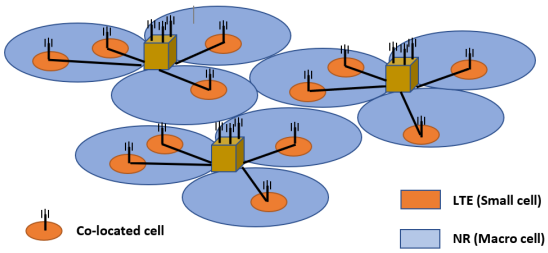

Figure 2.10: Heterogeneous 5G Network with LTE Small Cells

The illustration in Figure 2.11 highlights the three basic deployment scenarios: Dense urban high-rise, Urban low-rise, and rural environments.

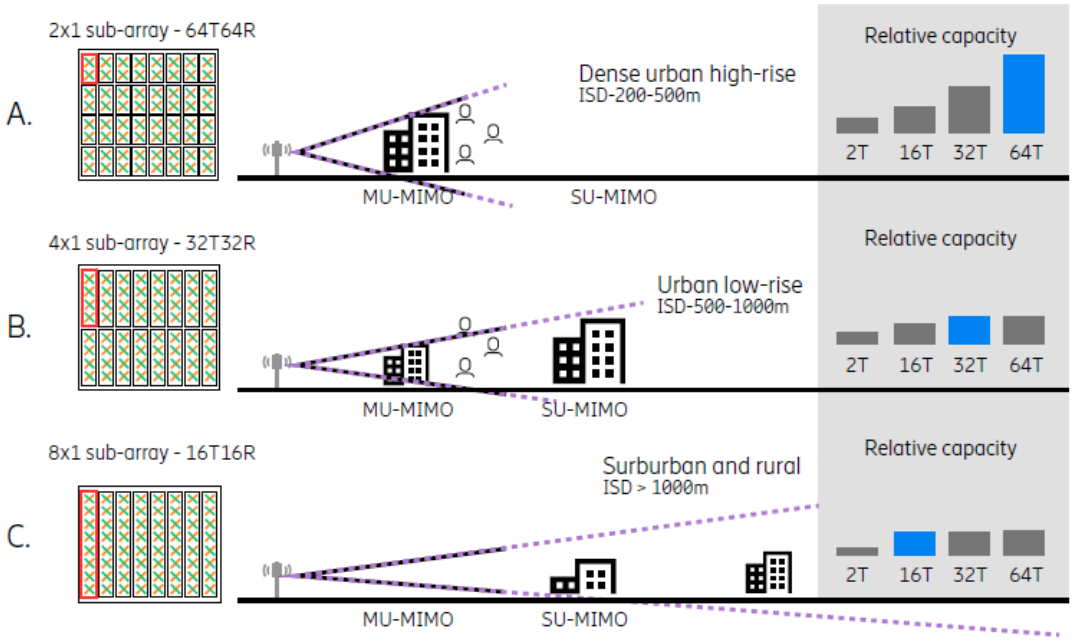

Figure 2.11: Massive MIMO Deployment Scenarios [8]

Dense urban environments are characterized by high-rise building and high BS density of 2×10^{-3}-5×10^{-3}. They are also characterized by the large traffic volume due to high MT density and MT spread in the vertical plane. This requires small sub-arrays with wide beams in the vertical direction, which produces high-gain beams that can be steered over a large range of angles. This also means that the antenna should have a sufficiently large number of RF chains to support all the sub-arrays. A proposed architecture is to have 64 radio chains controlling the sub-arrays.

The urban scenario represents most of the cities worldwide, including the outskirts of dense urban cities. Base stations are typically deployed on rooftops and are separated by few hundred meters. Traffic per unit area is lower than dense urban scenarios. And since the heights of the buildings is lower than dense urban, it allows larger vertical subarrays meaning fewer radio chains are required. Reciprocity-based beamforming schemes will work for most users, but there will be users with poor coverage that need to rely on techniques such as feedback-based beamforming. MU MIMO is also appropriate at high loads due to the multi-path propagation environment, good link qualities and MT pairing opportunities.

In rural and suburban environments, antennas are mounted on rooftops of on towers and separated by few kilometers. Low or medium population density and very small vertical MT distribution. This scenario calls for an antenna with a large area and supporting horizontal beamforming. Since the vertical distribution of users is very small, vertical beamforming does not provide significant gains and large antenna subarrays with small vertical coverage are suitable. In this scenario, MU-MIMO gains are less important.

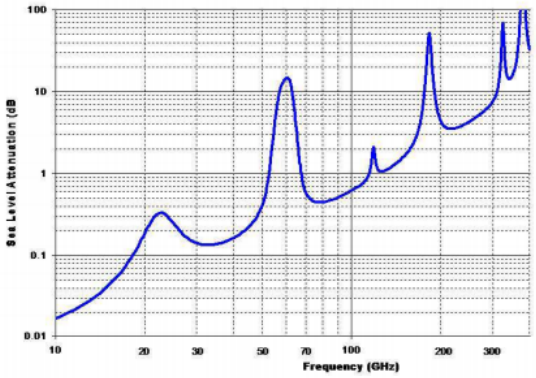

Figure 2.12: Atmospheric and molecular absorption in mmWave [18]

2.3 Millimeter wave Communications

Millimeter wave is the EM wave having a wavelength into the scale of millimeter (10 $\sim$ 1 mm or 30 GHz $\sim$ 300 GHz). The actual range of frequencies of the millimeter wave signals is not clearly defined, so the waves with frequencies $>$ 20 GHz can also be considered in the mmWave band. mmWave communication systems have fundamental differences from their RF counterparts which impose challenges in the physical, MAC and routing layers of mmWave communications.

mmWave signals suffer from big propagation loss compared to signal with lower carrier frequencies in addition to rain attenuation and atmospheric absorption as shown in figures 2.12 and 2.13. Smaller cell sizes are being deployed to combat the effect of rain attenuation and atmospheric absorption. NLOS channels also suffer more attenuation from atmospheric absorption than LOS. To combat the severe path loss in mmWave propagation directional antennas at both the transmitter and receiver are being used.

Moreover, electromagnetic waves don't have the ability to diffract around objects with sizes significantly larger than its wavelength. For this reason, waves in the 60 GHz band are susceptible to blockage by obstacles like humans and furniture.

On the other hand, the small wavelengths of mmWave signals allows the construction of antennas with a large number of elements, and by controlling the phase at each (or some) elements of the array, the direction of propagation of the antenna can be steered towards the desired direction of emission creating high gains towards the served MT, while having lower gain towards the interferers. The directivity of the transmission reduces the interference between the MTs in the cell, and also reduces inter-cell interference. However due to the fast growth of connected and IoT devices being deployed, especially in indoor environments, interference becomes a large problem to manage.

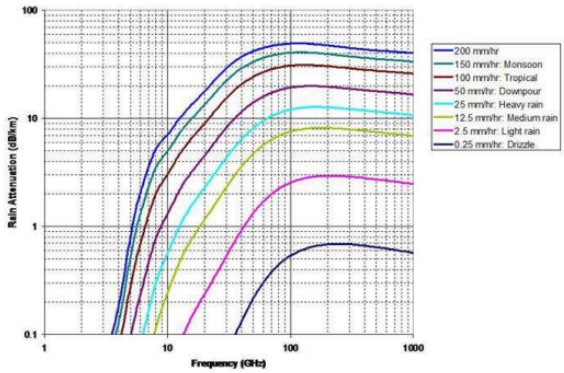

Figure 2.13: Rain attenuation in mmWave [18]

μ	f=2^{μ}.15 $[KHz]$	Cyclic Prefix	Supported for Data	Supported for Sync
0	15	Normal	Yes	Yes
1	30	Normal	Yes	Yes
2	60	Normal, Extended	Yes	No
3	120	Normal	Yes	Yes
4	240	Normal	No	Yes

Table 2.1: 5G Numerology

2.4 Physical layer

2.4.1 Numerology

NR operates in two frequency ranges, FR1 (450 MHz – 6 GHz), and FR2 (24.25 GHz – 52.6 GHz)- millimeter wave. Scalable and flexible frame structure is a key to implement the NR deployment in such broad and diverse spectrum. Numerology is a new concept created in the 3GPP specifications for NR and its most representing of the subcarrier spacing in the 5G frame [19]. In LTE, this terminology was not necessary because there was only one subcarrier spacing (15 KHz), while in NR there are multiple subcarrier spacings that can be used. The supported numerologies are summarized in Table 2.1, timings and durations in Table 2.2 and number of slots in Table 2.3.

Subcarrier Spacing	15 kHz	30 kHz (2 ×15 kHz)	60 kHz (4 ×15 kHz)	15×2^nkHz($n = 3, 4, \dots$)
OFDM symbol duration	66.67 μs	33.33 μs	16.67 μs	$66.67/2^n$ s
Cyclic prefix duration	4.69 μs	2.34 μs	1.17 μs	$4.69/2^n$ s
OFDM symbol including CP	71.35 μs	35.68 μs	17.84 μs	$71.35/2^n$ s
Number of OFDM symbols per slot	7 or 14	7 or 14	7 or 14	14
Slot duration	500 μs or 1,000 μs	250 μs or 500 μs	125 μs or 250 μs	$1,000/2^n$ s

Table 2.2: 5G Physical Layer Duration per Numerology

As shown in Table 2.1, not every numerology can be used for every physical channel and signals, though most of the numerologies can be used for both. The multiple numerologies (subcarrier spacings) are motivated by the changing characteristics of the 5G channel depending on the operation frequency (sub 6 GHz or mmWave).

μ	N_{Symb}^{Slot}	N_{slot}^{frame}	$N_{slot}^{subframe}$
0	14	10	1
1	14	20	2
2	14	40	4
3	14	80	8
4	14	160	16

Table 2.3: Number of Frames and Slots in 5G per Numerology

2.4.2 Frame structure

Depending on the numerology used, the slot changes in length. Lower subcarrier spacing will result in the orthogonal frequency division multiplexing (OFDM) symbols being closely positioned in the time domain. And since the number of OFDM symbols is fixed in a slot (14 symbols/slot for normal CP, and 12 symbols/slot for extended CP) at all the numerologies, the slot duration gets lower with wider subcarrier spacing. However, the duration of the radio frame does not change (10 ms).

The main differences between the legacy LTE TDD Subframe configuration and the NR slot configuration are [20]:

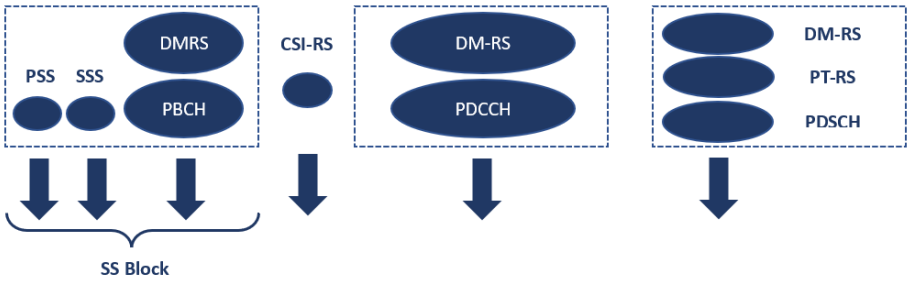

Figure 2.14: 5G Downlink Channel Mapping

1. In NR, the DL/UL assignment changes at symbol level compared to assignment at subframe level in LTE

2. Slot format patterns in NR are much more diverse than LTE.

3. Symbol assignment for NR can be UL, DL, or flexible.

The resource grid for NR is almost identical to the LTE resource grid but differs in its physical dimension (i.e. Subcarrier spacing, number of OFDM symbols per frame) since the dimension in NR is depending on the numerology. A slot is typically the unit for transmission used for scheduling, but in NR the system has the ability to start and end the transmission at any OFDM symbol (non-slot based scheduling) necessary and can utilize mini-slots that can occupy 2, 4 or 7 OFDM symbols to facilitate very low latency for critical data transmissions and minimize interference [21]. The Transmission Time Interval (TTI) can be considered as the slot duration as considered in [12]; in the paper the TTI is considered as the duration of the subframe. However, in the 3GPP specifications, the duration of the subframe is constant and the duration of the slot is the one dependent on the numerology/SCS. The 5G NR channel mapping is presented in Figure 2.14.

2.4.3 Duplexing

The duplexing schemes supported in NR are Frequency Division Duplex (FDD), Time Division Duplex (TDD) with semi-statically configured UL/DL configuration, and Dynamic TDD. For TDD operation, each OFDM symbol in a slot can be configured as DL, UL, or flexible. Where a symbol configured as flexible can be used in either DL or UL operations. The allocation of UL and DL symbols happens in cell-specific and MT-specific Radio Resource Control (RRC) configurations. Dynamic TDD is the case where there is no configuration for the slot and all the symbols are defaulted to flexible and whether the symbol is used for UL or DL can be dynamically determined according to layer 1/2 signaling of DL control information (DCI) [21].

2.4.4 Synchronization signal block (SS/PBCH block)

In LTE, the signaling block had only one pattern of transmission. While in NR, the transmission pattern of SSB is more complicated as it depends on different parameters (numerology, frequency range...) as illustrated by Figure 2.15. While the SSB set is always sent in the first half frame (first 5 ms), its periodicity is not fixed. The SSB set period can be {5, 10, 20, 40, 80, 160 ms}. An SSB is mapped to 4 OFDM symbols in time and 240 subcarriers (20 RBs) in frequency. The location of the SSB in the frequency domain is also flexible, but in its default, it is mapped to the center frequency. Figure 2.14 shows the mapping between the logical, transport, and physical channels in 5G NR. The SSB is contains three different physical channels:

Primary synchronization signal (PSS) at symbol zero and occupies 127 consecutive subcarriers. It is used for downlink frame synchronization.

Secondary synchronization signal (SSS) at symbol two and occupies 127 consecutive subcarriers. And also used for frame synchronization.

Physical broadcast channel (PBCH) at symbols one, two and three, and occupies 240 consecutive subcarriers in symbols one and three each, and ninety-six in symbol two. Its used mainly to broadcast the master information block (MIB).

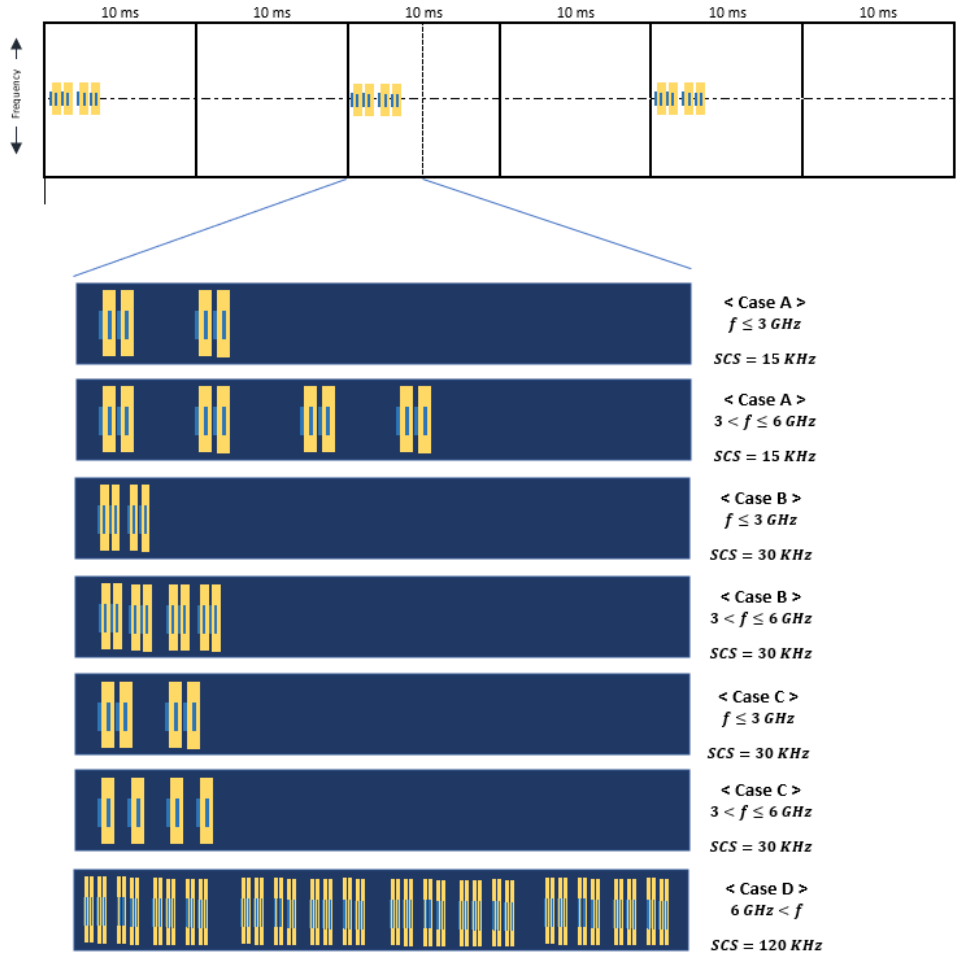

Figure 2.15: 5G SSB Structure per Numerology

Beam sweeping (Idle state)

The SSB plays a crucial role in beam management and resource allocation, as part of the beam sweeping procedure. Beam sweeping is implemented by assigning each SSB to a specified beam. The beams carrying the SSB are swept in time and transmitted towards MTs on different locations in the coverage area at regular intervals based on a set periodicity {5/10/20/40/80/160 ms}. Beam sweeping procedure is illustrated in the figure below.

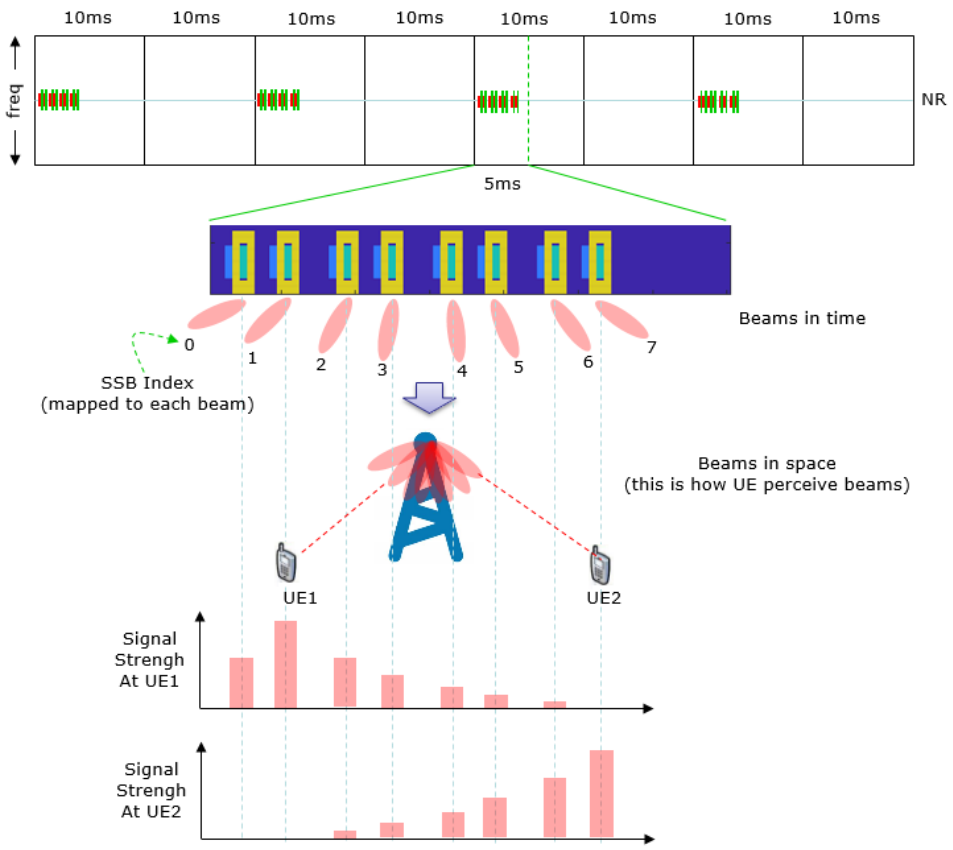

Figure 2.16: Beam Sweeping [16]

Each SSB is identified by a unique number called SSB index. MTs located in the coverage area around the gNB receive the SSBs and measures the signal strength of each SSB. Each MT then selects its preferred beam as a result from its measurements and communicates it back to the gNB. We note that the number of beams in the sweeping procedure is directly related to the number of SSBs in an SSB set which is also directly related to the numerology and frequency of operation used by the gNB. The maximum number of SSBs in a set (max number of beams) is called L_{max}. We can conclude, from the predefined numerologies discussed above, that for sub 6 GHz frequencies L_{max} can be either 4 or 8 and can be swept in one dimension only, while in mmWave it is 64 and can be swept in two dimensions.

2.4.5 Channel state information - reference signal

Like in LTE, channel state information-reference signal (CSI-RS) reporting is used in connected mode to regularly estimate the channel conditions for mobility management purposes. The CSI-RS spans {1, 2, 4} OFDM symbols and they are transmitted following one of two modes: periodic, semi-persistent/aperiodic. The CSI-RS is a downlink signal sent by the gNB and multiple CSI-RS can be configured to the same SS burst. CSI-RS is also used for beam management purposes in sub 6 GHz for analog beamforming. In the

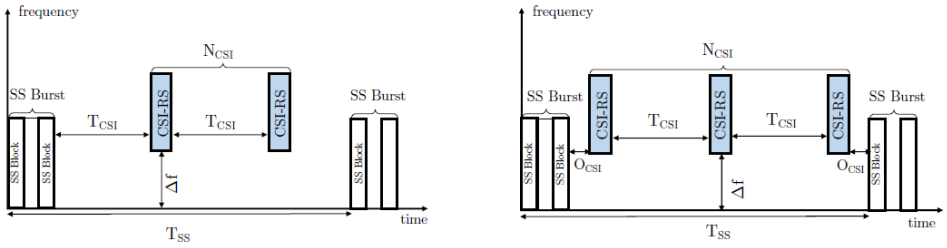

(a) Option 1: the first CSI-RS is sent T_{CSI} ms after an SS burst.

(b) Option 2: the first CSI-RC is sent O_{CSI} ms after an SS burst.

Figure 2.17: Periodic and Aperiodic CSI-RS [23]

downlink, for analog massive MIMO systems, there are multiple schemes that can be used for beam management either replacing SSB based beam management or complementing it [22].

Single CSI-RS Analogous to LTE Class A, the CSI-RS may or may not be beamformed an its typically intended for arrays having 32 TXRUs or less with no beam selection (no CRI). Its process is for the gNB to transmit the CSI-RS to the MT that in turn computes and sends the Rank Indicator (RI)/ Precoding Matrix Indicator (PMI)/Channel Quality Indicator (CQI) to the gNB.

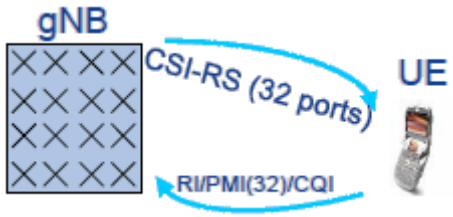

Figure 2.18: Single CSI-RS Signaling [22]

Multiple CSI-RS It combines beamforming with CSI-RS and CSI-RS Resource Indicator (CRI) feedback. The gNB transmits one or more CSI-RS each in different direction, the MT then computes the CRI /PMI/CQI and transmits it to the gNB. It supports arrays having arbitrary number of TRXUs and can be used as beam refinement in P-2 after SSB sweeping.

Figure 2.19: Multiple CSI-RS Signaling [22]

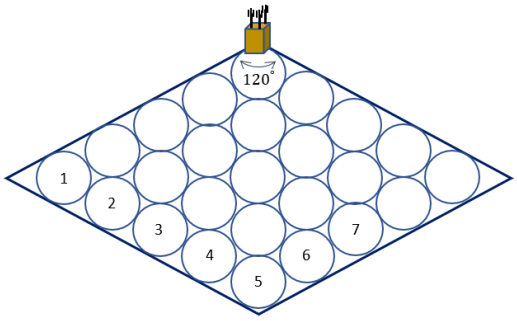

Figure 2.21: codebook-based beamforming massive MIMO cell Architecture

SRS-Based Designed for TDD systems. The MT sends the SRS signal and the gNB computes the precoding weights. Since in TDD the DL and UL channels can be assumed identical, the UL channel characteristics calculated by the gNB can be assumed for DL also.

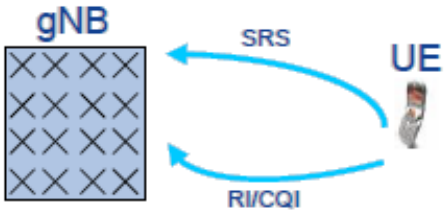

Figure 2.20: SRS Based Signaling [22]

Cell architecture

In NR, the sector-based cell architecture is no longer applicable in order to overcome the disadvantages of the usage of the mmWave band by using beamformed transmission. The cell architecture will be dependent on the characteristics of the massive MIMO antenna used at the gNB. It has been reported in that Nokia, for example, had a system with 128 antennas that can produce 32 beams, thus, a 32 beams massive MIMO system, with the aim to schedule up to 4 beams simultaneously. Below is an example of a 20 beams cell sector, spanning over an angle of 120°. Note that the predefined beams are those used for signaling and control, and the data beams can be dynamically formed depending on the cell usage.

EPRE and power allocation

The energy per resource element (EPRE) was a part of LTE power control before 5G and signifies the energy allocated to each resource element in a physical channel. Some of the relations of allocated power per resource element are highlighted in the 3GPP specifications [20] 15]. These relations can help in estimating the increase of the antenna

Number of DM-RS CDM groups without data	DM-RS configuration type 1	DM-RS configuration type 2
1	0 dB	0 dB
2	-3 dB	-3 dB
3	-	-4.77 dB

Table 2.4: The ratio of PDSCH EPRE to DM-RS EPRE

gain between the data and the signaling beams. The downlink EPRE directly specified are below. physical downlink shared channel (PDSCH) EPRE to DM-RS EPRE varies with the number of DM-RS CDM groups without data and given by Table 2.4 [15]. SSS, PBCH DM-RS and PBCH have the same EPRE. The ratio of PSS EPRE to SSS EPRE in a SS/PBCH block is either 0 dB or 3 dB. The ratio of PDCCH DMRS EPRE to SSS EPRE is within -8 dB and 8 dB [20].

2.5 Conclusion

In this chapter, we introduced the 5G NR physical layer and radio access network (RAN) technologies. We also introduced massive MIMO antennas, discussing their different possible architectures, deployments, and beamforming techniques. The high paryh-loss in mmWave bands will require high transmitted power to ensure SIR threshold, which can be achieved using massive MIMO antennas. Massive MIMO antennas can have many array structures that may allow multi or single user transmission, and digital, analog or hybrid beamforming. Different strategies of downlink power control can also be used like zero-forcing or max-min fairness. 5G networks will also be deployed in heterogeneous networks with small-cells and macro-cells, and as NSA and SA technology. Moreover, different sub-carrier spacings can be assigned at the 5G frames which affect slot timings and physical channels' bandwidth. Uplink and downlink assignment can also be done at symbol level and can be assigned flexibly by the operator.

It is apparent from this chapter, that measurement procedures need to be revisited for 5G systems to get an accurate EMF values. The main challenges for 5G measurements stem from the spatio-temporal variation of the emission alongside the effects of beamforming and beam refinement. In the next chapter, we introduce the metrics specified for EMF exposure estimation, and we discuss the different types of measurement techniques that can be used for 5G systems. We also present the results of an in-situ measurement, using the Keysight PXA signal analyzer, of a 5G massive MIMO antenna in different scenarios and using different methods.

Chapter 3

In-Situ Exposure Assessment of 5G Networks

Contents

3.1 Introduction

Since its emergence and spread, the human exposure to EMFs from wireless communications and radio technologies have been a source of worry for both the general public and for health professionals. And with each generation, and with the increasing deployment of transmitting devices to meet the ever-increasing demand, the demand for more precise studies, and clearly defined constraints grows larger. To give assurance to the public, and to maintain safe levels of EMF exposure, national and international standardization bodies such as ICNIRP, FCC, the European Council, and IEEE-SCCs emerged to standardize and to give guidelines on evaluation tests and limits ensuring no effect on the users.

In this chapter, we present the metrics of EMF exposure measurements used for compliance assessment. We then present signal power measurements of 5G massive MIMO antennas while discussing the different measurement methods presenting their advantages and disadvantages and highlighting areas where more improvements should be made for proper characterization of the exposure.

3.2 Electromagnetic field exposure metrics

The increase of deployment of cellular base stations and advanced wireless antennas, like large-array antennas and small cells, have increased the public dislike of these structures and made more countries concerned for the public health. This has led legislators to put forward restrictive limits on RF emissions. ICNIRP provides widely-accepted limits [24] through out the scientific community and constitutes the current scientific consensus [25]. Limits can be defined differently depending on the scenario in question with the main two metrics being the specific absorption rate (SAR) and the power density.

3.2.1 Specific absorption rate

The highest exposure for the general public is handheld devices and near-field emissions. The limits for such scenarios, the limits that are mainly considered by the SAR value, where the body configuration, the emitting device's positioning, and the device's design have strong impact on the absorbed power. The whole-body SAR can be defined as follows

$$SAR_{WB} = \frac{P_{abs}}{m}, \tag{3.1}$$

where P_{abs} is the absorbed power by the body in W and m is its mass in Kg. SAR can also be evaluated locally for specific body parts. Another way to express the SAR is by

linking it directly tot the incident electric field

$$SAR = \frac{\sigma E^2}{2\rho}, \tag{3.2}$$

where E is the incident electric field in (V/m), σ is the conductivity in (S/m), and ρ is the density of the tissue in (Kg/m^3). The SAR is the quantity used for exposure evaluation mainly in frequencies below 6 GHz in the IEEE standard and 10 GHz in the ICNIRP standard.

3.2.2 Power density

While the notation of SAR is mostly used in the near-field region of EMFs, the power density is the commonly used unit for exposure characterization in the far-field, especially in frequencies higher than 6 GHz that will be used in 5G. Power density is described by the power per unit area and is usually expressed in terms of watts per meters squared (w/m^2). In the IEEE-C95.1 standard the power density limit is considered for frequencies above 3 GHz, and for frequencies above 10 GHz in ICNIRP (1998). The power density is averaged over an area of 20 cm^2 and the limit for averaging it over an area of 1 cm^2 should not exceed 20 times the limit. The limit for the average power density has been specified in ICNIRP (1998) are 50 and 10 (W/m^2) for occupational exposure and general public, respectively.

3.3 5G NR measurement methods and scenarios

5G systems are being designed to be extremely flexible in terms of both the antennas used, the resource allocation, and the cellular system architecture. NR will have major differences in handling data transmission and reception. Moreover, the exact architecture and models are still being developed, and each constructor/operator can develop vastly different technologies of antennas and RAN architecture. This diversity in implementation possibilities makes the characterization of the emission more challenging than for older technologies, since it can be affected by many variables. Moreover, the EMF exposure in a 5G network will be highly dependent, much more so than older generations, on parameters that can only be represented statistically, e.g. MT distribution and density in the cell. This shifts the focus of EMF exposure estimation from the theoretical maximum to statistical percentiles of the possible exposure values [26].

Although the 5G waveform that has been decided by 3GPP specifications is OFDM based, and shares some characteristics with its predecessor in LTE, the 5G Massive MIMO antennas will require the development of a new approach to estimate the downlink exposure. Unlike in LTE, the emission of a 5G antenna, seen from a certain location in

space, is not continuous. The beamforming from a hybrid massive MIMO antenna allows the formation of up to n beams simultaneously at a certain point in time. In order to estimate the actual exposure induced by a 5G antenna, this variation must be considered. In order to properly estimate the exposure of a 5G antenna, the following issues must be tackled: The estimation of the exposure under maximum traffic conditions, estimation of the spatio-temporal variation of the antenna's serving beam, and the increase in gain due to beam refinement in the connected state. The following sections will review some measurement methods and check their compatibility with 5G systems.

3.3.1 Full spectrum measurement

Frequency domain and channel power

Frequency domain measurements are possible with current widely available spectrum analyzers which allows the measurement of the received power at a selected frequency range. This however can be operated in two scenarios, swept and real-time.

Swept spectrum analyzer This mode occurs when the selected measurement frequency is larger than the spectrum analyzer's resolution bandwidth (RBW). This will will divide the measurement bandwidth into sections that will get measured successively, and will take a duration denoted by "sweep time" to complete a sweep over the whole band.

Measuring the 5G transmission channel in the frequency domain will introduce inaccuracies in the measurement, for 5G more so than LTE, due to the high variability of the beamformed emissions and its dependence on the traffic variations, and the impossibility of the separation of the downlink from the uplink symbols in TDD. Since the sweep time is usually large compared to beam assignment frequency which can be done at subframe level.

Real-time spectrum analyzer This mode occurs when the measurement bandwidth is equal or less than the RBW of the spectrum analyzer. This condition, while not easily available in current hand-held measurement equipment, allows the real-time measurement of the whole bandwidth without loss of information.

Wile real-time spectrum analyzer will overcome data loss due to sweeping, it will still raise questions on the measurement performed in a 5G massive MIMO network. The power received at a certain location in the cell depends on the traffic and MT density in that specific location. An area with large number of active MTs will have a higher average power value in the transmission channel than an area with low number of served MTs. Moreover, the power hot-spots for a code-book based massive MIMO can easily be missed when performing the measurement.

3.3.2 SSB measurements

Since full spectrum measurements of the 5G does not give a sufficient representation of the received power, an alternative method has been suggested to get a conservative estimation of the received power. It consists of measuring the the always on downlink channels, then extrapolating it over the whole band. The Synchronization Signal Block (SSB) is the only downlink channel that is independent of the traffic and is periodically emitted with period T= {5, 10, 20, 40, 80, 160 ms} and is emitted in bursts depending on the numerology used.

SSB signals are composed of three physical channels (PBCH, PSS, SSS) spanning over 20 RBs in frequency and four OFDM symbols in time. The number of SSBs is also specified by the used numerology and each SSB is mapped to a signaling beam in case of beamforming. SSBs are located by default around the center frequency of the emission, and it can be measured over a specified bandwidth less or equal to its bandwidth.

Time domain

Measurements in the time domain (zero-span), as in Figure 3.1, gives the instantaneous power received over the measurement bandwidth. Measuring the SS block requires a RBW of around 7.2 MHz for 30 KHz subcarrier spacing, but a lower RBW (e.g. 1 MHz) can be used since the power of the SS block is constant (assuming no boosting of the PSS channel relative to SSS) and not dependent on the traffic.

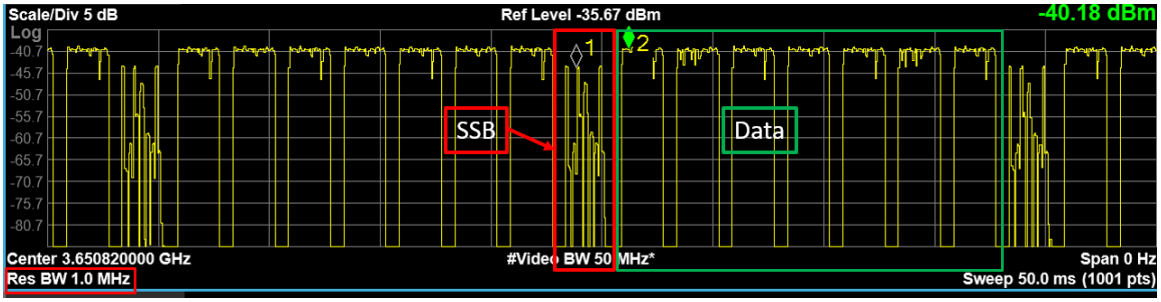

Figure 3.1: Zero-Span (Time Domain) measurement when data is being transmitted over a single beams showing the SSB power and data in time when measuring over 1 MHz bandwidth at the center frequency

Demodulation domain

Demodulation domain measurement, shown in Figure 3.2 produce the most accurate results when measuring the SSB power. In addition to that, demodulating the signal allows the access to some extra information like beam and cell identification. Demodulation domain measurements also help measure the PDSCH - DMRS signal useful in estimating the beam refinement gain explained below in section 3.3.3.

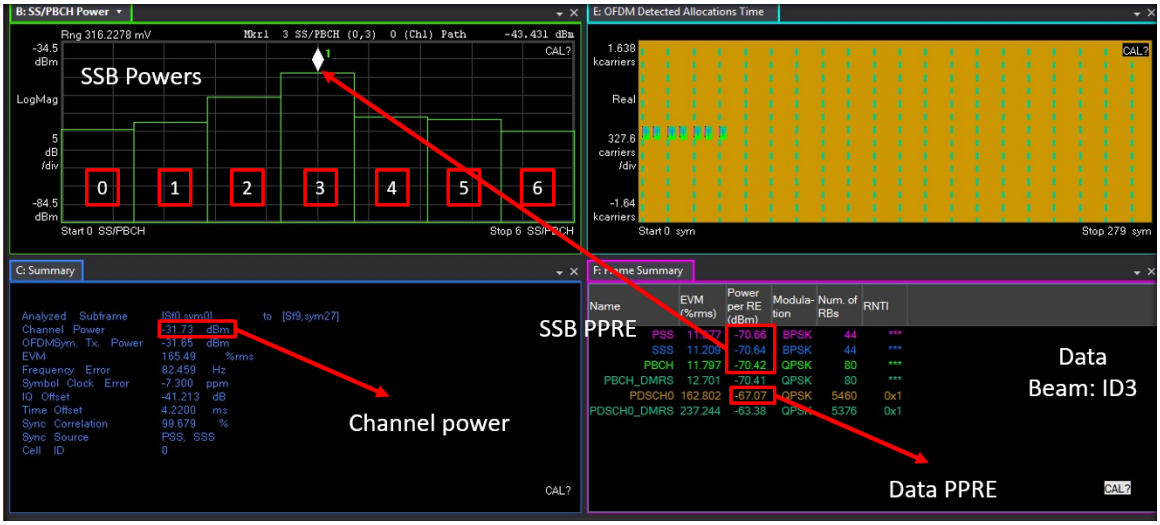

Figure 3.2: Demodulation domain measurement when data is being transmitted over the SSB beam 3, showing measured powers of the SSBs, the channel power and the power per resource element (PPRE) of signaling and data channels

Extrapolation

Be it in the time domain or demodulation domain, the measured instantaneous power of the SSB channels can be extrapolated to the whole transmission bandwidth to estimate the maximum possible received power from a specific beam at the measurement location. The extrapolation can be done by multiplying the power per RB of the measured signal by the extrapolation factor $K = N_{RB} \times N_{sc}^{RB}$, where $K = N_{RB}$ is the number of resource block (RB)s and N_{sc}^{RB} is the number of subcarriers per RB, to obtain the power over the whole band.

3.3.3 Beam refinement

One of the characteristics of 5G radio access is beam refinement, illustrated in Figure 3.3, which is the second step in establishing the connection between the gNB and the MT for data transmission. This dictates that the antenna will adapt its beamforming to be more suitable for the specific served MT. Therefore, the gain of the antenna when transmitting in the signaling channel will not be the same as when transmitting in the data channel.

Beam refinement, if used, means that we can't simply measure the SSB channel and extrapolate it to the transmission bandwidth, since the gain will be higher when transmitting data. And the refinement gain cannot be necessarily obtainable from the manufacturer/operator when doing in-situ measurements thus making it necessary to estimate the increase in gain to avoid the underestimation of the emission.

This refinement gain can be estimated by measuring the difference in the received instantaneous power in a small frequency band (e.g. 1 MHz) between the SSB and the

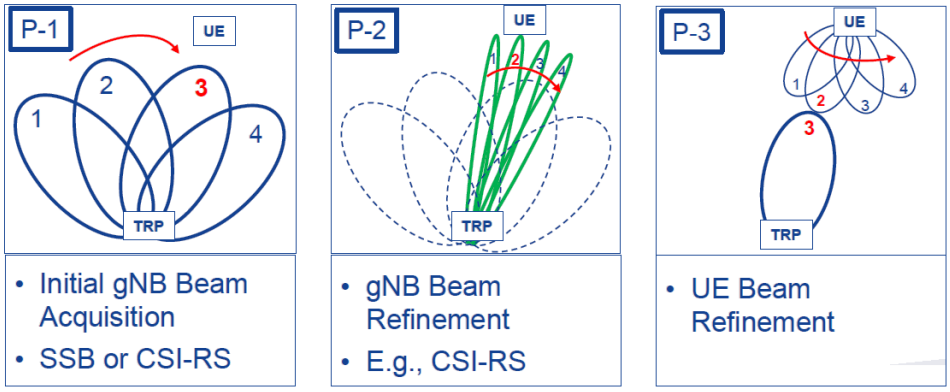

Figure 3.3: Representation of the beam refinement procedure as a second step of the signaling after the SSB selection [8]

PDSCH. Since power control is not necessary in 5G (static or semi-static, if present), the allocated Energy Per Resource Element (EPRE) is either constant or has a static offset between SSB subcarriers and PDSCH subcarriers [27]. The measured received instantaneous power per resource element should differ between the SSB channel and the data channel only due to the gain of beam refinement. To determine the increase in gain due to refinement, it is sufficient to determine the ratio of the received instantaneous power in a resource element between the PDSCH and SSB channels as follows

$$G_{BR} = P_{RE}^{PDSCH} - P_{RE}^{SSS}\text{dB} \tag{3.3}$$

We can assume that EPRE_{SSS}= EPRE_{PDSCH} [28], which is not necessarily true for every scenario, but seems to be the default if no downlink power control is deployed.

Beam refinement gain can also be determined by calculating the power ratio between the PDSCH-DMRS and SSB in demodulation domain, and accounting for the suitable power control ratios if present. Refinement gain can be hard to detect if the PDSCH EPRE is lower than the SSS EPRE. The ratio of PDSCH EPRE to DM-RS EPRE (same as SSS EPRE) is stated in [27].

Beam refinement varies with the location of measurement since the refined beams are generally precoded and can sometimes be used for vertical steering of the antenna beam, as will be shown in section 3.4. Measuring in a real network however, makes it hard to distinguish data channels for each beam in the time domain thus deducing the refinement becomes more difficult.

3.4 5G massive MIMO measurements

In this section we present multiple measurements done on a 5G massive MIMO antenna. We present exposure measurements in frequency (channel power) domain and by

extrapolating the SSB power done in both time domain (zero-span) and demodulation domain. We analyze these measurement methods and compare them, we also present the advantages and disadvantages of each of them.

3.4.1 Measurement setup and scenario

In this section we present measurements done on a 5G massive MIMO antenna, emitting over a 100 MHz bandwidth at the 3.65 GHz center frequency, using Keysight's PXA signal analyzer co-located with a receiving MT. It involved a 64-elements antenna transceiver capable of 1-D sweeping in the horizontal direction using SSBs, and capable of 2-D beamforming in both horizontal and vertical directions for data transmission using CSI-RS. The beamforming vectors were predefined in a 7×4-beam code-book as shown in figure 3.4 for data transmission with IDs ranging from 0 to 30 divided into 7 rows and 4 columns. The PXA was installed at a fixed distance directly in face of the MIMO. We measure the power received at the PXA when data is transmitted over beams 3, 11, 19, and 27. The measurements were performed to test different characteristics of the 5G antenna for different transmission scenarios. We present measurements in the time domain (zero-span), frequency domain (spectral analysis), and demodulation domain. We analyze the observations from the measurements and discuss their advantages and shortcomings.

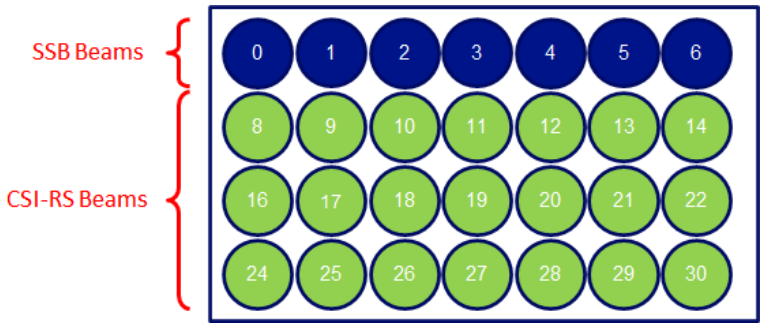

Figure 3.4: Representation of the measured massive MIMO's beamforming code-book

3.4.2 Demodulation domain measurements

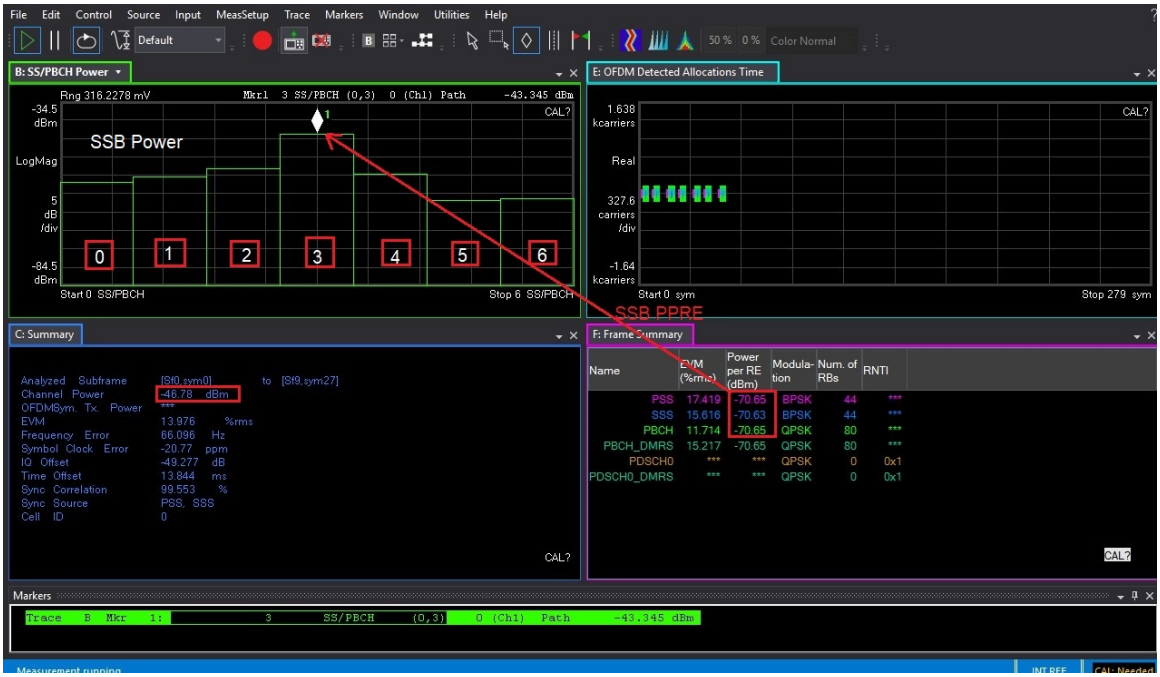

Figure 3.5: Demodulation domain measurement for 0% traffic load being transmitted on the data channel and only the SSB channel is on

In Figure 3.5, we measure the downlink transmission of the 5G antenna in the demodulation domain when no traffic load is present. In this type of measurement, we can get the power per resource element (PPRE) of each signaling block corresponding to each beam formed at the BS. The main serving beam is the one that has the highest power, which is at -70.65 dBm in this measurement and corresponds to the fourth SSB/beam, the number of RB can then be used to extrapolate the total power.

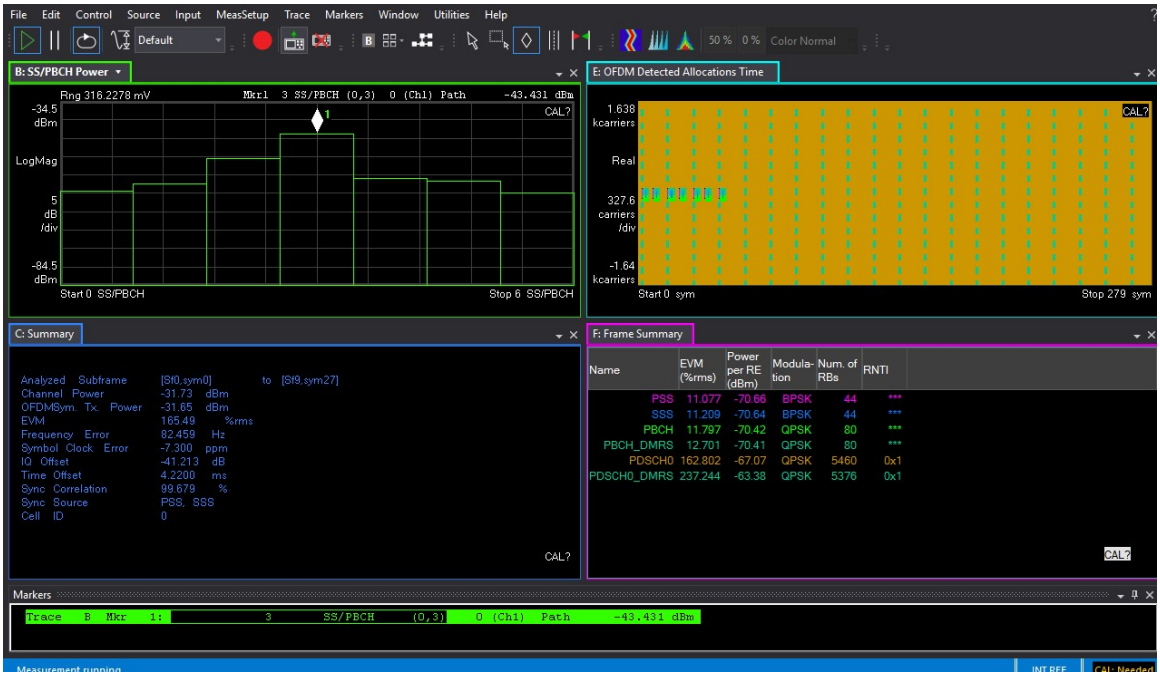

Figure 3.6: Demodulation domain measurement when we send 100% traffic load of data at beam 3

In Figure 3.6 3.7 and 3.8, the downlink transmission is measured also in the demodulation domain for 100% traffic load and where the data is being sent on beams 3, 11, and 19 consecutively, which represents the same horizontal direction, i.e. SSB beam, but several elevation angles. We notice that the ranking of the SSB beams remains unchanged even with slight changes in power values, which is to be expected. In this case, it is also possible to measure the PPRE of the downlink data channel, PDSCH, and we notice the difference in power between the SSB and PDSCH, and we notice that the ideal serving beam for the MT is 11. This difference is due to the beam refinement gain done after the signaling phase.

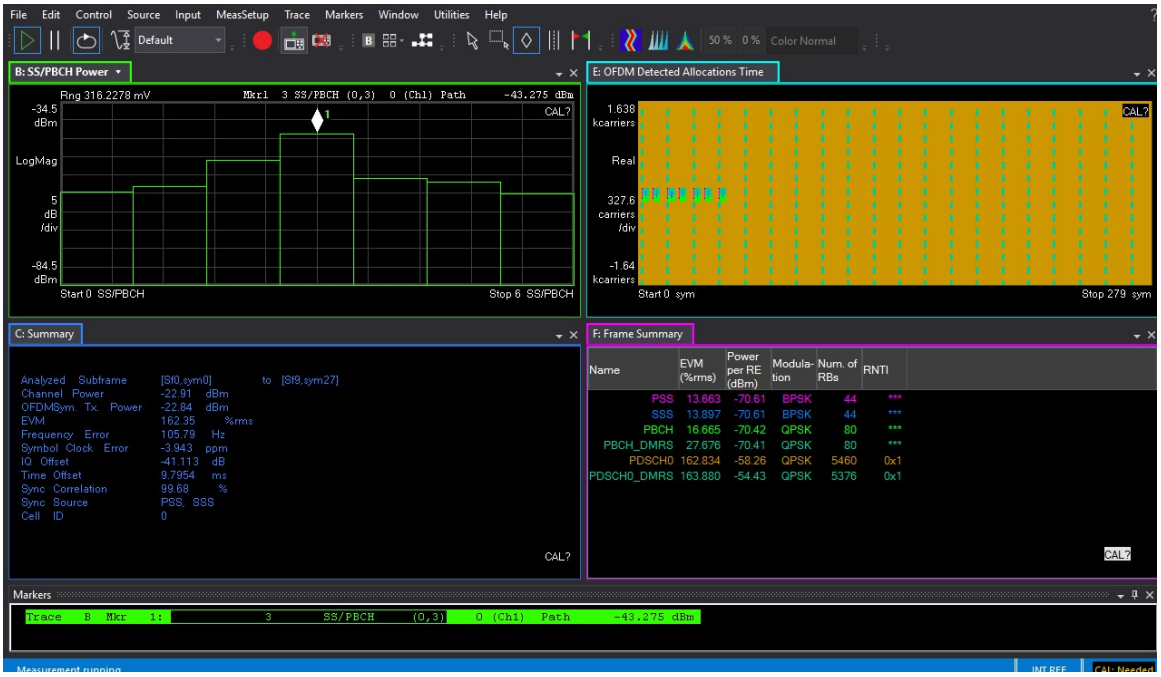

Figure 3.7: Demodulation domain measurement for 100% traffic load transmitted over beam 11

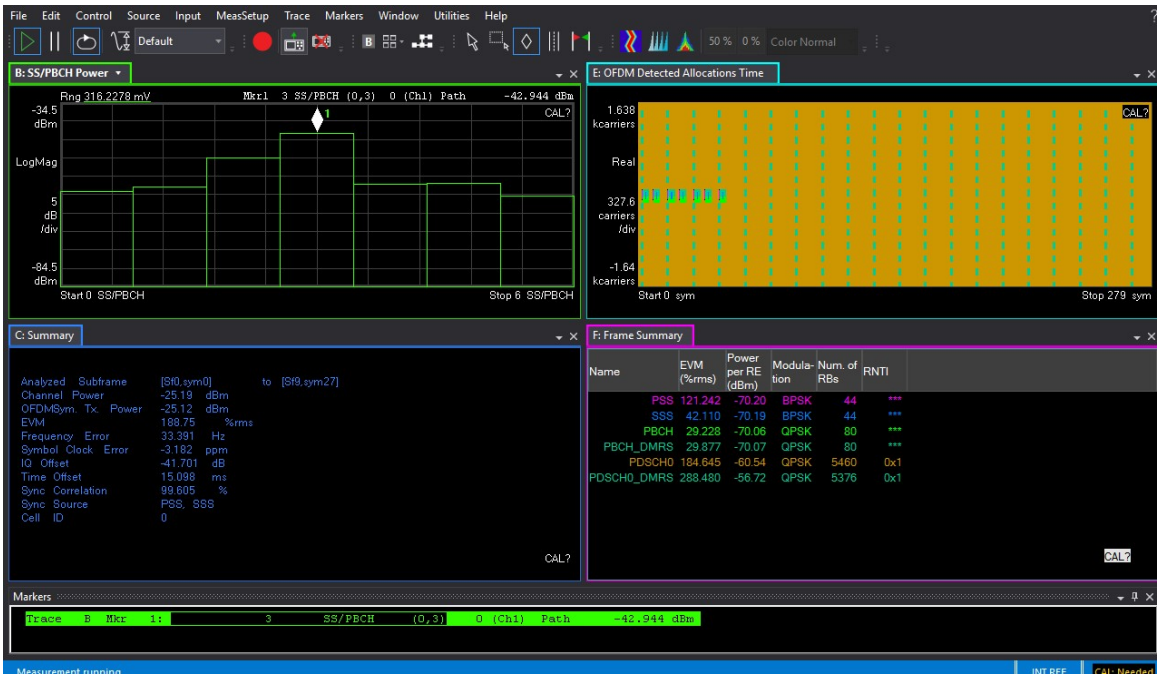

Figure 3.8: Demodulation domain measurement for 100% traffic load transmitted over beam 19

In Figure 3.9, we measure in the demodulation domain while transmitting data in four randomly selected beams that are allocated every 20 ms. We notice that, while the PPRE remains unchanged for the signaling channels, the PPRE drops significantly for the PDSCH. This measurement scenario is more representative of the actual deployment of the MIMO antenna in a 5G system, since many MTs will have to be served simultaneously

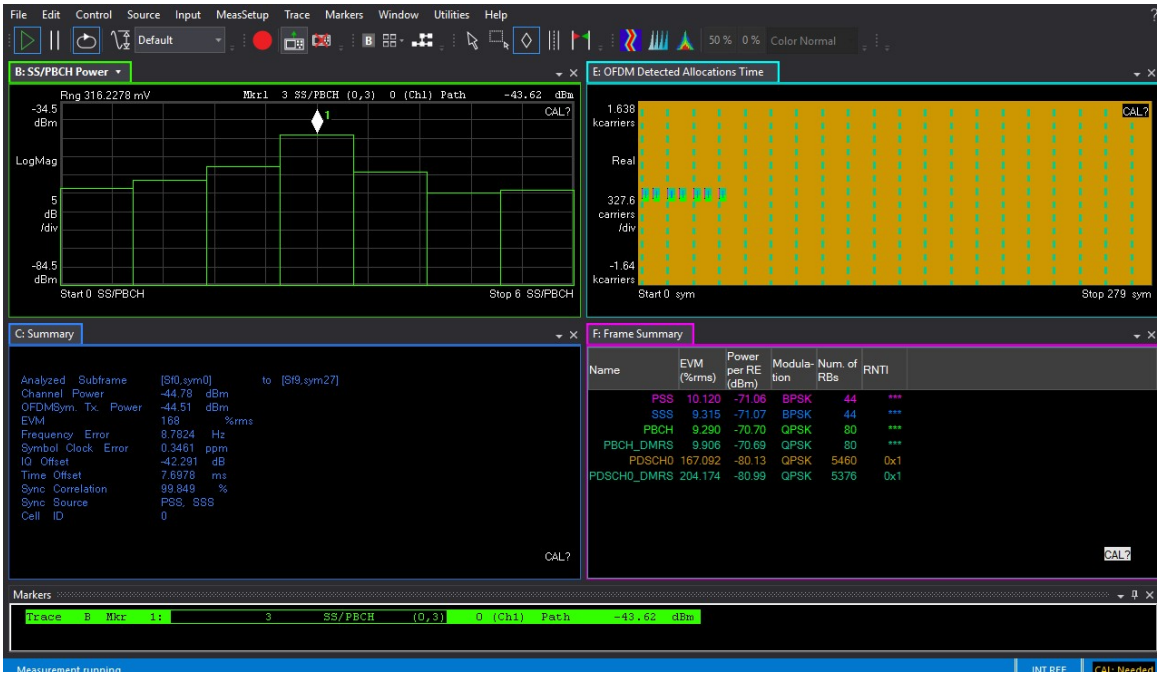

Figure 3.9: Demodulation domain measurement for 100% traffic sent over 4 different beams

using different beams. In this scenario, the power allocated to each MT/beam, likewise the frequency resources, depends on the MT's requirement and the BS capability.

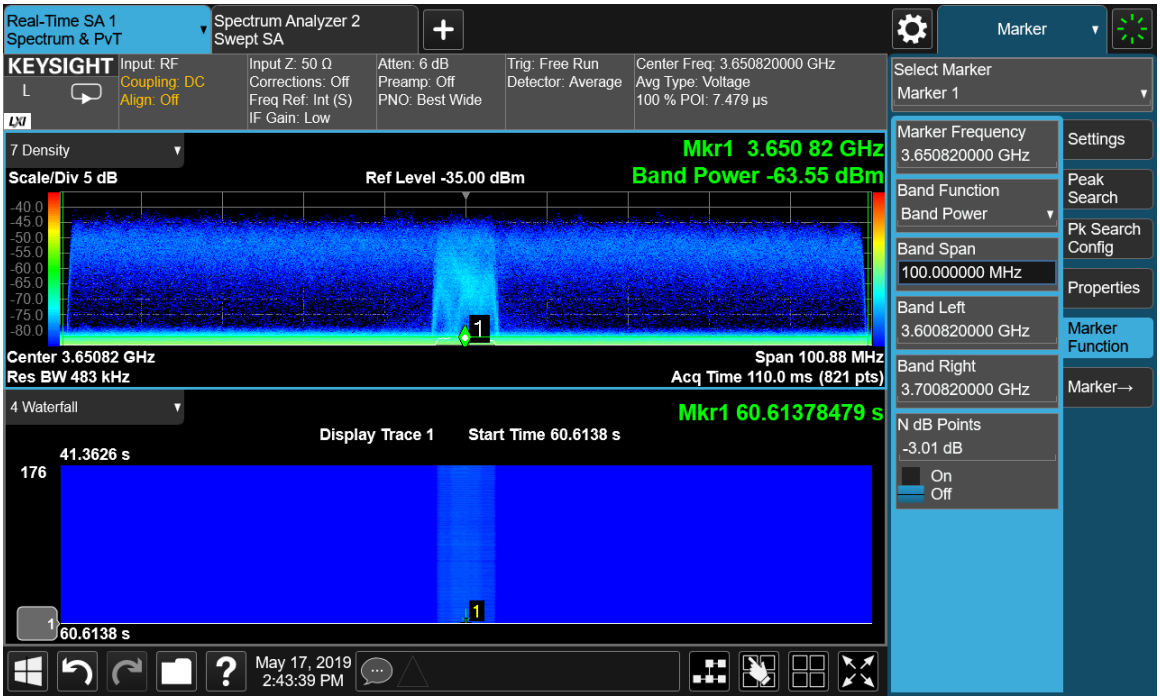

Figure 3.10: Frequency domain measurement over the whole 100 MHz band for 0% traffic load

3.4.3 Frequency domain measurements

In Figure 3.10, we measure the channel power when no traffic is present. We notice the power values at the center of the spectrum, which corresponds to the SSB signal power. The channel power measured is, as expected, low at −63.5 dBm measuring the whole 100 MHz band, and the peak power value is measured at −35 dBm. A waterfall display is also presented on the bottom half which shows the periodicity of the SSB channel.

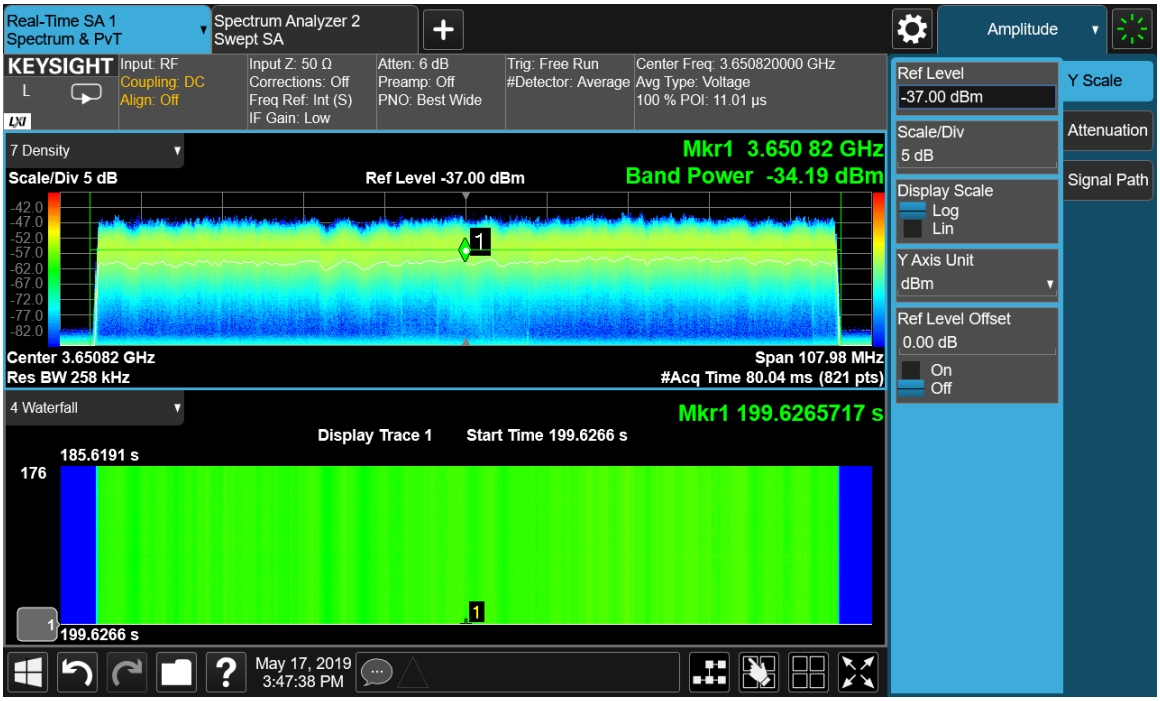

Figure 3.11: Frequency domain measurement over the whole 100 MHz band for 100% traffic load transmitted over beam 3

In Figure 3.11, 3.12, 3.13, and 3.14, we measure the channel power for 100% traffic load being sent on beams 3, 11, 19, and 27, respectively. Just like in demodulation domain measurements, we deduce that the optimal beam to the served MT, co-located with the PXA, is beam 11 since it has the highest channel power. We also notice the channel becoming more frequency selective, and more prone to fading, the more we move away from the optimal beam and the transmission is moving away from being in LoS.

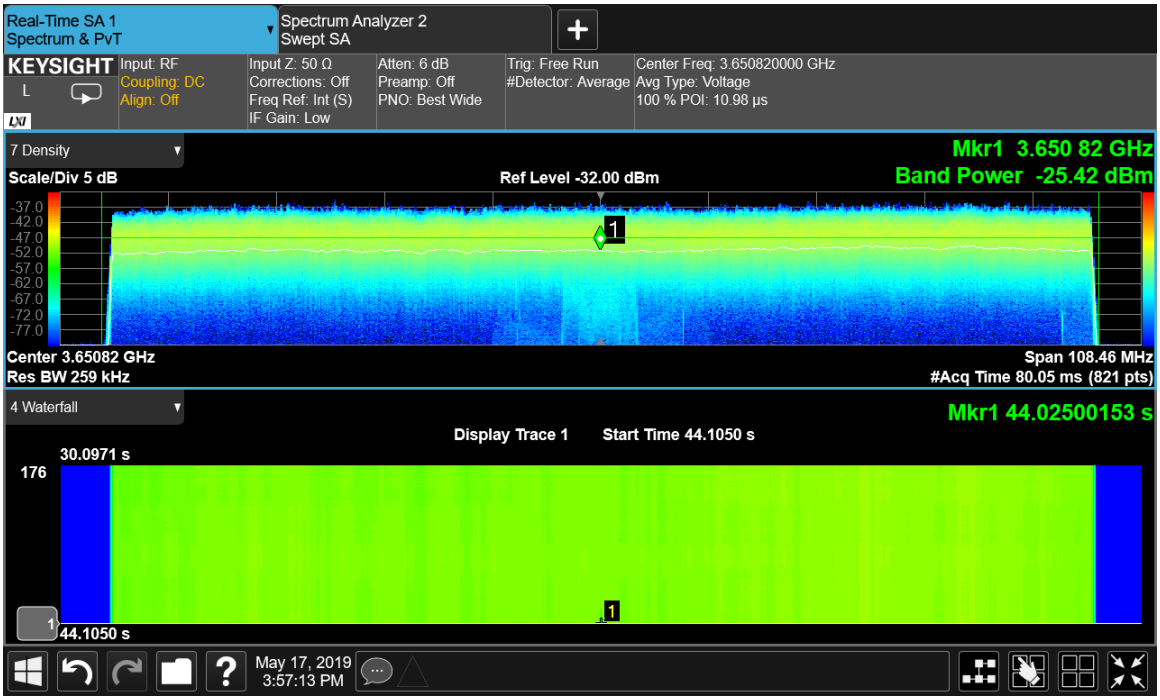

Figure 3.12: Frequency domain measurement over the whole 100 MHz band for 100% traffic load transmitted over beam 11

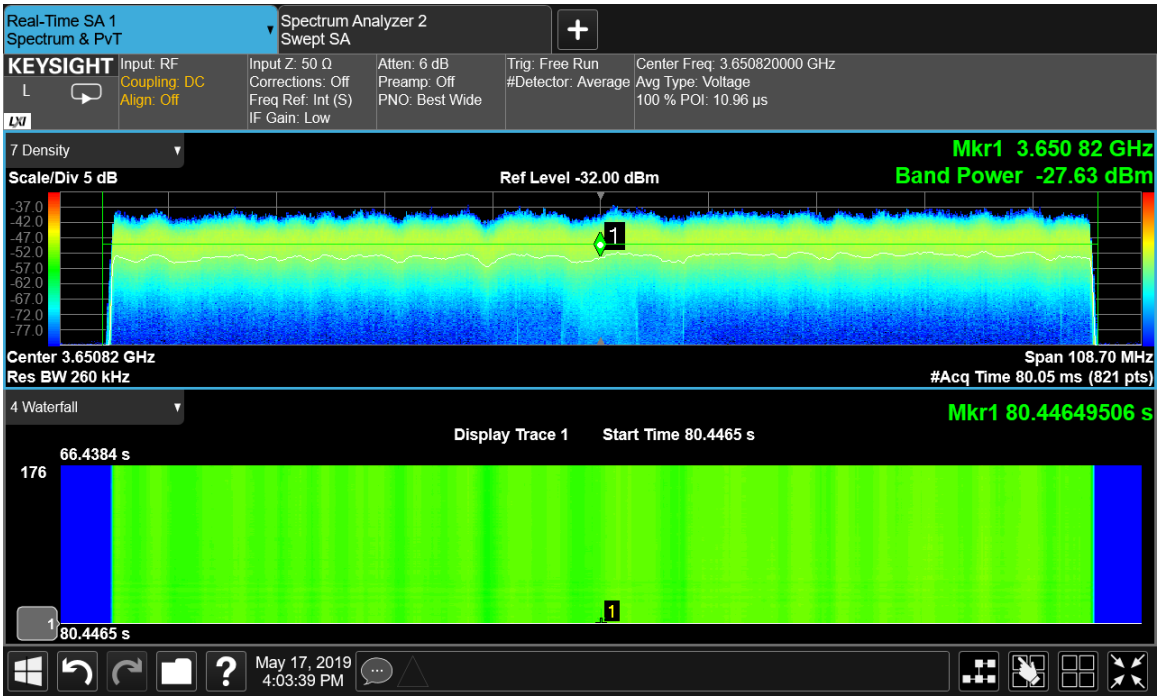

Figure 3.13: Frequency domain measurement over the whole 100 MHz band for 100% traffic load transmitted over beam 19

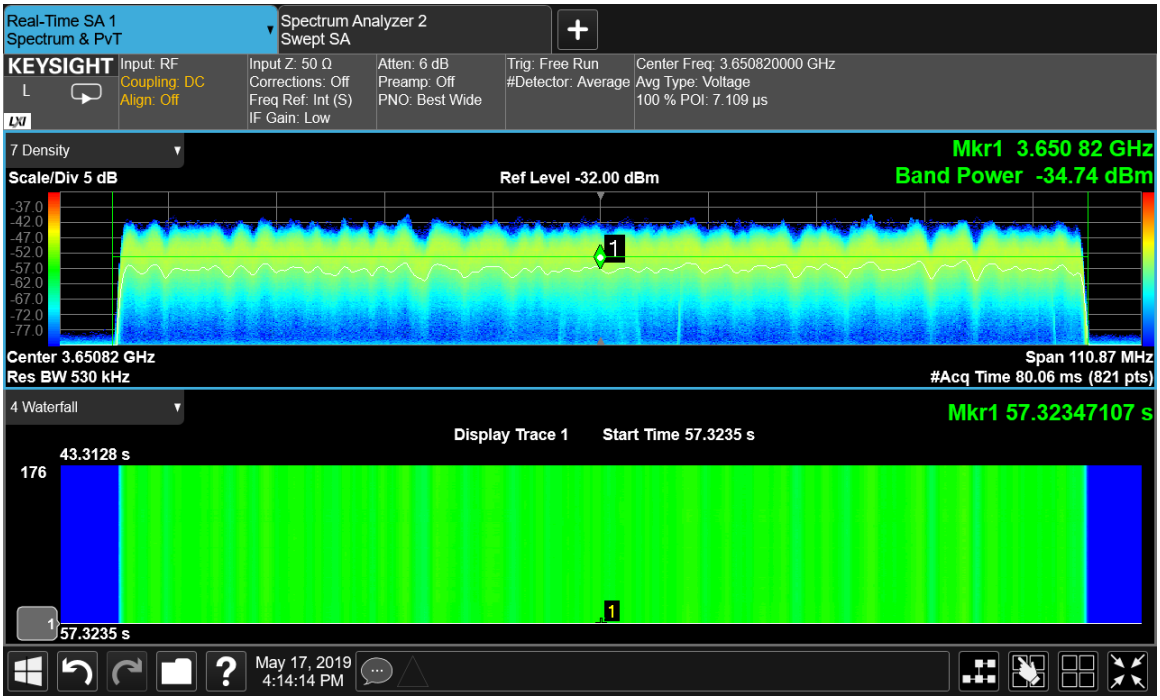

Figure 3.14: Frequency domain measurement over the whole 100 MHz band for 100% traffic load transmitted over beam 27

We also measure the spectrum when we emit simultaneously on four different beams as shown in Figure 3.15. In this mode, we are measuring the power received from the optimal serving beam to the MT and PXA, in addition to the multi-beam interference which can be equated to multi-user interference in an actual deployment of the antenna.

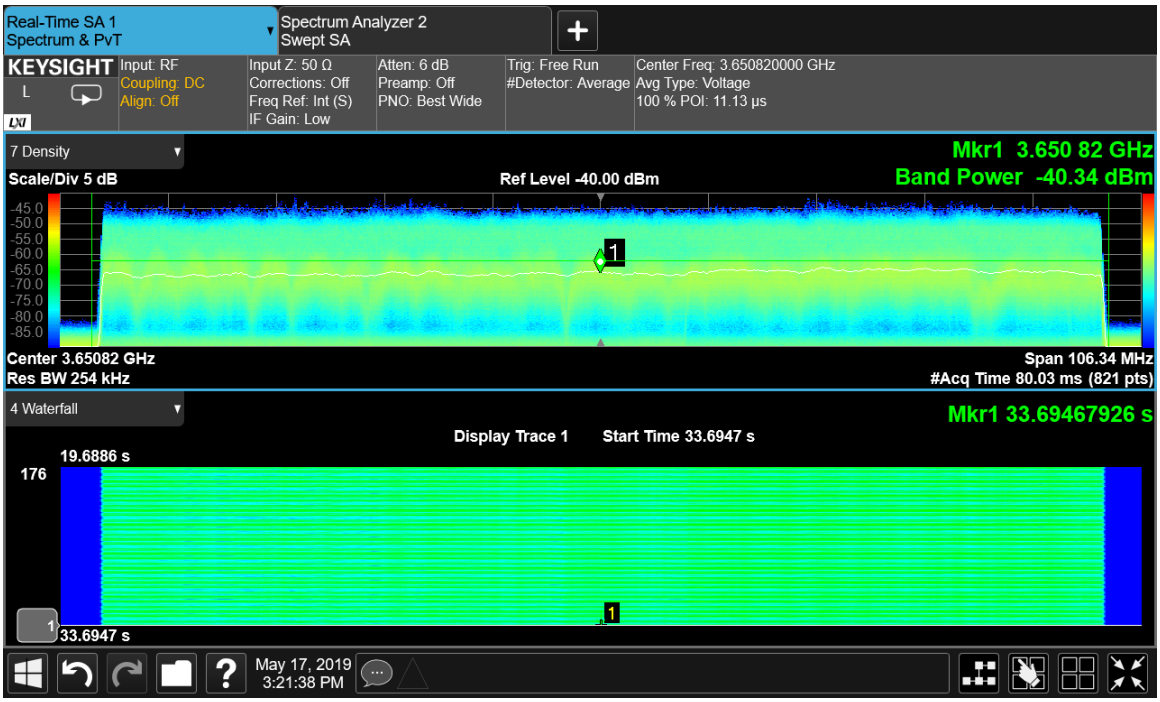

Figure 3.15: Frequency domain measurement over the whole 100 MHz band for 100% traffic load sent over 4 different beams

3.4.4 Time domain measurements

We measure the received signal power in zero-span configuration over a RBW of 1 MHz, centered around the center frequency of the transmission. This bandwidth will allow the measurement of the SSB in time-domain. In this measurement, since we are emitting over the whole spectrum, and the RBW is fully covered by the SSB channel, the measured power values in zero-span are distributed over the same bandwidth and thus the power values at the SSB can be compared to the values of the data (PDSCH). We also recall that the SSBs are associated to beams 0 to 7, and the optimal SSB corresponds to beam 3.‘

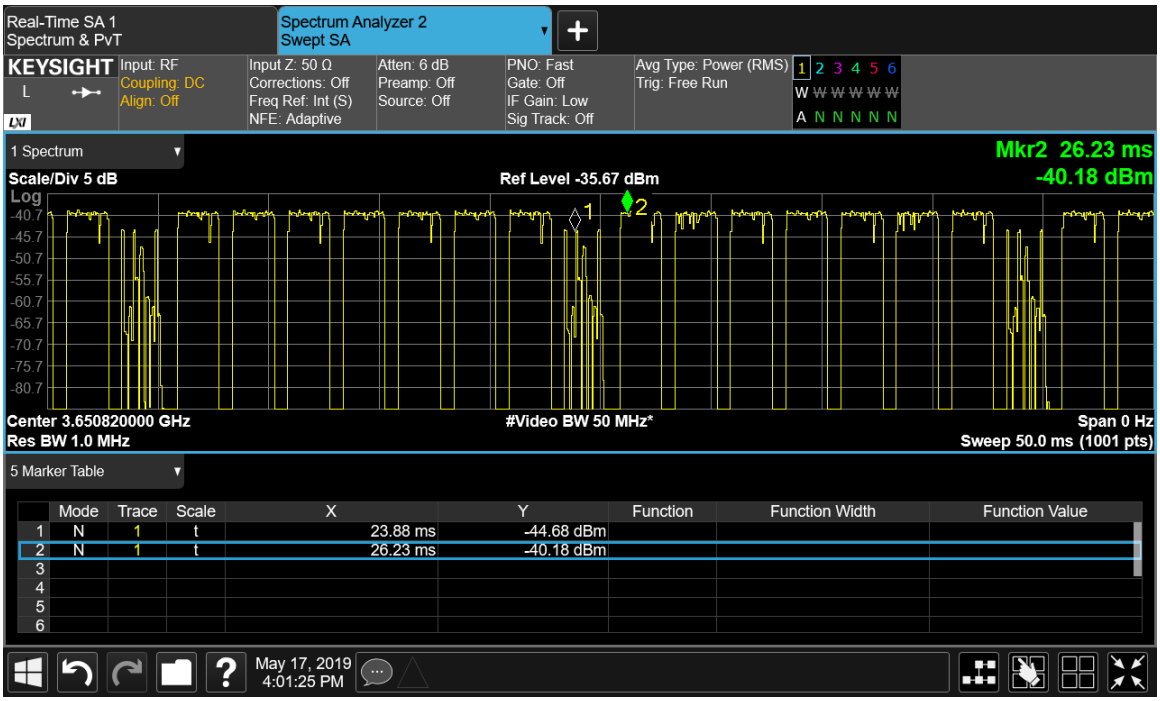

Figure 3.16: Time domain measurement for 100% traffic load transmitted over beam 11

In Figure 3.16, we present the time domain measurement of the received power for 100% traffic load when transmitting at beam 11. In the figure, we measure the SSBs alongside the PDSCH over a 1 MHz bandwidth. We notice the difference in measured power between the optimal SSB beam, 3, and the power received from the optimal beam, 11, which is in this case 4.5 dB.

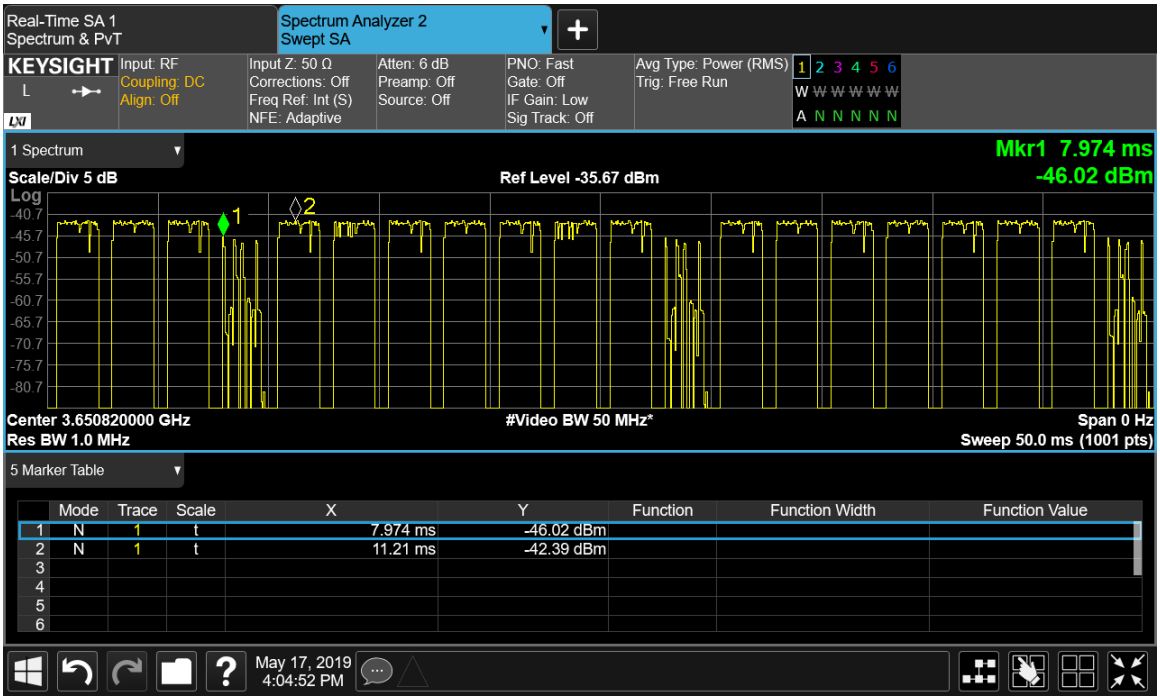

Figure 3.17: Time domain measurement for 100% traffic load transmitted over beam 19

In figures 3.17 and 3.18, we perform the same measurement when transmitting in beams 19 and 27. The SSB power values are the same, but the PDSCH power is lower, in accordance with the other measurement types.

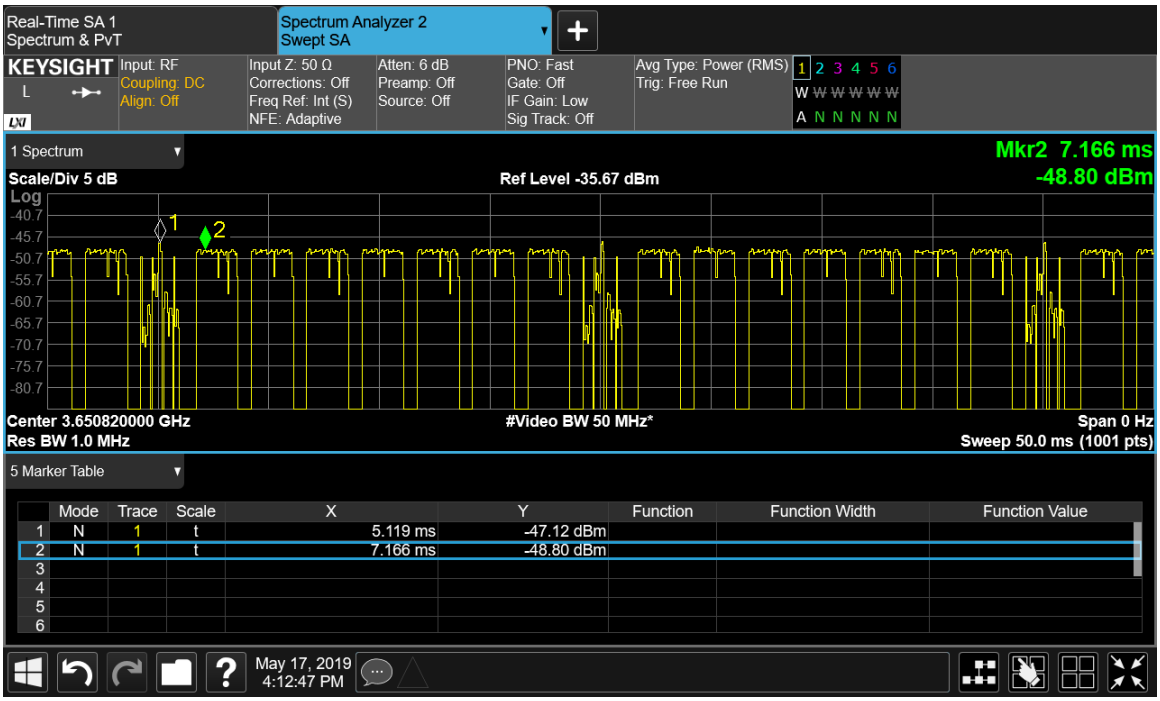

Figure 3.18: Time domain measurement for 100% traffic load transmitted over beam 27

We also measure in zero-span, like with previous types of measurements, when transmitting in four different beams, presented in Figure 3.19. We notice the the different

power values of the different beams received at the PXA. Measuring the PDSCH seems straightforward from this configuration, however, the PDSCH is not necessarily sent over the whole bandwidth, nor is it necessarily present around any specific frequency. In this figure, we also notice the presence of periodic power spikes which can be attributed to the CSI-RS channel. This channel spans only over 1, 2, or 4 OFDM symbols, meaning that the instantaneous power measured in zero-span would not give visually-comparable values to the SSB and PDSCH, their power values however can be extrapolated if their configuration was known.

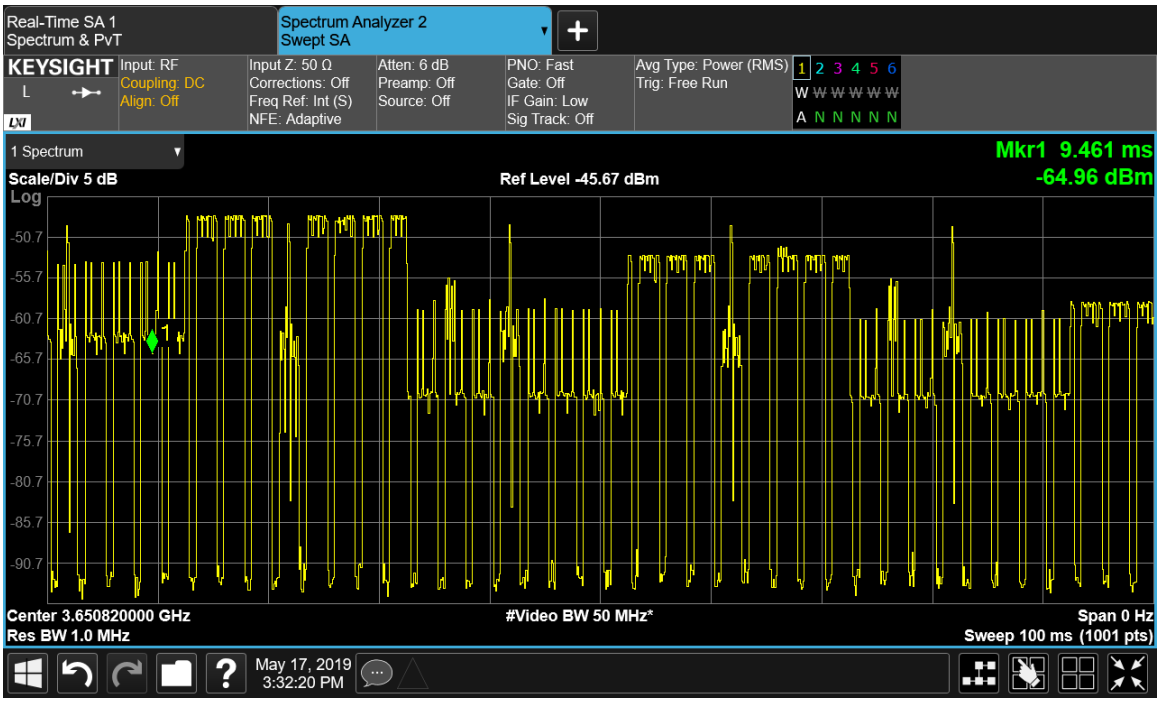

Figure 3.19: Time domain measurement for 100% traffic load sent over 4 different beams

3.5 Conclusion

From these measurements, we can predict the challenges when measuring a 5G massive MIMO network's exposure when actually deployed. Utilizing a swept spectrum analyzer will introduce a loss in information when measuring the power in frequency domain since the beam does not necessarily emit over the whole bandwidth. This loss can be significant since the difference in power between beams can be very large in a network. Moreover, measuring the channel power without loss of information due to sweeping requires a large RBW, which may not be available for handheld analyzers or otherwise, since, for 5G networks, transmission bandwidth can go up to 400 MHz.

The alternative way of measuring the SSBs and extrapolating the power to get a conservative estimation, while seemingly promising, can largely underestimate the received power due to beam refinement after the initial SSB beam selection. The refinement gain

can be very significant, like in our case here, where the refinement is done at another dimension completely, and cannot be reliably measured in a realistic network. Also extrapolating the SSB power would give the highest possible power value at the location of measurement itself, and can vary significantly between the locations since we would not be sure of the specific location of the power hot-spot, especially in NLoS scenarios where a beam does not necessarily have a single angle of departure. In addition to that, multi-user antennas serving more than one MT in the same time-frequency block will reduce the gain of the data channel without necessarily affecting the SSB this will further add more uncertainty to the measurement since the gain will depend on the number of MTs served.

For all the reasons above, and since there haven't been a real deployment of 5G massive MIMO network, characterizing and studying the exposure of massive MIMO networks using in-situ measurements will be lacking. We believe it is essential to study the exposure analytically to investigate the different characteristics of the network and its antennas. It is also necessary to characterise the exposure under a more realistic network scenario, in this dissertation, we opted to do that using stochastic geometry, which is what we present in the following chapters.

Chapter 4

Introduction to Stochastic Geometry in Wireless Networks

Contents

Both the performance and the EMF exposure in a wireless network depend largely on the locations of the BSs and the MTs. This is especially the case for 5G and beyond networks where the spatial distribution of emission is even more prominent than previous generations. In modern networks, with the number of transmitting nodes greatly increasing and small cells are being deployed to increase capacity in low-coverage areas, the network architecture can no longer be assumed as regular or deterministic. This has prompted the modeling of the network not as regular cells, but as a stochastic process of points either in two-dimensional or three-dimensional space.

Stochastic geometry is the area in mathematics that allow the analysis of such random models and as such, it is the go-to for more realistic representations of the wireless network. As such, it has been widely studied in the last decade by researchers in wireless networks mainly to study the performance of the network. In this dissertation, we introduce using the same method to study the EMF exposure in the 5G massive MIMO network.

4.1 Mathematical background

4.1.1 Poisson point process

Point processes are a collection of points randomly located on a mathematical space. Therefore, they have been widely used to model wireless network components like BSs, MTs, WiFi access points, etc. A point process can formally defined by [29] as follows: A point process is a countable random collection of points residing in a measure space, usually the Eucledian space $\mathbb{R}^d$. The associated $\sigma-$algebra is the Borel sets $\mathcal{B}^d$, and the measure is the Lebesgue measure.

Point processes can be characterized by counting the number of points falling in a set $A \subset \mathbb{R}$ as

$$\Phi = \{x \in \mathbb{R}^d : N(\{x\}) = 1\} \tag{4.1}$$

In wireless networks applications, the formalism of the *simple point process*, or sometimes called orderly point process, is usually used where a single point can exist at a given location. The counting measure of such point process is

$$N(\{x\}) \in \{0, 1\} \quad a.s. \quad \forall x \in \mathbb{R}^d \tag{4.2}$$

For simple point processes, the notion of *boundedly finite* point process is usually used. A point process is boundedly finite if and only if

$$|A| < \infty \implies \Phi(A) < \infty \tag{4.3}$$

The simplest point process to consider is the homogeneous Poisson point process (PPP) where for every compact set A, the point process $\Phi(B)$ has a Poisson distribution with mean $\lambda|B|$ where λ is the expected number of points per unit area, also known as the intensity of the PPP. Moreover, if the sets $A_1, A_2, \ldots, A_n$ are disjoint, then $N(A_1), N(A_2), \ldots, N(A_n)$ are independent random variables. The PPP Φ with intensity measure Λ can be defined by the joint probability distribution, for $A_i, \forall i = 1, \ldots, k$ being compact sets, as

$$\Pr\left[\Phi(A_1) = x_1, \ldots, \Phi(A_n) = x_k\right] = \prod_{i=1}^{k} \left(\exp\left(-\Lambda(A_i) \frac{-\Lambda(A_i)^{x_i}}{x_i!} \right) \right), \tag{4.4}$$

for k being a finite positive integer. This distribution is also called the finite-dimensional distribution (fidi) distribution.

The PPP, shown in Figure 4.1, has been widely used in many practical applications for the mathematical tractability of the models it produces. One expression resulting from 4.4, for $n = 0$ and $k = 1$, is of particular interest and is called the *void probability* function. It gives that for any subset A of Φ,

$$\Pr\left[\Phi(A) = 0\right] = \exp^{-\Lambda(A)}. \tag{4.5}$$

The void probability gives the probability that no points exist in A. It also represents the complementary cumulative distribution function (CCDF) of the *contact distance distribution*, or empty space distribution defined for a generap point process as

$$F(r) \triangleq \Pr[\|u, \Phi\| \leq r]. \tag{4.6}$$

The void probability function describes the distance distribution between a typical point and its nearest point in the PPP.

A homogeneous PPP can also be stationary if its distribution is translation-invariant, implying a constant intensity. It can be formulated as the following

$$\Pr[\Phi \in E] = \Pr[\Phi_x \in E] \quad \forall E, x, \tag{4.7}$$

where Φ_x is the point process Φ translated by $x \in \mathbb{R}^d$. Similarly, a PPP is *isotropic* if its distribution is rotationally invariant about the origin. A PPP that is both stationary and isotropic is called a *motion-invariant* point process.

A special case of the PPP for a fixed number of points n is the uniform binomial point process (BPP) Φ_B. The number of points in $C \subset W$ are identically and independently distributed on a compact set $B \subset \mathbb{R}^d$ according to a binomial distribution on B with parameters $n = \Phi_B(B)$, and $p = \frac{|C|}{|W|}$. And since the number of points is finite, the point

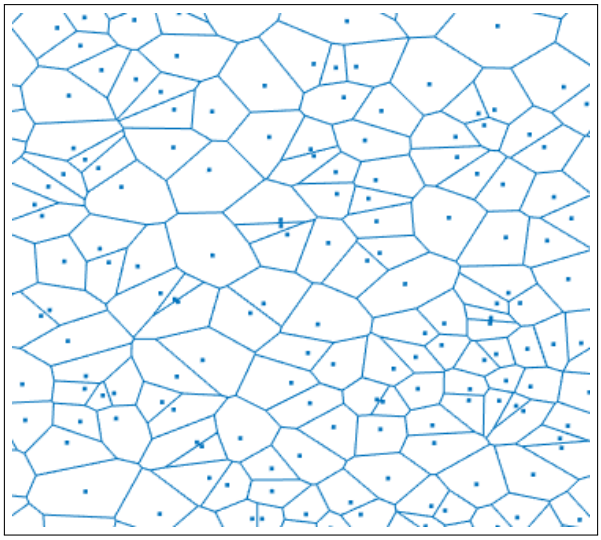

Figure 4.1: Representation of a Voronnoi tessellation of a Poisson Point Process

processes $\Phi_B(W \setminus C) = n - \Phi_B(C)$ and are therefore not independent.

In the last decade, modeling wireless nodes as PPP has been widely studied in the literature. Its mathematical tractability has allowed its usage in analyzing and optimizing the performance of said wireless networks. Many emerging technologies have also been studied by means of random distribution of wireless nodes to prove their functionalities, some notable examples are massive MIMO networks [30], [31], distributed antenna arrays [32], cell free massive MIMO [33]–[36], and heterogeneous networks [37], [38].

4.1.2 Useful theorems and definitions

Modeling the network as a point process, sums and products of functions evaluated at these points is essential. An obvious example is the interference on a wireless network is a sum over all interfering nodes. Equivalently, the total exposure at a particular MT is the sum of all emissions from all active transmitting nodes in the network. Ideally, we would like a complete statistical characterization of these sums and products, we often opt to obtain transforms of the random variables.

Campbell's theorem

Campbell's theorem is the most important result about the expectation of a sum on a point process. For a point process Φ on $\mathbb{R}^d$ and for $f : \mathbb{R}^d \mapsto \mathbb{R}$ being a measurable function, the random sum $S = \sum_{x \in \Phi} f(x)$ is a random variable with mean

$$\mathbb{E}[S] = \int_{\mathbb{R}^d} f(x)\Lambda(\mathrm{d}x). \tag{4.8}$$

For a stationary point process $\Phi \subset \mathbb{R}^d$ with intensity λ, Campbell's theorem reduces to

$$\mathbb{E}\left[S\right] = \lambda \int_{\mathbb{R}^d} f(x)\,\mathrm{d}x. \tag{4.9}$$

Probability generating functional

For a non-negative integer-valued random variable X, the moment generating function (MGF) M_X is defined as

$$M_X(t) = \mathbb{E}[t^X] = \int_{\mathbb{R}^d} t^n f_X(x)\,\mathrm{d}x. \tag{4.10}$$

This function can be used to compute the moments of the function. Most notably, the mean $\mathbb{E}[X] = \frac{\mathrm{d}M_X}{\mathrm{d}t}\ |_{t=0}$, and the variance $\mathrm{Var}[X] = \frac{\mathrm{d}^2M_X}{\mathrm{d}t^2}\ |_{t=0}$. We note that for X having a continuous PDF, $f_X(x)$, $M_X(t)$ is the two-sided Laplace transform of $f_X(x)$, and $M_X(-jt)$ is the characteristic function of X.

For a measurable function $v : \mathbb{R}^d \mapsto [0,1]$, the probability generating functional (PGFL) of a point process Φ is defined as

$$G[v] \triangleq \mathbb{E}\left(\prod_{x\in\Phi} v(x)\right) \tag{4.11}$$

for Φ being a PPP, the PGFL can be expressed as

$$G[v] = \exp\left(-\int_{\mathbb{R}^d}[1-v(x)]\Lambda(\mathrm{d}x)\right). \tag{4.12}$$

4.2 Cellular network modeling

For the last few years, cellular network modeling is shifting from the classical hexagonal model to a more random distribution of wireless nodes. In fact, It has been shown in [39] that the hexagonal model of modeling the BSs provides an upper bound of the coverage probability whereas PPP models provide the lower bound. Stochastic geometry, as a tool to analyze these random distributions, have shown great promise in describing an actual implementation of wireless networks. In [40] the distribution of the BSs of Paris has been shown to fit a $\beta-$Ginibre point process. And in [41] a promising method, called the inhomogeneous double thinning approach, have been developed that aims to represent existing wireless networks as known point processes.

These models of the spatial distribution of the BSs in the network can be complemented by realistic and/or relevant channel and transmission models to get a more realistic representation of the wireless network, or to study the behaviors of certain technologies or scenarios. In this section, we introduce the different concepts of modeling a wireless

network, like antenna gains, transmission channels, path loss models, and other relevant parameters. We then derive an expression for the average total power received in a simple network.

4.2.1 Path-loss model

Single-state unbounded PL Model

The unbounded path-loss model, also called unbounded PL model, is the most common and simplest one. Defining r as the distance between the transmitting BS and the receiver, we can define the path-loss as follows

$$\beta(r) = \kappa r^{-\alpha}, \tag{4.13}$$

where κ is the PL constant, and $\alpha > 2$ is the *path-loss coefficient*, also called the *path loss exponent*.

While this model is the simplest for the mathematical framework, it introduces a singularity for the received power at the MT when $r \to 0$. This model also assumes transmission in the far-field which is not the case for lower values of r. To overcome these shortcomings, we opt to use a *bounded path-loss model*. Another problem with this model is the shortcoming when considering the LoS and NLoS since it assumes the same exponent $\alpha_{LoS} = \alpha_{NLoS} = \alpha$.

Single-state bounded PL model

A solution to the singularity problem in unbounded PL models is its bounded counterpart. The bounded PL model can be achieved either by using the max function or adding a factor to the distance between the BS and the MT. A bounded PL model can be formulated as

$$\beta(r) = \kappa \max(d, r)^{-\alpha}. \tag{4.14}$$

Other forms of bounded PL models exist like $\beta(r) = \kappa \max(d, r^{-\alpha})$, or $\beta(r) = \kappa(1 + r^{-\alpha})$.

Dual-state PL model

The dual state PL model assumes two path loss exponents, α_L and α_N for LoS and NLoS propagation channels respectively. The model is expressed as follows

$$\beta = \begin{cases} \kappa_L r^{-\alpha_L} & \text{in LoS} \\ \kappa_N r^{-\alpha_N} & \text{in NLoS} \end{cases} \tag{4.15}$$

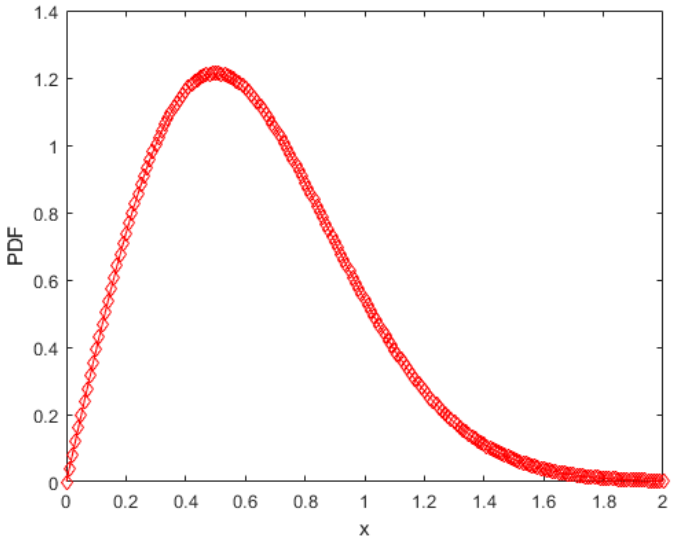

Figure 4.2: Representation of the Rayleigh distribution for $\sigma = 0.5$

where κ_s is the path-loss constant for $s \in L, N$. Each state has a probability P_L which is the probability that the MT is in LoS or NLoS of the BS. The dual-state PL model can be either bounded or unbounded by using any of the techniques presented before in this section.

4.2.2 Small-scale channel fading

A fading model is the mathematical formulation of the effects of the transmission channel on the amplitude and phase of the transmitted signal. While path-loss, which represents slow changes in the signal, is represented by the path-loss model previously discussed, small-scale fading represents the rapid changes of amplitude and phase of the signal usually due to multi-path and is commonly represented by statistical distributions. The most popular distribution for modeling the small-scale fading is the Rayleigh distribution presented in Figure 4.2, and is used to represent what is called Rayleigh fading channel [42]. The Rayleigh distribution has the PDF

$$f(x) = \frac{x}{\sigma^2} e^{\frac{-x^2}{2\sigma^2}} \tag{4.16}$$

Multi-path propagation results from the signal getting reflected by numerous obstacles between the transmitter and the receiver. Each path will have its own Doppler shift, path attenuation, and time delay resulting in a linear, time-varying channel. Such channel, when no dominant path exists, can be represented by the Rayleigh fading channel. This results from the fact that the envelope of the received signal follows the Rayleigh distribution. When a dominant path exists, usually a LoS path, the small-scale fading

channel is often described by the Rician distribution [43].

4.2.3 The total received power

We consider a two-dimensional downlink (DL) cellular network where the BSs are distributed according to a PPP denoted by Φ having an intensity λ. Base stations are distributed in a 2D plane following a PPP Φ_{BS} with intensity λ_{BS}. The MTs are assumed to be uniformly distributed in the cell. The system is assumed to be in full buffer mode, which is an acceptable conservative assumption for exposure estimation, and users are being served over the whole transmission period.

The simplest path-loss coefficient model a single-slope path loss model, $\beta = max(m, r^{-\alpha})$. Where, α is the path loss exponent and r is the distance between the MT and the BS. We also ignore the transmission noise and shadowing effects. We also assume a constant antenna gain G.

For a NLoS channel, the default small-scale fading coefficient is assumed to vary according to a Rayleigh distribution. A Rayleigh fading channel can be modelled by independent and identically distributed (i.i.d.) complex Gaussian random variable with zero mean and variance σ, $h \sim \mathcal{CN}(0, \sigma)$. For this type of channel, the channel gain, $|h|^2 \sim Ex(1/\sigma)$, will be exponentially distributed with mean σ.

The exposure can be calculated by summing the received power at a certain point in space from the serving base station and from all other interferers. The expression of the total received power at a typical MT is as follows

$$\mathcal{E} = \sum_{r_i \in \Phi_{BS}} P_{tx} |h|^2 G_{tx} r^{-\alpha}, \tag{4.17}$$

where P_{tx} is the transmit power from the BSs, $|h|^2$ is the small-scale fading channel gain, and G_{tx} is the antenna array gain. To determine the CDF of the exposure, we first determine the MGF defined as $\Phi_{\mathcal{E}}(t) = \mathbb{E}[\exp(jt\mathcal{E})]$. The MGF can be expressed as

follows

$$\varphi(t) = E\left[\exp\left(jt\sum_{r_i\in\phi_{BS}} P_{tx}\left|h\right|^2 G_{tx} r^{-\alpha}\right)\right] \tag{4.18}$$

$$\overset{(a)}{=} E_r\left[\prod_{x\in\Phi_{BS}} E_{|h|^2}\left[\exp\left(j\ t\ P_{tx}\ \left|h\right|^2\ G_{tx}\ r^{-\alpha}\right)\right]\right] \tag{4.19}$$

$$\overset{(b)}{=} E_r\left[\prod_{x\in\Phi_{BS}} \frac{1}{1-\frac{jtP_{tx}G_{tx}}{r_i^{\alpha}}}\right] \tag{4.20}$$

$$\overset{(c)}{=} \exp\left(2\pi\lambda\int_m^{\infty} \frac{jtP_{tx}x}{x^{\alpha}-jtP_{tx}}\,\mathrm{d}x\right) \tag{4.21}$$

$$\begin{aligned}= \exp\Bigg[\Bigg(&-2\pi\lambda BW\ G\ P_G\ \frac{jtP_{tx}G\bar{\gamma}m^{2-\alpha}}{\alpha-1}\times \\ &{}_2F_1\left(1,\frac{\alpha-2}{\alpha},2-\frac{2}{\alpha},jtP_{Tx}G\ BW\ P_G\ \bar{\gamma}m^{-\alpha}\right)\Bigg)\Bigg]\end{aligned} \tag{4.22}$$

Here, (a) follows from conditioning $|h|^2$ and r, (b) follows from the PDF of the exponential distribution, and (c) from the PGFL 4.12 of a PPP. Where ${}_2F_1(a,b,c,z)$ is the Kummer confluent hypergeometric function defined in [44], α is the path loss exponent, BW is the beamwidth, λ is the PPP intensity, G is the average gain, P_{tx} the transmit power, and m the minimum separation distance between the BS and the MT to avoid infinite values at the BS location.

The CDF of the exposure can be determined using the Gil-Peleaz theorem [45] defined as follows

$$F(x) = \frac{1}{2} - \frac{1}{\pi}\int_0^{\infty} \frac{Im\left[e^{-jtx}\varphi(t)\right]}{t}dt. \tag{4.23}$$

The result obtained from applying the PGFL to 4.22 is verified with Monte-Carlo simulations as shown in Figure 4.3. In the Monte-Carlo simulation, the network was modeled as having 2000 points, on average, representing the BSs randomly distributed in the two-dimensional plane following a PPP in an area $R_{network}$ satisfying BS density λ. The total power is the sum of all powers received from the different BSs using the already defined path-loss model and modeling each channel as complex Gaussian. The simulation was performed over 5×10^4 runs and lasted ~ 1 minute.

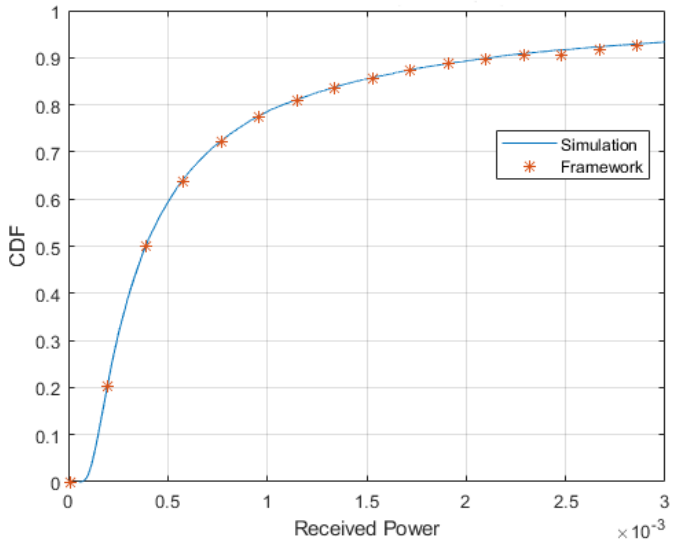

Figure 4.3: Cumulative distribution function of the total power received

Using this approach, studying the trends of the EMF exposure for different BS densities. The superposition of multiple independent networks is also simple just by summing the multiple BS point processes. This model however, is representative of the 5G network. As we discussed in the previous chapters, the usage of massive MIMO antennas will be widespread in future network. Here, the characteristics of massive MIMO antennas and 5G, like beamforming, MIMO channels, mmWave, and multi-user transmission, are not considered. In the following chapters we introduce more relevant models that considers important 5G network parameters.

Chapter 5

A Statistical Estimation of 5G Massive MIMO Networks' Exposure Using Stochastic Geometry in mmWave Bands

Contents

As discussed in the previous chapter, a simplistic classical network model is not representative of 5G massive MIMO transmission and will result in over-conservative exposure values. In this chapter, we aim to prove this claim by using more realistic channel and antenna models to derive a closed-form expression of the distribution of the total power receiver at the typical user in a massive MIMO network in mmWave, and by comparing the obtained results to the simplistic model derived in the previous chapter. In this chapter, we assume that the BSs and the MTs are distributed following a PPP. The power received at the transmitter is modeled as a shot-noise process with a modified power law. The distributions of 5G massive MIMO antenna gain and channel gain were obtained by fitting simulation results from the NYUSIM mmWave channel simulator [46]. The fitted distributions, e.g., exponential and gamma distribution for antenna and channel gain respectively, were then implemented into an analytical framework and validated by Monte-Carlo simulations. We then perform sensitivity analysis to investigate the impact of key parameters, e.g., BS density, path loss exponent, and transmission probability.

5.1 Introduction

The explosive growth in communication devices in the last decade pushed the industry towards exploiting the existing communication spectrum. The recent mass-deployment of Internet of Things (IoT) devices paired with increasing demand for quality in the streaming and entertainment industries made satisfying these requirements using the same spectrum particularly challenging. To ensure that the huge spectrum capacity required to maintain a stable communication system is met, the industry started shifting with the design of 5G networks to millimeter-wave (mmWave) frequency bands. For indoor communication, mmWave bands are already in use, e.g., IEEE 802.11ad [47]. However, mmWave channels are fundamentally different from Ultra High Frequency channels used for existing cellular communication protocols, they have higher propagation loss in air, and low penetration for construction materials and foliage [48]. The high path loss in mmWave frequencies makes it necessary to implement methods to increase the received power at the mobile terminal (MT) in order to maintain an acceptable signal-to-noise ratio (SNR) to decode the signal. One way of increasing the SNR is by increasing the gain at the base station (BS). Therefore, beamforming became one of the essential technologies for 5G mmWave communication. The usage of a large number of radiating elements at the antennas will allow them to emit signals in fast-varying, high-gain beams focused on the desired MT, while simultaneously decreasing the interference to other MTs. Exposure compliance assessments are performed by manufacturers and operators to ensure that emitting devices are compliant with safety regulations concerning human exposure to electromagnetic fields. Safety regulations concerning human exposure to EM fields have been specified by International Commission on Non-Ionizing Radiation Pro-

tection (ICNIRP) [49] and IEEE [50]. Multiple studies have been made over the years to characterize the exposure in current and legacy communication systems which are based on assuming the maximum theoretical power emitted for the antenna. However, these characterizations struggle to stay accurate for 5G and future technologies due to the fundamental differences between the systems. In [51] and [52], it has been shown that the actual power contributing to the electromagnetic field exposure is much lower than the theoretical maximum. This is due to the uncertainty in the values of the emitted and received power from a massive MIMO antenna deploying beamforming. The spatio-temporal variation of the antenna pattern, and its dependency on the MT distribution and channel characteristics make the transition to statistical methods for the exposure estimation a necessity if accurate estimations are desired. Statistical analysis of cellular networks' exposure has been a case study for the last couple of years, using simulations to model the behavior of the channel and the transmission e.g., in [53], but accurate analytical analysis is yet to be performed.

5.1.1 Our approach and contributions

The mathematical approach to analyzing cellular systems is often considered as a promising solution [54]. However, for cellular networks, analytical tractability has been proven by relying on the methodology of stochastic geometry while modeling the BSs using point processes. Stochastic geometry has been widely applied in the field of communication theory, and it has proven that it is a powerful approach in conducting performance analysis and solving optimization problems. Examples of the usage of stochastic geometry in modeling cellular networks can be found in [19–24]. In this study, we model the locations of the base stations in the network as identically and independently distributed following a homogeneous Poisson point process (PPP).

In this chapter, we use the active antenna model developed by 3GPP [55], [56], which assumes a uniform rectangular array antenna, for communication in bands above 6 GHz. As for the channel model, we use the NYUSIM statistical mmWave channel simulator [1], which is backed by extensive measurements in the mmWave band, and was shown to be better suited for above 6 GHz frequencies [57]. Multiple large-scale channel measurements have been performed in the mmWave band over the last few years [14], [58]–[60], and multiple studies compared the different channel models used by the different standardization bodies as in [54], [57].

In this chapter, we fitted the channel gain and the antenna gain into statistical distributions based on channel simulations from NYUSIM and the 3GPP antenna array model. We determined the closed-form expression of the MGF for the exposure in the network, which is equivalent to the total power received at a certain MT location, with which we compute its cumulative distribution function (CDF). We analyzed the behavior of the

90th percentile of the exposure for different network parameters. We showed the comparison between this model and a simplified, less accurate, model with simple antenna and channel models in [61]. We performed a sensitivity analysis on the exposure expression to show the impact of each parameter on the global exposure. The list of the symbols used in the chapter is presented in Table 5.1.

5.2 System model

The aim of this study is to determine the closed-form equation of the electromagnetic field exposure in a 5G massive MIMO cell emitting in the mmWave band. The base stations are modeled as points of a stationary and isotropic Poisson point process Ψ_{BS} with density λ_{BS}. The locations of said points are denoted by $x \in \Psi_{BS} \subseteq \mathbb{R}^2$. The MTs are distributed uniformly and independently in a bounded region of $\mathbb{R}^2$ and thus, in addition to the assumption on the BS distribution, we can generalize the distribution of the exposure over the whole cell area and the framework can be developed for a typical MT denoted by MT_0 located at the origin without losing generality. To investigate the effect of the network load on the exposure, we assume that the BSs emit with probability α, i.e., at a certain time-frame the number of active MTs is less than the number of base stations $\lambda_{MT}^{active} \leq \lambda_{BS}$, which means that the BSs will have an effective density of $\lambda_{eff} = \alpha\ \lambda_{BS}$. Since line-of-sight (LOS) paths are the highest contributors to the exposure, we assume that all the paths between the BS and the MT are LOS paths. The BSs will emit with a constant power denoted by P_{tx}. We assume a 5G massive MIMO network where the BSs are composed of antenna arrays with identical structure, and thus identical radiation patterns. The BS is assumed as single-user MIMO, and it emits towards one MT in a single time slot. We assume no downlink power control exist in the network, which seems to be the case for 5G networks [62], so every MT is being allocated the whole power resource for each transmission slot. We implement the channel model NYUSIM, developed by New York University Wireless Group [46] which divides the channel power into clusters and paths between the BS and the MT. The received power $P_{rx}^{BS_i}$ at each MT is dependent on the transmitted power, the propagation distance, the channel gain, and the antenna gain. The global exposure P_{rx}^{t} can then be defined as $P_{rx}^{t} = \sum_{BS_i \in \Psi_{BS}} P_{rx}^{BS_i}$ and it can be rewritten as

$$P_{rx}^{t} = \sum_{BS_i \in \Psi_{BS}} P_{tx} H_i G_i L_i, \tag{5.1}$$

where H_i, G_i, and L_i are the link's channel gain, antenna gain, and path loss, for the link between the MT to the i^{th} BS, respectively. To better analyze the distribution of total received power P_{rx}^{t}, we focus on studying the CDF of total received power, which is defined as

Symbol	Description
P_{rx}^{t}	Total Power Received at the center of the cell
$P_{rx}^{BS_i}$	Power received from the i^{th} BS at the center of the cell
P_{tx}	Transmitted power from all the BSs
$H_i,\ G_i$	Channel and antenna gain from the i^{th} BS to the MT
L_i	Path loss experienced by the transmitted signal from the i^{th} BS to the MT
$\theta,\ \phi$	Zenith and azimuth angles in the local coordinate system centered at the origin of the array
$A_E,\ A_{E,V},\ A_{E,H}(\theta,\phi)$	Radiation pattern and its vertical and horizontal components respectively
$\theta_{3dB},\ \phi_{3dB}$	Vertical and horizontal beamwidths of the antennas in degrees
$min[x_1, x_2 \dots]$	Numerically smallest number of x_k
A_m	Antenna's front-to-back ratio
$SLA_V,\ SLA_H$	Vertical and horizontal sidelobe attenuation levels
$A_A(\theta,\phi)$	Array pattern of the antenna
$v_{m,n}$	Phase shift due to the $[m,n]$ antenna element placement
$w_{m,n}$	Weighting factor due to the $[m,n]$ antenna element
$N_H,\ N_V$	Number of horizontal and vertical antenna elements
$\theta_{etilt},\ \phi_{escan}$	Zenith and azimuth electrical down-tilt steering angle
$d_v,\ d_H$	Vertical and horizontal antenna element spacing
$\Gamma(b)$	Gamma function $\Gamma(b) = \int_0^\infty x^{b-1}e^{-x}dx$, $\Re(b) > 0$
Ψ_{BS}, λ_{BS}	The Poisson point process and its density describing the BS distribution in the cell
$\mathbb{E}_k[.]$	Expectation with respect to the random variable k
λ_{MT}^{active}	Density of the active MTs in the cell
α	Emission probability of the BSs
MT_0	Mobile terminal at the center of the cell
r_i	the distance between BS_i and MT_0
η	Path loss exponent assumed constant in the whole cell
$\varphi_X,\ \Phi_X$	MGF and characteristic function of the random variable X
$F_X(x)$	CDF of the random variable X
$\Gamma(a,x)$	Upper incomplete gamma function
$\gamma(a,x)$	Lower incomplete gamma function
K	Iid random variable describing the channel and antenna gains
${}_2F_2(a_1,a_2,b_1,b_2,z)$	Generalized hypergeometric function

Table 5.1: List of symbols used in antenna pattern and model derivation

$$F_{P_{rx}^t}(x) = Pr\left\{P_{rx}^t \leq x\right\}, x \in [0, +\infty) \tag{5.2}$$

In the following subsections, we describe the system model, including the antenna array gain, the channel gain, and derive the expression to compute the CDF of the exposure of the assumed network.

5.2.1 Path Loss Model

In this chapter, a two-state path loss model is considered. It is modeled as a shot noise process with a modified power law [63]. We divide path loss into two regions, with $r < R_0$ and $r \geq R_0$. The explicit expression for path loss $L_i\ (r_i)$ for the link between MT and ith BS is denoted as

$$L_i\ (r_i\ ) = (K_i, r_i < R_0 K_i r_i^{-\eta}, r_i \geq R_0) \tag{5.3}$$

where r_i is the distance between BS$_i$ and MT$_0$, and η is the path loss exponent assumed constant in the network. K is an independently distributed random variable drawn from a common distribution and independent of r. It accounts for the transmitted power, the channel gain and the antenna gain for the ith link, defined as $K_i = P_{rx} H_i G_i$. The details of H_i and G_i are presented in the following subsections.

Remark 1. *In this chapter, we adopt this two-state path loss model, which has already included the simpler case by setting $K(r < R_0) = 0$ used in the authors' previous work [61]. In the region where $r < R_0$, we approximate the path loss with a constant which can be interpreted as a rough average of the attenuation in the near-field region while for $r > R_0$, the power law decay model is used.*

5.2.2 Antenna model

We implement the 3GPP active antenna model used to model the channels above 6 GHz [55]. The model can be used on frequencies up to 100 GHz. We have implemented the 3D model (2D steering) with steering in both elevation and azimuth since both scanning directions will be exploited in mmWave antennas [64]. The total antenna radiation pattern is the combination of the radiating element's radiation pattern and the array factor. The modeling of the antenna array is explained in the following subsections.

Element pattern

By denoting θ and ϕ as the zenith and azimuth angles in the local coordinate system centered at the center of the antenna array, respectively, and defined as $0° < \theta < 180°$

and $-180^\circ < \phi < 180^\circ$, we can express the radiation pattern A_E of an antenna element as

$$A_E(\theta, \phi) = -\min\left[A_{E,V}(\theta) + A_{E,H}(\phi),\ A_m\right] \tag{5.4}$$

where $A_{E,V}$ and $A_{E,H}$ are the vertical and horizontal radiation patterns of the array element, expressed as

$$A_{E,V}(\theta) = -min[12((\theta - 90^\circ)/\theta_{3dB})^2, SLA_V] \tag{5.5}$$

and

$$A_{E,H}(\phi) = -min\left[12\left(\frac{\phi}{\phi_{3dB}}\right)^2, A_m\right] \tag{5.6}$$

where, θ and ϕ are the zenith and azimuth angles respectively in the local coordinate system centered at the center of the antenna array and defined as $0^\circ < \theta < 180^\circ$ and $-180^\circ < \phi < 180^\circ$. $\theta_{3dB} = \phi_{3dB} = 65^\circ$ are the 3 dB vertical and horizontal beamwidths of the antenna, $SLA_V = SLA_H = 30\ dB$ are the vertical and horizontal sidelobe attenuation levels, respectively, and $A_m = 30\ dB$ is the antenna's front-to-back ratio.

Array pattern

Implementing a large number of antenna elements in the array will allow high-gain transmission of power towards the served MT by concentrating the field intensity in the direction of transmission [65]. The interference of the transmitted electromagnetic fields will form points of high intensity in certain directions, while producing low intensity transmissions towards unwanted directions. The array pattern is determined according to the physical implementation of the antenna elements and the electrical steering of the main beam. The array's radiation pattern A_A is determined using the element radiation pattern A_E in (5.4), and assuming a uniformly spaced rectangular array (URA) in the horizontal and vertical dimensions with identical element radiation pattern as in

$$A_A(\theta, \phi) = A_E(\theta, \phi) + 10log_{10}\left[1 + \rho\left(\left|\sum_{m=1}^{N_H}\sum_{n=1}^{N_V} w_{m,n} v_{m,n}\right|^2 - 1\right)\right], \tag{5.7}$$

where $v_{m,n}$ is the phase shift due to the antenna element placement, $w_{m,n}$ is the weighting factor which provides the electrical down-tilt and attenuation of the antenna's sidelobes, and N_H and N_V are the number of horizontal and vertical antenna elements respectively. As it is shown in (5.9), w is dependent on the antenna steering angles, the electrical down-tilt steering angle θ_{etilt} and the electrical horizontal steering angle φ_{escan}, and since we assume that the main beam of the antenna is centered towards the receiving MT, the antenna array will have a different radiation pattern towards each MT depending on their location. The 2D slice of the antenna pattern on the azimuth plane for a 16 $\times$

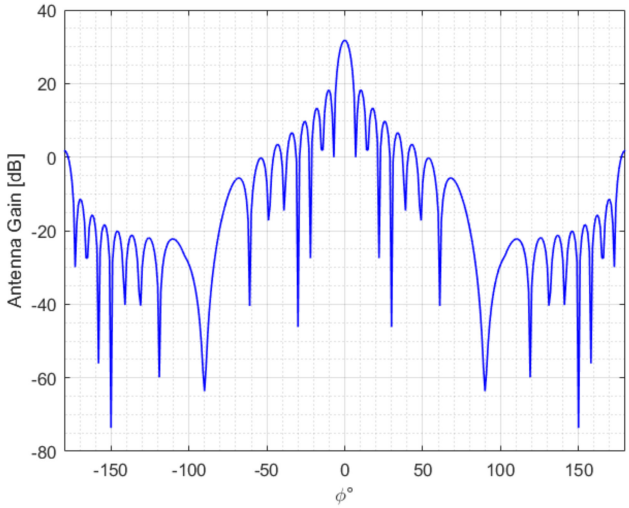

Figure 5.1: 2D slice of the 3D antenna pattern realization of the 3GPP active antenna array model with 256 antenna elements directed perpendicularly to the antenna array over the steering angles in the azimuth and elevation.

16 array can be presented as in Figure 5.1.

$$v_{m,n} = exp\left(2\pi i\left((n-1)\frac{d_V}{\lambda}cos(\theta) + (m-1)\frac{d_H}{\lambda}sin(\theta)sin(\phi)\right)\right) \tag{5.8}$$

$$w_{m,n} = \frac{1}{\sqrt{N_H N_V}}exp\left(2\pi i\left((n-1)\frac{d_V}{\lambda}sin(\theta_{etilt}) - (m-1)\frac{d_H}{\lambda}cos(\theta_{etilt})sin(\phi_{escan})\right)\right) \tag{5.9}$$

$$m = 1, 2, \ldots\ N_H \tag{5.10}$$

$$n = 1, 2, \ldots\ N_V \tag{5.11}$$

5.2.3 Channel model

In our model, we separate the two gains obtained from the channel simulation into channel gain obtained directly from the NYUSIM channel simulation, and antenna gain obtained by determining the antenna radiation pattern for every scanning angle after each channel simulation. Using the NYUSIM channel simulator, we determine, in each simulation, the LOS link characteristics between the serving antenna and the receiving MT. From that link, we can determine the channel gain, and the angles of departure (AoD) from the BS towards the MT. The AoDs are then used to determine the array gain using the 3GPP active array model [55], modeled in Section 5.2.2 The antenna gain for each beam can be determined from this model, according to its AoD, as shown in the realization in Figure 5.1. We assume that the antennas are deployed in an urban

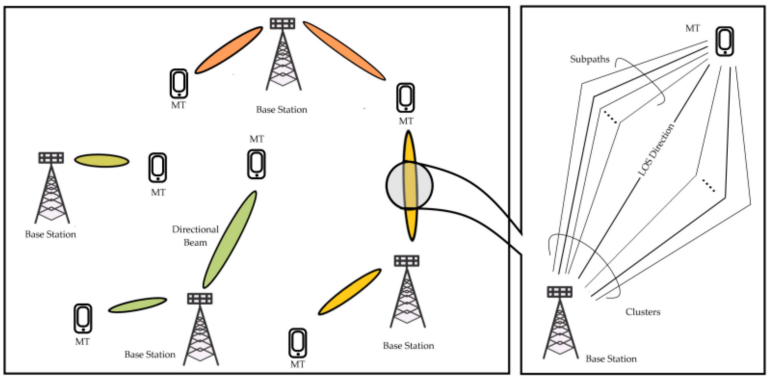

Figure 5.2: Illustration of our mmWave model (left) and the channel model (right). The channel model follows the NYU Wireless Group mmWave channel model in [46].

Parameter	Value
Frequency	$28\,GHz$
Scenario	UMI
Tx Power	$0\,dBm$
Array type	URA
Number of elements	256
Antenna spacing	$0.5\,\lambda$
Half-Power Beamwidth	$10°$
Link Type	LOS
RF Bandwidth	$800\,MHz$
MT Terminal Height	$1.5\,m$
Base Station Height	$35\,m$

Table 5.2: NYUSIM simulation parameters used for the channel simulations.

microcell (UMI) scenario. The channel model is presented in Figure 5.2. The parameters used for the channel simulation are presented in Table 5.2. Running a large number of simulations, we empirically fitted the distributions of the gain components into statistical models. We chose the distributions for the channel and antenna gain by determining the best fit out of the common distributions using MATLAB. The distributions' parameters summarized in Table 5.3 were determined accordingly.

Parameter	Value	Description
a	0.57	Gamma distribution shape parameter
b	1.45	Gamma distribution scale parameter
c	966.5	Exponential distribution exponent

Table 5.3: Parameters of the fitted distributions. a for the exponential distribution and b, c for the gamma distribution

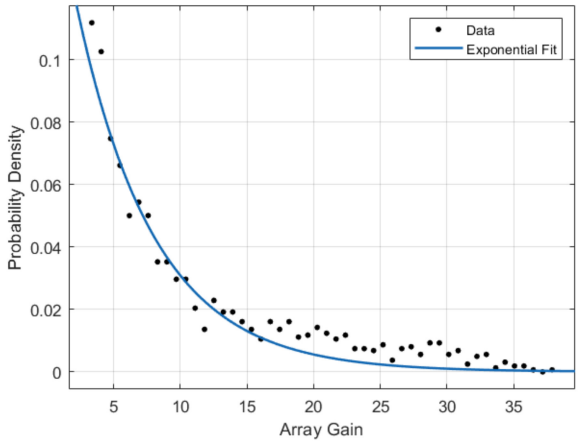

Figure 5.3: Plot of the fit of the antenna array gain into an exponential distribution for a rectangular uniform antenna array with $N_{tx} = 256$ antenna elements.

Array gain

Using the AoDs from the simulated paths in NYUSIM we have determined, for each path, the array gain g towards each specific MT. The distributions of the array gain G using the 3GPP active antenna array model, presented in Figure 5.3, has been fit into an exponential distribution with probability density function (PDF) f_G defined as

$$f_G(g) = ae^{-ag}. \tag{5.12}$$

Channel gain

Channel gain h is the gain produced by the exploitation of the channel between the Tx and Rx such as the diversity gain, multipath, hardening, etc. [46]. This corresponds to the sum of the gains of the different subpaths in NYUSIM channel model. We fitted the channel gain H into a gamma distribution, as shown in Figure 5.4, with PDF f_H given in (5.13). The parameters for the fit gain distributions are summarized in Table 5.3.

$$f_H(h) = \frac{1}{\Gamma(b)\, c^b} h^{b-1} e^{-h/c} \tag{5.13}$$

5.3 Exposure estimation

In this section, we derive the analytical framework based on the system model of the 5G network given in Section . Since the distribution of P_{rx}^t is unknown, we adopt the Gil-Pelaez inversion theorem [66] to compute the CDF defined in (5.2), which is based on characteristic function of random variable P_{rx}^t. The CDF P_{rx}^t is given by

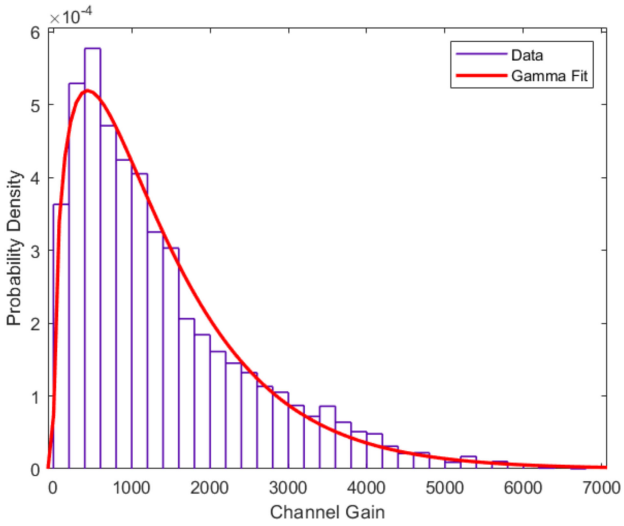

Figure 5.4: Channel gain fit into a gamma distribution for MTs uniformly distributed on a 2D plane and having a single element antenna array.

$$F_{P_{rx}^t}(x) = \frac{1}{2} - \frac{1}{\pi}\int_0^\infty \frac{1}{t} Im\left[e^{-jtx}\Phi_{P_{rx}^t}(t)\right] dt \tag{5.14}$$

where $\Phi_{P_{rx}^t}(t)$ represents the characteristic function of P_{rx}^t, which can be derived from moment-generating function as $\Phi_{P_{rx}^t}(t) = \varphi_{P_{rx}^t}(jt)$. The MGF (MGF) of a random variable, defined as $\varphi_X(x) := \mathbb{E}\left[e^{tX}\right]$, $\forall\, t \in \mathbb{R}$, is an aLTErnative representation of the random variable other than its probability distribution. It can be used to determine the distribution's moments as $\mathbb{E}[X^n] = \frac{d^n\varphi_X(x)}{dx^n}\Big|_0$, $\forall\, n \in \mathbb{R}$. Since the expected value of the distribution is determined by derivation of the MGF in comparison to integrating the probability density, using the MGF becomes more attractive for complicated random variables thanks to the simpler operation. Following the path loss model defined in (6.2), the total power at the MT_0 can then be represented by: $P_{rx}^t(t) = \sum_{i\in\Pi} \mathcal{B}_i f(K_i, r_i)$. Where $\mathcal{B}_i$ is a set of random variables such that $P(\mathcal{B}_i = 1) = 1 - P(\mathcal{B}_i = 0) = \alpha$. Since we divided the space into two regions, the total power received in the whole region can be written as $P_{rx}^t = P_{rx}^{in} + P_{rx}^{out}$ where P_{rx}^{in} is the total power received from transmitters within distance R_0 from the MT, and P_{rx}^{out} is the total received power from transmitters at distances greater than R_0. To account for transmission gain, we assume that K_i is drawn from the distribution having the PDF: $f_K(k) = f_G(g).f_H(h)$. Where, G and H are the antenna gain and the channel gain distributions, respectively. As mentioned in 2.2., we fit the antenna gain into an exponential distribution with PDF $f_G(g) = ae^{-ag}$, and the channel gain into a gamma distribution with PDF $f_H(h) = \frac{1}{\Gamma(k)\theta^k}h^{k-1}e^{-h/c}$. The MGF of this model is presented in Theorem 1.

Theorem 1. *The MGF of the exposure in the network modeled in Section 5.3, given the*

array gain and channel gain in (10) and (11) is formulated as:

$$\varphi(s) = \exp(\pi\lambda\alpha\Theta), \tag{5.15}$$

where,

$$\begin{aligned}\Theta = 1 &- \left(\frac{a}{\widetilde{P}}\right)^{b} e^{\frac{a}{\widetilde{P}}}\Gamma\left(1-b, \frac{a}{\widetilde{P}}\right) - \pi\frac{2}{\eta}\left(\frac{\widetilde{P}}{a}\right)^{\frac{2}{\eta}} \frac{\csc\left(\pi\frac{2}{\eta}\right)\Gamma\left(b+\frac{2}{\eta}\right)}{\Gamma(b)} \\ &+ (-1)^{b}\frac{\pi b}{\Gamma(b)}\left(-\frac{c}{a}\right)^{\frac{2}{\eta}}\csc(\pi b)\gamma\left(b+\frac{2}{\eta}, -\frac{a}{\widetilde{P}}\right) \\ &+ \frac{\eta}{2\Gamma(b)}\Bigg[-\left(\frac{c}{x}\right)^{\frac{1}{2}}\Bigg((-1)^{b}\frac{2}{\eta}\left(-\frac{x}{a}\right)^{\frac{2}{\eta}}\pi\csc(\pi b)\gamma\left(1+b+\frac{2}{\eta}, -\frac{a}{\widetilde{P}}\right) \\ &- \left(\frac{xc}{a\widetilde{P}}\right)^{\frac{2}{\eta}}\Omega(b+1)\Bigg) + \Omega(b)\Bigg]\end{aligned} \tag{5.16}$$

and

$$\Omega(x) = \left(\frac{a}{c}\right)^{2/\eta}\Gamma(x)\ {}_2F_2\left(\{1,\ 2/\eta\}, \{1-x, 1+2/\eta\}, \frac{a}{s\ c\ P_{tx}}\right) \tag{5.17}$$

and where, $\widetilde{P} = scP_{tx}, \Gamma(a,x) = \int_x^\infty t^{a-1}e^{-t}dt$ *is the upper incomplete gamma function,* $\gamma(a,x) = \int_0^x t^{a-1}e^{-t}dt$ *is the lower incomplete gamma function [67],* ${}_2F_2$ *is the generalized hypergeometric function defined as* ${}_pF_q = \sum_{k=0}^{\infty}\frac{\prod_{j=1}^{p}(a_j)_k z^k}{\prod_{j=1}^{q}(b_j)_k k!}$*, and* $\Gamma(x) = \int_0^\infty t^{x-1}e^{-t}dt$ *is the standard gamma function.*

Proof. The total exposure assuming the emission as shot noise process $f(K,r) = Kr^{-\eta}$ for $A < r < B$, and Poisson distribution of transmitters, can be written as $P_{rx}^{t}(r) = P_{tx}\sum_{\mathrm{BS}_i\in\Psi_{BS}} K_i r_i^{-\eta}$ continuing from (5.1) for $K_i = H_iG_i$. We let K_i be drawn from a discreet set $\{K_i\}$ so that the shot noise process can be written as sum of independent shot noise processes $P_{rx}^{i}(r) = P_{tx}\sum_j\ f(K_i, r-r_j)$. The MGF of P_{rx}^{i} can be determined by solving (5.20). As per the result in [63], we can obtain the form in (5.21) for a continuous set of K_i, and using the probability generating functional (PFGL) of a poisson point process. Simplification by integrating by parts gives the form in equation

$$\varphi(s) = \mathbb{E}\left[e^{-sP_{rx}^{i}(r)}\right] \tag{5.18}$$

$$= \mathbb{E}_K\left[\exp\left(-sP_{tx}\sum_{\mathrm{BS}_i\in\Psi_{BS}}\sum_j K_i(r-r_j)^{-\eta}\right)\right] \tag{5.19}$$

$$\overset{\text{PGFL}}{=} \exp\left\{-\mu\int_A^B \mathbb{E}_K\left[1-\exp\left(-sP_{tx}Kr^{-\eta}\right)\right]\ dr\right\} \tag{5.20}$$

The MGF of the exposure then can be represented by the product of the two independent MGFs $\varphi(s) = \varphi_{in}(s)\,\varphi_{out}(s)$, where φ_{in} can be obtained by substituting $A = 0$, and

$B = R_0 = 1$ in (5.20). Likewise, for $A = 1$ and $B = \infty$, φ_{out} can be expressed by

$$\varphi_{out}(s) = \exp\left(\pi\lambda\alpha\left[\mathbb{E}_K\left[1 - e^{-sP_{tx}K}\right] - s^{2/\eta}\,\mathbb{E}_K\left[(P_{tx}K)^{2/\eta}\right]\Gamma(1-2/\eta) + s^{2/\eta}\,\mathbb{E}_K\left[(P_{tx}K)^{2/\eta}\,\Gamma(1-2/\eta, sP_{tx}K)\right]\right]\right) \tag{5.21}$$

The expression of φ_{out}, (5.21) can be rewritten into (5.22), replacing the expectations with their integral forms. Each component can then be determined as presented below to obtain the closed-form expression

$$\varphi_{out}(s) = \exp\left(\pi\lambda\alpha\left[1 - \int_0^\infty e^{-skP_{tx}} f_K(k)\,dk - \Gamma(1-2/\eta)\;(sP_{TX})^{2/\eta}\int_0^\infty k^{2/\eta} f_K(k)\,dk + (sP_{tx})^{2/\eta}\int_0^\infty k^{2/\eta}\Gamma(1-2/\eta, skP_{tx})\;f_K(k)\,dk\right]\right) \tag{5.22}$$

To determine the PDF of K, $f_K(k)$, we first determine the CDF $F_K(k)$ of K as follows

$$\begin{aligned}
F_K(k) &\stackrel{\text{def}}{=} \mathbb{P}(K < k) && (5.23)\\
&= \mathbb{P}(GH \le k) && (5.24)\\
&= \mathbb{P}(GH \le k,\ G \ge 0) + \mathbb{P}(GH \le\ k,\ G \le 0) && (5.25)\\
&= \mathbb{P}(H \le {}^{k}/_{G},\ G \ge 0) + \mathbb{P}(H \ge {}^{k}/_{G}, G \le 0) && (5.26)\\
&= \int_0^\infty f_G(g)\int_{-\infty}^{k/g} f_H(h)dh\;dg + \int_{-\infty}^0 f_G(g)\int_{k/g}^\infty f_H(h)dh\;dg && (5.27)
\end{aligned}$$

The PDF $f_K(k)$ can then be obtained by differentiating the CDF with respect to k using the chain rule. Where, K_{b-1} is the modified Bessel function of the second kind, and $\Gamma(b)$ is the gamma function.

$$\begin{aligned}
f_K(k) &= \int_{-\infty}^\infty \frac{1}{|g|} f_G(g)\, f_H({}^{k}/_{g})\;dg && (5.28)\\
&= \int_0^\infty -\frac{1}{|g|}\frac{1}{\Gamma(b)\,\theta^b} g^{b-1} e^{-g/\theta}\;\; a e^{-ak/g} dg && (5.29)\\
&= \frac{2a\,(k\theta a)^{\frac{b-1}{2}}\,K_{b-1}\left(2\sqrt{\frac{ka}{\theta}}\right)}{\Gamma(b)\,\theta^b} && (5.30)
\end{aligned}$$

The $2/\eta^{th}$ moment of k can then be expressed by the closed-form equation by solving (5.31) knowing that $K = P_{TX}G\ H$. Since we assume that P_{tx} is constant, the integral

can be solved to give (5.32).

$$\mathbb{E}_K\left[K^{2/\eta}\right] = P_{tx}^{2/\eta}\int_0^\infty k^{2/\eta} f_K(k)\,dk \tag{5.31}$$

$$= \left(P_{tx}\frac{\theta}{a}\right)^{2/\eta}\frac{\Gamma(1+2/\eta)\,\Gamma(b+2/\eta)}{\Gamma(b)},\ for 2/\eta < 1 \tag{5.32}$$

$M_K(t) = \mathbb{E}_K\left[e^{-sK}\right]$ is the MGF of K. The MGF can be determined by solving (5.33) using the PDF expression from (5.32).

$$M_K(t) = \mathbb{E}_K\left[e^{-sP_{tx}K}\right] \tag{5.33}$$

$$= \int_0^\infty e^{-skP_{TX}} f_K(k)\,dk \tag{5.34}$$

$$\overset{(a)}{=} \frac{1}{P_{tx}}\int_0^\infty \frac{e^{-su}}{\Gamma(b)\,\theta^b}\ 2a\left(\frac{u\theta a}{P_{tx}}\right)^{\frac{b-1}{2}} K_{b-1}\left(2\sqrt{\frac{ua}{P_{tx}\theta}}\right)\,du \tag{5.35}$$

$$= \frac{ae^{\frac{a}{\theta s\ P_{tx}}}}{P_{tx}\theta s}\int_1^\infty \frac{1}{t^b} e^{\frac{-a}{\theta s\ P_{tx}}t} dt \tag{5.36}$$

$$\overset{(b)}{=} \frac{ae^{\frac{a}{\theta s\ P_{tx}}}}{P_{tx}\theta s}\int_0^1 \frac{w^{-2}}{w^{-b}} e^{\frac{-a}{w\theta s\ P_{tx}}}\,dw \tag{5.37}$$

$$= \frac{ae^{\frac{a}{P_{tx}\theta s}}}{P_{tx}\theta s}\left(\frac{P_{tx}\theta s}{a}\right)^{1-b}\Gamma\left(1-b, \frac{a}{P_{tx}\theta s}\right) \tag{5.38}$$

Step (a) follows from a change of variables as $u = kP_{tx}$. To determine the closed-form expression of the exponential integral in (5.36) we perform, in step (b), another change of variables as $w = t^{-1}$ and we obtain in (5.38) the incomplete upper gamma function defined as $\Gamma(a,x) := \int_x^\infty t^{a-1}e^{-t}\,\mathrm{d}t$. The expectation $\mathbb{E}_K\left[K^{2/\eta}\Gamma(1-2/\eta, sK)\right]$ can be determined using the law of the unconscious statistician [68] as in (5.40).

$$\mathbb{E}_k\left[K^{2/\eta}\Gamma(1-2/\eta, sK)\right] = \int_0^\infty k^{2/\eta}\Gamma(1-2/\eta, sk)\ \ f_K(k)\,dk \tag{5.39}$$

$$= \csc(\pi b)\left[\left(e^{\frac{a}{\theta s}}\right)\left(-\frac{a}{\theta s}\right)^{b+2/\eta} - n\Gamma(b+2/\eta) + n\Gamma\left(b+2/\eta, -\frac{a}{\theta s}\right)\right.$$

$$\left. + a(-1)^b\left(-\frac{a}{\theta s}\right)^{2/\eta}\Gamma(b-1)\ {}_2F_2\left[\left\{2, 2/\eta+1\right\}, \{2-b, 2+2/\eta\}, \frac{a}{\theta s}\right]\right] \tag{5.40}$$

where, ${}_2F_2$ is the generalized hypergeometric function defined as ${}_pF_q := \sum_{k=0}^\infty \frac{\prod_{j=1}^p (a_j)_k z^k}{\prod_{j=1}^q (b_j)_k k!}$. □

Just by observing the exposure definition in (5.1), we notice some of the effects the parameters will have on the total exposure. However, we are also interested in estimating

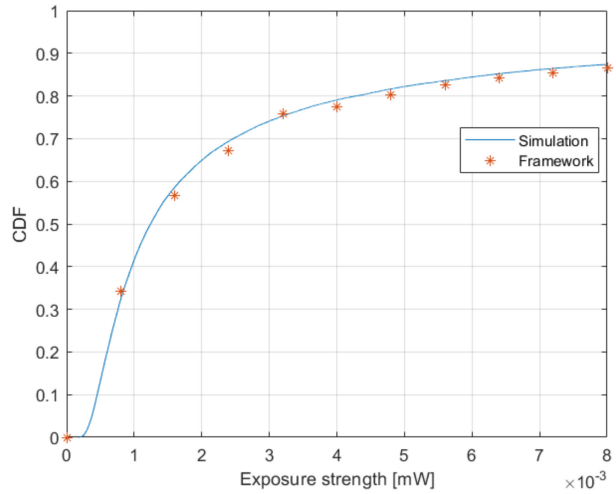

Figure 5.5: Verification of the analytical expression of the CDF of the power received versus a Monte-Carlo simulation.

Parameter	Value
λ	2×10^{-5}
α	0.5
η	4
P_{tx}	$1\,mW$

Table 5.4: Simulation Parameters used for the verification of the analytical equation with Monte-Carlo simulations

the importance of each parameter on the total exposure and analyzing the way these parameters affect the total exposure. In the next section, we first verify our model with a Monte-Carlo simulation, then we investigate the variation of the 90th percentile of the exposure, we perform a sensitivity analysis to quantify the importance of each parameter on the total exposure, and then we compare the model we developed in this chapter with the old model developed in [61].

5.4 Numerical results

In this section, we validate the model against numerical simulations, and we present some numerical results of the variation of the 90th percentile of the exposure against different network parameters. In Figure 5.5, we validate the CDF from with $\varphi(s)$ given by Theorem 1, with Monte-Carlo simulations of the same scenario, to verify the model we developed while the parameters used in the validation are presented in Table 5.4.

The expression derived above has an indeterminate expectation, but from the determined CDF we can easily determine the 90th percentile of the exposure, which is a percentile that is often used to express the exposure in a network. We determine the 90th percentile as function of the base station density for different values of the path loss

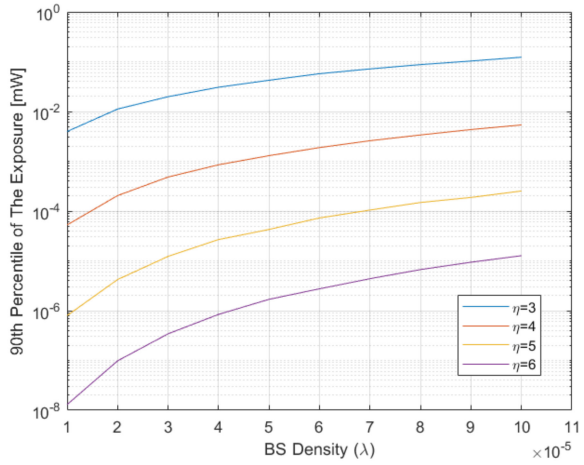

Figure 5.6: 90th percentile of the exposure as function of BS Density λ for different values of the path loss exponent η.

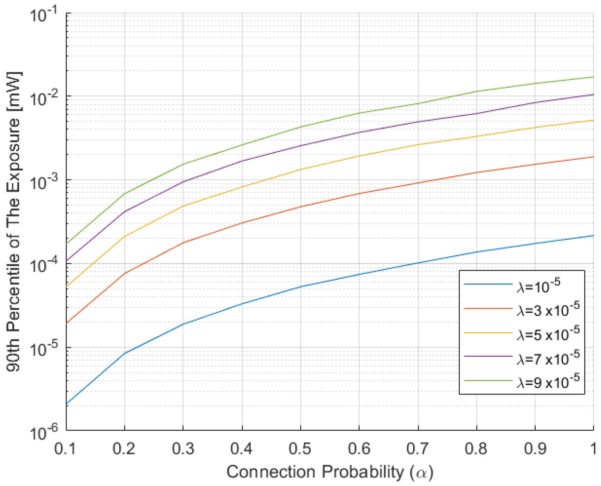

Figure 5.7: 90th percentile of the exposure as function of system utilization α for different values of the BS density λ.

exponent η, the results are presented in Figure 5.6. We also determined the variation of the 90th percentile of the exposure as a function of the system utilization α in Figure 5.7. The parameters used to simulate the results of Figure 5.6 and Figure 5.7 are presented in Table 5.5.

We also perform a comparison between the newly created model and the model in our previous work [61] versus the exposure simulation derived directly from the NYUSIM data in Figure 5.8. This comparison shows that the old model overestimates the exposure especially at the lower percentiles. This overestimation can be attributed to the fact that the old model assumes uniform array pattern, which is equivalent of having an isotropic antenna gain at the transmitter, and gain values towards the MT. It is also apparent, in the model derived in this study compared to the simulations, the small error between the simulation and our model which can be attributed to the error in fitting finite gain data into infinite distributions alongside the errors from the imperfect fitting. The former

Parameter	Value
b	1.45
c	966.5
a	0.57
λ	2×10^{-5}
α	0.5
η	3

Table 5.5: Parameters used in the analysis simulations for Figure 5.6 and Figure 5.7.

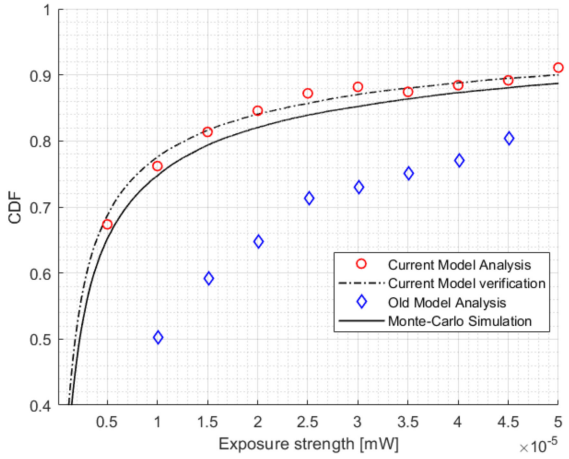

Figure 5.8: Comparison between the current model developed in this chapter (red circles), its verification using Monte-Carlo simulations assuming the gain distributions from Section 5.3 (dashed line), and the model assuming a constant gain presented in 4.2 (blue diamonds), versus a Monte-Carlo simulation of the exposure using gain values simulated by NYUSIM (solid line).

error can be calculated depending on the maximum gain the antenna can produce as in (5.41) where $f_X(x)$ is the probability density function of the fitted distribution, and G_{max} is the maximum gain the antenna array can produce.

$$er_{fit} = \int_{G_{max}}^{\infty} f_X(x)\, dx \tag{5.41}$$

Since massive MIMO will be implemented in really diverse scenarios, it is important to investigate the effect of each variable on the exposure. For this, we perform a variance-based sensitivity analysis on the calculated model which estimates the effect of the variance of the inputs on the variance of the output as form of indices called Sobol indices [69] . Sensitivity analysis is often performed to determine the importance of the input variables on the output of the model. n^{th} degree Sobol indices $S_{1,2...n}$ determine the fraction of the output variance attributed to the set of inputs of degree n. We are interested here in determining the total Sobol indices which can be defined as in (5.42). The total Sobol indices determine the variance of the output due to the variance of an input, in addition to the interactions between the specified input variable and the other

Input Variable	Total Sobol Indices
α	0.447
η	0.932
λ	0.365
P	0.254

Table 5.6: Total Sobol indices of the inputs contributing to the 90th percentile of the exposure in the network.

input variables. It is an alternative to computing the higher-order Sobol indices for every variable.

$$S_{Ti} = \frac{E_{X_{\sim i}}\left(Var_{X_i}\left(Y|\ X_{\sim i}\right)\right)}{Var\left(Y\right)} \tag{5.42}$$

Since obtaining the exposure from the CDF requires solving an inverse function, it takes a long time to determine the Sobol indices and it may introduce inaccuracies at extreme input values. To avoid this, we use polynomial chaos expantion (PCE) using Latin Hypercube samples to estimate a metamodel to represent the 90th percentile of the exposure in the cell. PCE approximates the relation between the model's output to its inputs by expanding it in an orthogonal polynomial basis [69]. The metamodel can be denoted as

$$\Upsilon\left(\zeta\right) = \sum_{\beta \in N^d} a_\beta \Psi_\beta\left(\zeta\right), \tag{5.43}$$

where Ψ_β are miltivariate polynomials defined as the product of univariate polynomials of degrees $(\beta_1, \ldots, \beta_d)$ and a_β are the polynomial's coefficients. The fit model has a leave-one-out error of 0.14%. Using this metamodel we estimate the Sobol indices for each one of the variables and we obtain the results in Table 5.6. We can see that the sum of the total Sobol indices is greater than one, showing the interactions between the input variables in determining the percentile.

5.5 Discussion

In this section, we discuss the results of the numerical outcomes of our model. We discuss the effect of some of the network parameters considered throughout this study on the exposure, and we discuss the result of the sensitivity analysis considering the importance of each parameter on the global exposure. From the results presented in Figure 5.5, we can show the accuracy of the developed model in estimating the total exposure in the cell. The result shows a good overlap between the analytical framework and the numerical validation. Here, the blue solid line is obtained by considering the fitted distribution of the channel and antenna gain, i.e., (5.12) and (5.12). The purpose

of Figure 5.5 is to verify the correctness of the analytical framework. It should be noted that the execution time in obtaining results from the analytical framework is much quicker than the numerical simulations. The sensitivity analysis shows the big effect the path loss exponent has in comparison to the other variables. In terms of exposure, this effect is desirable especially knowing that the path loss exponent is relatively high in mmWave channels leading to lower power in the cell. Although, since cellular networks are usually designed to maintain a sufficient SNR, it would give clearer insight analyzing the exposure in relation with the SNR. On the other hand, our study sheds the light on a usually ignored, but increasingly discussed, aspect of cellular network design and analysis which is the total electromagnetic wave power present in the cell area. As previously mentioned in Section 1.1., the 5G NR architecture make it difficult to accurately measure the exposure because of its beam behavior. In terms of in-situ measurements of the exposure, they are being performed without consideration of the variability in the system utilization in order to have constant beam behavior. This assumption will ignore the effect the system usage will have on the actual exposure in the cell. As we can see from our analysis, the transmission probability, which is directly related to the system utilization, it is the second-most important variable affecting the exposure since it accounts for 0.44 of the total exposure's variance, and simply measuring at constant full transmission may lead to major overestimation of the exposure.

5.6 Conclusion

In this study, we have determined a closed-form analytical representation of the downlink exposure of a 5G massive MIMO network distributed following a PPP with realistic transmission gain and channel representation using statistical distributions instead of approximated value. We have analyzed the distribution of the exposure for different implementation scenarios and we have shown the impact that the network characteristics have on the exposure in the cell. This approach allows the accurate study of the massive MIMO network without the need for costly simulations. We have also shown the significance of using a realistic antenna model as compared to a simple one. We also studied the significance of the key parameters in the network, and we showed the importance the network usage has on the total exposure and the importance of considering it when conducting exposure analysis.

Even though downlink EMF exposure estimation is increasing in importance, most network deployment planning and analysis focuses more on the network performance. And since the goal of future wireless networks is to provide better performing networks, it is of importance to study the EMF exposure jointly with the network performance. Moreover, it is necessary to consider the worst case scenario of the EMF exposure in the network, which is at the nearest MT to the serving BS, which is the focus of the next

chapter.

Chapter 6

Performance and EMF Exposure Analysis of Massive MIMO Networks With Max-Min Power Control in LoS/NLoS Scenarios

Contents

In this chapter, we analyze the EMF exposure, in terms of total received power, in a massive multiple-input multiple-output (MIMO) network at the nearest MT to the serving BS. With the recent deployment of 5G networks, the potential risks of EMF exposure are gaining increasing attention. However, most of the current research that focuses on the mathematical modeling of 5G networks ignore downlink power control. Therefore, we derive the framework of the average power received at the nearest MT under max-min fairness power control using stochastic geometry, where MTs in the cell can be in either LoS and NLoS channel conditions. In addition to that, we derive the expression of the average exposure to SIR ratio at the nearest MT. We propose a tight approximation on the power control coefficient. The framework on total received power and the ratio are then validated by Monte-Carlo simulations. The results show that the average received power monotonically increases as the density of the base station increases and the number of users increases. It is also shown that the system is increasingly efficient in terms of SIR considering the EMF exposure with the increase in the number of antenna elements in the MIMO in NLoS environments, but less so in LoS.

6.1 Introduction

Radio frequency (RF) electromagnetic field (EMF) compliance assessments are critical for manufacturers and operators to prove that the transmitting equipment is compliant with safety regulations on human exposure [51] and to determine exclusion bounds around base stations (BS)s. For this reason, metrics, and measurement procedure, were standardized to ensure proper estimation of the EMF exposure. In the far field, the EMF exposure metric is usually the power density which is directly proportional to the received power [70]. Traditionally, RF EMF exposure assessments are performed assuming the maximum theoretical transmit power at the BS [71]. This will introduce an unnecessary bottleneck when deploying large, high-gain, antenna arrays for 5G networks, also called massive multiple-input multiple-output (MIMO) antennas, which concentrate the transmit power towards the desired MT.

Massive MIMO antennas have become a key technology in 5G systems for both sub-6GHz and millimeter-wave bands [72]. The large number of transmitting elements in one antenna array create a robust transmission channel [73] with high directed gain which results in high throughput, spectral efficiency and energy efficiency at the receiving MT [74]. The large massive MIMO allows the simultaneous transmission to multiple MTs in the cell in the same time-frequency resource block, through spacial multiplexing [75]. Power control schemes exist to ensure coverage for all the MTs in the cell, either by allocating a minimal signal to interference and noise ratio (SINR) targets [76] or ensuring equal SINR between MTs using max-min fairness power control [77]. Massive MIMO has been extensively studied throughout the years with the main focus being the

performance [34], and efficiency. However, the RF EMF exposure cannot be overlooked [78]. Moreover, statistical studies of the EMF exposure have mostly ignored the network performance aspect. Since network planning is done mainly considering the performance, the deployment of future networks should be studied in relation to their induced EMF exposure.

Multiple precoding schemes exist to create signals with high directive gain, with the goal of focusing the transmitted signal towards the served user while simultaneously decreasing the interference [79]. When the MT is in line-of-sight (LoS) with the BS, the precoded signal is sent over a single lobe directed at the MT, however, in non-line-of-sight (NLoS), the precoded signal is sent over several different paths depending on the channel. This spatial variation of the emitted power, while well studied in the domains of coverage and throughput, is introducing new challenges for exposure estimations.

Many papers have addressed modeling the 5G network using stochastic geometry, however, power control was mostly missing since they considered the typical MT. In [80] a millimeter-wave network has been shown to outperform the ultra-high frequency one for a dense 5G network. And in [81], 5G heterogeneous networks were modeled by PPP and K-means clustering methods and their performance analyzed. As for EMF exposure studies of 5G networks, statistical studies were performed to estimate more realistic power levels [26] for simple network architecture. And recently, some studies opted to analyze the average EMF exposure in the cell for randomly distributed BSs following a Poisson point process (PPP) [82], [83].

In this chapter, we aim to characterize the power received and the SIR at the nearest MT to the serving BS in a 5G massive MIMO network in LoS/NLoS scenarios. We consider a more realistic channel model with max-min power control amongst all MTs. Then, a tight approximation of the power control coefficient is proposed and validated by Mon-Carlo simulations in order to obtain closed-form expression on the total received power at MT_0.

The contributions of this chapter can be summarized as follows:

1. We derive a closed-form expression of the average received power for the signal, and the inter-cell and multi-user interference, with max-min fairness power control in LoS/NLoS scenarios.

2. We derive an expression allowing the evaluation of the average ratio between the total power and the SIR in a single cell.

3. We analyze both the average received power and the ratio between it and the SIR for multiple scenarios and show different behaviors in relation to different parameters.

We also propose a robust framework, which has big distinctions from the ones used in exposure studies of massive MIMO networks, that can be considered for future research

on exposure assessment and complicance studies in highly variable networks.

The rest of this chapter is organized as follows. We present the system model in Section II. We derive the expressions for the average total received power and the average ratio between the total power and the SIR in Section III. In Section IV, we apply the models and present the results to analyze the trends of behavior of the power received and SIR. Finally, we give the conclusions and perspective based on the work in Section V.

Vectors and matrices are expressed by boldface lowercase and uppercase letters. $(\cdot)^*$ denotes the complex conjugate of a matrix, and $\|\cdot\|$ is the euclidean norm of a vector. The probability of an event and the expectation are denoted by $\Pr[\cdot]$ and $\mathbb{E}[\cdot]$. The notation $\mathbf{a} \sim \mathcal{CN}(0, I_M)$ represents a circularly symmetric complex Gaussian random vector with zero-mean and a covariance matrix I_M being an $M \times 1$ identity matrix.

6.2 System Model

In this section, we present the system model that we use to evaluate the performance of a massive MIMO network. We focus on some standard modeling assumptions for BS and MT distributions since our aim in this study is to introduce a more relevant scenario of evaluating the exposure in the cell, in addition to performance analysis in this same scenario. Throughout this study, we assume the MRT precoding scheme at the transmitting BS.

6.2.1 Massive MIMO Network Modeling

We consider a downlink multi-cell, multi-user massive MIMO network. This network consists of BSs distributed following a homogeneous PPP $\Phi_{BS} \subset \mathbb{R}^2$ with density λ_{BS}. The MTs are modeled as another homogeneous PPP, Φ_{MT} with density λ_{MT}. We assume the zero-cell to be a disk centered around the BS and having a radius of $R = \frac{1}{\sqrt{\pi\lambda_{BS}}}$, which is the average size of the voronoi cell of a homogeneous PPP. Since Φ_{BS} is stationary and isotropic, the MTs will be distributed inside the cell also following a homogeneous PPP $\Phi^l_{MT} = \left\{X^l_k\right\}$, where X^l_k is the $k+1$-th nearest MT from its serving BS in cell l. We condition Φ_{MT} on having fixed number of points K in a single cell, representing the served MTs in a single time-frequency block. The MTs in a single cell l are therefore distributed following a binomial point process (BPP) [84] Φ^l_{MT} with density $\lambda^l_{MT} = K/R$. We denote by R_{lk} the distance between the k-th MT to the l-th BS, and by R_k the association distance of the k-th MT. Each BS is equipped with M antenna elements and each MT is equipped with a single omnidirectional antenna.

Channel Modeling

In this study, we consider both small-scale fading and uncorrelated path-loss for both LoS and NLoS paths. We assume that the network operates using a time-division duplex (TDD) scheme, to exploit channel reciprocity [85]. Thanks to these assumptions, the BS will be able to estimate the downlink channel matrix using a pilot signal sent from the MT. We assume a cell where each MT can be either LoS or NLoS independently from each-other and independently from the distance to the serving BS, thus we can denote K_L and $K_N = K - K_L$ as two binomial random variables representing the number of MTs in LoS and NLoS conditions to the serving BS, respectively. The probability mass function (PMF) of K_L is that of the binomial distribution $f_{K_L}(x) = \binom{K}{x} p_L^x (1-p_L)^{K-x}$. The LoS and NLoS probabilities are P_L and P_N respectively. We assume that LoS paths can occur exclusively between an MT and its serving BS. We justify this assumption since the inter-cell interference occurs over high distances where the channel is progressively more likely to be in NLoS condition. Same argument applies for denser small cell BSs that are distributed on lower altitudes. We also present distinct path-loss models for both LoS/NLoS channel conditions.

We denote by $\boldsymbol{g}_{lk}^S = \sqrt{\boldsymbol{\beta}_{lk}^S} h_{lk}^S$, for $S \in \{L, N\}$, the $M \times 1$ downlink random channel vector between MT_k and BS_l for a LoS/NLoS link, where β_{lk}^S and h_{lk}^S are the path-loss and small-scale fading vectors respectively. We introduce both vectors in the following.

path-loss

We introduce a two-slope path-loss model that represents LoS/NLoS channel conditions. We express the fading exponents by α_L, with probability p_L and α_N with probability p_N. Furthermore it is important, for modeling the total power received, to consider a two-region path-loss coefficient to avoid the singularity for $R_{lk} = 0$. The path-loss vector is expressed by

$$\boldsymbol{\beta}_{lk}^S(R_{lk}) = \max\left(d, R_{lk}\right)^{-\alpha_S} \tag{6.1}$$

$$= \mathbb{1}_{\Phi_{MT}^{LoS}}(k) \left(d, R_{lk}\right)^{-\alpha_L} + \mathbb{1}_{\Phi_{MT}^{NLoS}}(k) \left(d, R_{lk}\right)^{-\alpha_N} \tag{6.2}$$

where α_S is the path-loss exponent for LoS/NLoS, and $d \in \mathbb{R}^+$ is the distance of the guard zone around the BS.

Small-Scale Fading

For a generic link between MT_k and BS_l we assume that $\boldsymbol{h}_{lk}^S \sim \mathcal{CN}(0, I_M)$ is an $M \times 1$ i.i.d. Rayleigh fading vector representing the small-scale fading of the NLoS link between an MT and a BS.

When transmitting in a LoS massive MIMO channel, the small scale fading is deterministic with very high correlation between the paths between the different antenna elements and the served MT. Therefore, it cannot be expressed as i.i.d. Rayleigh, but its small-scale fading can be represented by a deterministic model. The performance of such case is investigated in [86] and [87] where it is shown that favorable propagation can be obtained for LoS paths, and where a performance analysis is also performed. The $M \times 1$ small-scale fading vector $\boldsymbol{h}_{lk}^{L}$ between BS_l and MT_k in the far-field can be expressed as

$$\boldsymbol{h}_{lk}^{L} \coloneqq e^{i\theta_k} \left(e^{-i\frac{2\pi}{\delta}\Delta_k^{(2)}} \dots e^{-i\frac{2\pi}{\delta}\Delta_k^{(M)}} \right)^T \in \mathbb{C}^M, \tag{6.3}$$

where δ is the carrier wavelength, θ_k is the phase shift between the BS and user k assumed to be uniformly distributed on $[-\pi, \pi]$, and $\Delta_k^{(m)}$ is the distance differential between the mth antenna array element and the kth user as in

$$\Delta_k^{(m)} := d(k,1) - d(k,m), \qquad m = 1, \dots, M \tag{6.4}$$

Assuming that the users are uniformly distributed on the circle of radius R, and the antenna elements spacing between antenna elements is $\frac{\lambda}{2}$, (6.3) can be written as [88]

$$\boldsymbol{h}_{lk}^{L} \coloneqq e^{i\theta_k} \left(e^{-i\pi \sin\psi_k} \dots e^{-i(M-1)\pi \sin\psi_k} \right)^T \in \mathbb{C}^M \tag{6.5}$$

Channel Gain

The channel gain between a BS and an MT in a LoS path depends on the correlation between the channel vector obtained from the uplink pilot and the precoding vector at the BS. The function of this correlation is an intractable function, which is why we propose a simplification of this gain. We divide the space around BS_0 into two angular regions: Main-lobe region where the user is in the main beam of the antenna i.e., the angular separation between MT_k and BS_0 is less than the beamwidth, and side-lobe gain when MT_k is elsewhere. We can easily determine the angular coordinates of the first nulls in the antenna pattern from (6.5) to be $\theta_0 = \pm\sqrt{\frac{3}{M}}$. The gain function can be represented by [89]

$$\mathcal{G}_k(M) = \begin{cases} M, & |\theta_{0,k}| \leq \frac{\sqrt{3}}{\sqrt{M}} \\ G_k(M) = \frac{\sqrt{M} - \frac{\sqrt{3}}{2\pi} M \sin\left(\frac{\sqrt{3}}{2\sqrt{M}}\right)}{\sqrt{M} - \frac{\sqrt{3}}{2\pi} \sin\left(\frac{\sqrt{3}}{2\sqrt{M}}\right)}, & elsewhere \end{cases} \tag{6.6}$$

The signal gain is identical for LoS and NLoS links. However, the interference gain at MT_k will be one of two cases, either aligned interferers when MT_k is in the angular region of the main-lobe or misaligned interference when MT_k is elsewhere. Since the MTs are uniformly distributed in the cell, the probability that a user is aligned with the beam of

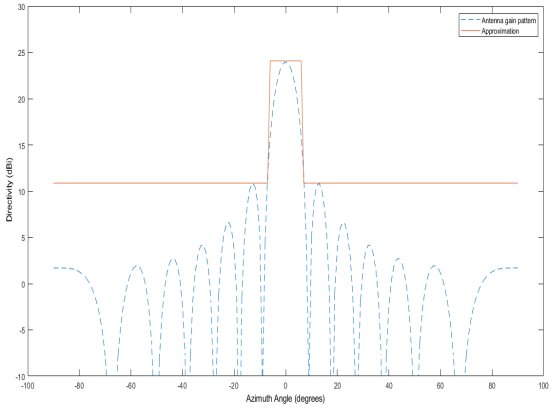

Figure 6.1: Antenna gain pattern and the side-lobe approximation in the LoS link between the BS and the MT

an interferer is $P_A = \frac{1}{\pi}\sqrt{\frac{3}{M}}$. A representation of the antenna pattern and the proposed approximation in (6.6), for $M = 256$, is given in figure 6.1.

6.2.2 Downlink Transmission

In this study, we assume perfect CSI at the transmitter and no pilot contamination. The perfect CSI assumption produces a conservative estimation of the downlink exposure. The signal received at the nearest MT to the typical BS, MT_0 is given by

$$\boldsymbol{y}_0 = \sqrt{\rho_{dl}} \sum_{l \in \Phi_{BS}} \boldsymbol{g}_{l0}^H \boldsymbol{s}_l^S + w_0, \tag{6.7}$$

where ρ_{dl} is the downlink transmit power, $\boldsymbol{g}_{l0}$ is the $M \times 1$ channel gain vector at MT_0 taking into account the path-loss and the small-scale fading, and $\boldsymbol{s}_l$ is the transmitted signal from the BS in cell l. It can be expressed as $\boldsymbol{s}_l = \sum_{k=1}^{K} \sqrt{\eta_{lk}} \boldsymbol{a}_{lk} q_k$, with η_{lk} being the power control coefficient, and $q_k \sim \mathcal{CN}(0,1)$ the transmit data symbols for the kth MT in cell l. Moreover, $\boldsymbol{a}_{lk}$ represents the vector of the linear precoder. Under MRT, the $M \times 1$ precoding vector $\boldsymbol{a}_{lk} = [a_{lk}^1, ..., a_{lk}^M]^T$ is

$$\boldsymbol{a}_{lk}^S = \frac{1}{\mathbb{E}\left[\mathrm{tr}(\mathbf{A}_l \mathbf{A}_l^H)\right]} \boldsymbol{h}_{lk}^H, \tag{6.8}$$

where A_l is the $M \times K$ precoding matrix, the term $\frac{1}{\mathbb{E}\left[\mathrm{tr}(\mathbf{A}_l \mathbf{A}_l^H)\right]} = \frac{1}{\sqrt{M}}$ is the normalization parameter insuring the constraint on the transmit power $\mathbb{E}\left[\rho_{dl} \boldsymbol{s}_l (\boldsymbol{s}_l)^H\right] = \rho_{dl}$.
Taking into account the previous assumptions, the signal received at MT_0 in cell l, is [85]

$$y_0 = \frac{\sqrt{\rho_{dl} \eta_{lk} \beta_{l0}^S}}{\sqrt{M}} \left(\|\boldsymbol{h}_{l0}^S\|^2 + \sum_{l \in \Phi_{BS}} \sum_{k \in \Phi_{MT}^l} \boldsymbol{h}_{l0} \boldsymbol{h}_{lk}^H \right) q_k, \tag{6.9}$$

Table 6.1: List of symbols and abbreviations used in the document

Symbol	Description
Φ_{BS}, λ_{BS}, Φ_{MT}^{l}, λ_{MT}^{l}	Point process and density of the BSs and MTs respectively
R	Radius of the 0-cell
K, K_L, K_N	Number of MTs simultaneously served in a cell, number of served MTs in LoS/NLoS respectively
M	Number of antenna elements at each BS
BS_l, MT_k	BS in cell j and user k in the 0-cell
α_S	Path-loss exponent
d	radius of the guard zone around the BSs
$\boldsymbol{g}_{lk}^{S}$, $\boldsymbol{\beta}_{lk}^{S}$, $\boldsymbol{h}_{lk}^{S}$	$M \times 1$ channel, path-loss, and small scale gain vectors between user k and its associated BS in cell l
η_{lk}	Power control coefficient for MT_{lk}
R_{lk}, R_k	Distance between MT_k and BS_l, and association distance of user k in the 0-cell
$(\cdot)^*, (\cdot)^H, \lvert\cdot\rvert$	Complex conjugate and conjugate transpose of a matrix, respectively
P_A	Aligned probability
$\mathcal{E}_l, \mathcal{E}_{l0}$	Average power received at a the typical MT and nearest MT to BS_l respectively

and the total power received at MT_0 in cell l can be written as

$$\begin{aligned} P_{l0} =& M\rho_{dl}\eta_{l0}\beta_{l0}^{S} + \sum_{i\in\Phi_{BS}\setminus\{l\}} \rho_{dl}\beta_{i0} + \rho_{dl}\beta_{l0}^{S}\times \\ & \left[\sum_{k\in\Phi_{MT}^{NLoS}\setminus\{X_0\}} \eta_{lk} + \sum_{k\in\Phi_{MT}^{LoS}\setminus\{X_0\}} \eta_{lk}\mathcal{G}_k(M)\right], \end{aligned} \tag{6.10}$$

Where the first term in (6.10) represents the received signal, the second term represents the inter-cell interference, and the last term represents the multi-user interference from users in LoS and NLoS. Similarly, the SIR can be written as follows

$$\Xi_0 = \frac{M\eta_{l0}\beta_{l0}^{S}}{\sum\limits_{i\in\Phi_{BS}\setminus\{l\}} \beta_{i0} + \beta_{l0}^{S} \sum\limits_{k\in\Phi_{MT}^{S}\setminus\{X_0\}} \eta_{lk}\mathcal{G}_k(M)}. \tag{6.11}$$

We note from (6.11) that unlike the traditional approach, the SIR at MT_0 decreasing with K is not apparent since β_{l0} is also dependent on K. This will be presented further on when analyzing the expression.

6.2.3 Max-Min Fairness Power Control

Max-min power control seeks to maximize the worst SINR in the cell by providing equal SINR for all the terminals in Φ_{MT}^{l} [85]. The proposed model assumes no coordination between the BSs so that the power control coefficient is computed solely based on the multi-user channel inside the cell, and the coefficient is determined independently in each cell. This results in a simple optimization problem that produces a closed-form solution for this particular scenario. We can write the power control coefficient at the nearest MT to its BS as

$$\eta_{lk} = \frac{1 + \rho_{dl}\beta_{lk}}{\beta_{lk} \sum\limits_{k \in \Phi_{MT}^{S}} \frac{1+\rho_{dl}\beta_{lk}}{\beta_{lk}}}. \tag{6.12}$$

This power control scheme introduces an important trade-off in the power received at MT_0. Even though MT_0 has the smallest path-loss coefficient out of all MTs in the cell, it will have fewer high-gain resources allocated to it, as per (6.10).

We note that the power control coefficient η_{lk} is chosen under the constraint allowing maximum power usage at each BS, i.e. $\mathbb{E}\left[\|s_l\|^2\right] = 1, \forall l$, giving

$$\sum_{k \in \Phi_{MT}^{l}} \eta_{lk} = 1, \forall l. \tag{6.13}$$

6.3 Average Power Received

In this section, we derive the closed-form expressions of the average received power at the nearest MT in cell l, MT_0, using an approximation of the power control coefficient. From this section onward, we ignore the noise factor w_0 in the evaluation of the total power received. And without loss of generality, we assume that the typical BS is located at the origin (Slivnyak theorem [29]). From (6.10), knowing that the precoding gain is independent of the power control coefficient and the path-loss coefficient, and substituting η_{l0} by its expression in (6.12), we divide the expectation of the power received at MT_0 to its associated BS as

$$\mathcal{E}_{l0} = \mathcal{S} + \mathcal{I}_M + \mathcal{I}_I, \tag{6.14}$$

where,

$$\mathcal{S} = \rho_{dl} M \mathbb{E}\left[\eta_{l0}\beta_{l0}\right], \tag{6.15}$$

is the average useful signal power,

$$\mathcal{I}_M = \rho_{dl}\mathbb{E}\left[\beta_{l0}^S \sum_{k\in\Phi_{MT}^S\setminus\{X_0\}} \eta_{lk}\mathcal{G}_k(M)\right], \tag{6.16}$$

is the average multi-user interference power, and

$$\mathcal{I}_I = \mathbb{E}\left[\sum_{i\in\Phi_{BS}\setminus\{l\}} \beta_{l0}\right], \tag{6.17}$$

is the average inter-cell interference power. The sum in the denominator of the power control coefficient (6.12) makes the derivation of the expectations intractable. For this reason, we propose an approximation for this parameter in the following proposition.

Proposition 1. *For an MT k in cell l, the power control coefficient η_{lk} can be approximated, for large number of served users K, using the weak law of large numbers [90] as in*

$$\eta_{lk} = \frac{1+\rho_{dl}\beta_{lk}}{\beta_{lk}\left(\rho_{dl}K + \sum\limits_{j\in\Phi_{MT}^L}(\beta_{lj}^L)^{-1} + \sum\limits_{j\in\Phi_{MT}^N}(\beta_{lj}^N)^{-1}\right)} \tag{6.18}$$

$$\asymp \frac{1+\rho_{dl}\beta_{lk}}{\beta_{lk}\left(\rho_{dl}K + K_L\mathbb{E}\left[(\beta_{lj}^L)^{-1}\right] + K_N\mathbb{E}\left[(\beta_{lj}^N)^{-1}\right]\right)} \tag{6.19}$$

$$= \frac{1+\rho_{dl}\beta_{lk}}{\beta_{lk}\left(\rho_{dl}K + K_L\bar{\Upsilon}(\alpha_L) + K_N\bar{\Upsilon}(\alpha_N)\right)} \tag{6.20}$$

where $\bar{\Upsilon}(\alpha_S)$ is the expectation of the inverse of the path-loss coefficient from a typical MT in the cell for $S \in \{L, N\}$. We validate this proposition for our model with a Monte-Carlo simulation in Fig. 6.2. For minimal error, we assume $K > 10$ throughout this chapter.

We present the expression of the expectation of the path-loss for MTs for either LoS or NLoS, $\bar{\Upsilon}(\alpha_S)$, in the following lemma.

Lemma 2. *The average of the inverse of the path-loss coefficient from a typical MT, $\bar{\Upsilon}(\alpha_S)$, can be formulated as follows,*

$$\bar{\Upsilon}(\alpha_S) = \frac{\alpha d^{\alpha_S+2} + 2R^{\alpha_S+2}}{(\alpha_S+2)R^2} \tag{6.21}$$

Proof. We denote by $F_{R_k}(x) = P(k \in B_d)$ the CDF R_k which is the probability that the

user k falls inside the ball $B_d = \{b(0,x) : x \leq R\}$. Its PDF can be determined as follows

$$f_{R_k}(x) = \frac{\mathrm{d}\Pr\left[k \in b(0,x)\right]}{\mathrm{d}x} = \frac{2x}{R^2}. \tag{6.22}$$

Using the path loss model in (6.2) the nth moment of the distance between the origin and a point distributed according to a BPP in a ball $b(0,R)$ centered at the origin is

$$\mathbb{E}\left[R_k^n\right] = \int_d^R x^n f_{R_k}(x)\,\mathrm{d}x + \int_0^d d^n f_{R_k}(x)\,\mathrm{d}x \tag{6.23}$$

$$= \frac{n\,d^{n+2} + 2R^{n+2}}{(n+2)\,R^2}, \tag{6.24}$$

replacing n with α_S completes the proof. □

From proposition 1, the power control coefficients of the interfering users can be assumed independent of the path-loss of the corresponding user so that their expectations can be determined separately. We determine the expectation of the signal power received at MT_0 in the following theorem.

Theorem 3. *The expectation of the useful signal power received at MT_0 can be expressed as follows*

$$\mathcal{S} = M\rho_{dl}\left(1 + \rho_{dl}p_L\mathcal{Q}_{l0}^L + \rho_{dl}p_N\mathcal{Q}_{l0}^N\right)\mathcal{L}, \tag{6.25}$$

where $\mathcal{Q}_{l0}^S$ is the expectation of the path-loss fading from the multi-user interference at MT_0, determined in the following lemma, and $\mathcal{L} \triangleq \mathbb{E}_{K_L}\left[\frac{1}{K\rho_{dl}+K_L\bar{\Upsilon}(\alpha_L)+K_N\bar{\Upsilon}(\alpha_N)}\right]$ is the expectation of the denominator of the power control coefficient.

Proof. Since the LoS probability of MT_0 is independent of the distance, we can simply write from (6.15)

$$\mathcal{S} = \rho_{dl}M\mathbb{E}\left[\eta_{l0}\beta_{l0}^S\right] \tag{6.26}$$

$$= \rho_{dl}M\mathbb{E}\left[\frac{1+\rho_{dl}\beta_{l0}^S}{\left(\rho_{dl}K + K_L\bar{\Upsilon}(\alpha_L) + K_N\bar{\Upsilon}(\alpha_N)\right)}\right] \tag{6.27}$$

$$= \rho_{dl}M\,\mathbb{E}_{K_L}\left[\frac{1+\rho_{dl}\mathbb{E}_{S,R_{lk}}\left[\beta_{l0}^S\right]}{\left(\rho_{dl}K + K_L\bar{\Upsilon}(\alpha_L) + K_N\bar{\Upsilon}(\alpha_N)\right)}\right] \tag{6.28}$$

$$= \rho_{dl}M\,\mathbb{E}_{K_L}\left[\frac{1+\rho_{dl}\mathbb{E}_{R_{lk}}\left[p_L\beta_{l0}^L + p_N\beta_{l0}^N\right]}{\left(\rho_{dl}K + K_L\bar{\Upsilon}(\alpha_L) + K_N\bar{\Upsilon}(\alpha_N)\right)}\right], \tag{6.29}$$

defining $\mathcal{Q}_{l0}^S \triangleq \mathbb{E}_{R_lk}\left[\beta_{l0}^S\right]$ and $\mathcal{L} \triangleq \mathbb{E}_{K_L}\left[\frac{1}{K\rho_{dl}+K_L\bar{\Upsilon}(\alpha_L)+K_N\bar{\Upsilon}(\alpha_N)}\right]$ and substituting them in the equation gives (6.25) and concludes the proof. □

Lemma 4. *The expectation of the path-loss fading for the nearest MT to its serving BS, $\mathcal{Q}_{l0}$ with path loss model defined in* (6.2) *is*

$$\mathcal{Q}_{l0}^{S} = \frac{d^{-\alpha_S-1}}{4K^2-1}\left(\left(1-\frac{d^2}{R^2}\right)^{K}\left(d^2(2K-1)+R^2\right) - R^2\,{}_2F_1\left(-\frac{1}{2},1-K;\frac{1}{2};\frac{d^2}{R^2}\right)\right) + \frac{\Gamma\left(\frac{-\alpha_S+3}{2}\right)}{2R^2}\left(\frac{\Gamma(K)R^{-\alpha_S+3}}{\Gamma\left(K+\frac{-\alpha_S+3}{2}\right)} - d^{-\alpha_S+3}\,{}_2\tilde{F}_1\left(1-K,\frac{-\alpha_S+3}{2};\frac{-\alpha_S+5}{2};\frac{d^2}{R^2}\right)\right), \tag{6.30}$$

where $\Gamma(x)$ is the gamma function, $B(a,b)$ is the binomial function, and ${}_2\tilde{F}_1$ is the regularized hypergeometric function.

Proof. In a point process consisting of K uniformly distributed points in a 2-dimensional ball of radius R centered at the origin, we denote by $\bar{F}_{R_{l0}}$ the complementary cumulative distribution function (CCDF) of R_{l0} for $0 < r \leq R$ which is the probability that there are less than n points in $b(0,r)$. It can be written as [84]

$$\bar{F}_{R_k}(r) = \sum_{k=0}^{k-1}\binom{K}{1}p\,(1-p)^{K-1}, \tag{6.31}$$

where $p = r^2/R^2$. $\bar{F}_{r_0}$ can also be represented by the regularized incomplete beta function [91].

$$\bar{F}_{R_{l0}}(r) = I_{1-p}(K,1), \tag{6.32}$$

The Euclidean distance R_{l0} from the origin to the nearest neighbor follows a generalized beta distribution of the first kind, the PDF can then be derived by differentiating the CDF w.r.t. r as follows

$$f_{R_{l0}}(r) = -d\bar{F}_{r_0}(r)/dr \tag{6.33}$$

$$= \frac{dp}{dr}\frac{(1-p)^{K-1}}{B(K,1)} \tag{6.34}$$

$$= \frac{B(3/2,K)}{B(K,1)}\beta\left(\left(\frac{r}{2}\right)^2;3/2,K\right), \tag{6.35}$$

where $\beta(x;a,b) = (1/B(a,b))x^{a-1}(1-x)^{b-1}$ is the generalized beta function. The nth moment of R_{lk}, $\mathbb{E}\left[R_{lk}^n\right]$ for $d < r_k < R$ can then be determined as

$$\mathbb{E}\left[R_{l0}^n\right] = \frac{2}{R^3B(K,1)}\int_d^R r^{n+2}\left(1-\left(\frac{r}{R}\right)^2\right)^{K-1}\mathrm{d}r \tag{6.36}$$

$$= \frac{\Gamma\left(\frac{n+3}{2}\right)}{2R^2}\left(\frac{\Gamma(K)R^{n+3}}{\Gamma\left(K+\frac{n+3}{2}\right)} - d^{n+3}\,{}_2\tilde{F}_1\left(1-K,\frac{n+3}{2};\frac{n+5}{2};\frac{d^2}{R^2}\right)\right), \tag{6.37}$$

for $0 < r_k < d$, $\mathbb{E}[\beta_k]$ can be determined likewise by replacing r^n with d^n inside the integral. The summation of the expression in the two ranges gives (6.30) for $n = -\alpha_S$, and completes the proof. □

We now determine the expectation of the multi-user interference at MT_0 defined in (6.16). This expression takes into account the different states an interfering MT can be in, in terms of LoS/NloS, which produces different gains for the interfering signal at MT_0. The derivation of the expectation is presented in the following lemma.

Theorem 5. *The expectation of the multi-user interference at MT_0 is*

$$\begin{aligned}\mathcal{I}_M = \rho_{dl}\left(p_L\mathcal{Q}_{l0}^L + p_N\mathcal{Q}_{l0}^N\right)\frac{(1-p_L)^K}{K(\rho_{dl}+\bar{\Upsilon}(\alpha_N))} \\ \times\ {}_2F_1\left(-K, \frac{K(\rho_{dl}+\bar{\Upsilon}(\alpha_N))}{\bar{\Upsilon}(\alpha_L)-\bar{\Upsilon}(\alpha_N)}; \frac{K\rho_{dl}+\bar{\Upsilon}(\alpha_L)+(K-1)\bar{\Upsilon}(\alpha_N)}{\bar{\Upsilon}(\alpha_L)-\bar{\Upsilon}(\alpha_N)}; \frac{p_L}{p_L-1}\right)\end{aligned} \tag{6.38}$$

Proof. Knowing that β_{l0} and η_{lk} are independent for $k \neq 0$, and the array gain is independent of the distance, we can write

$$\mathcal{I}_M = \rho_{dl}\mathbb{E}_{K_L}\left[\mathcal{Q}_{l0}^S \sum_{k\in\Phi_{MT}^S\setminus\{X_0\}} \mathbb{E}\left[\eta_{lk}^{S'}\mathcal{G}_k(M)\right]\right] \tag{6.39}$$

We determine the expectation of the multi-user interference at MT_0 conditioned on being in LoS by splitting the sum of the interference power to LoS interferers and NLoS interferers as follows

$$\mathcal{I}_M^{LoS} = \rho_{dl}\mathbb{E}_{S,K_L}\left[\mathcal{Q}_{l0}^S\left(\sum_{k\in\Phi_{MT}^L\setminus\{X_0\}}\mathbb{E}\left[\eta_{lk}^L\mathcal{G}_k(M)\right] + \sum_{k\in\Phi_{MT}^N}\mathbb{E}\left[\eta_{lk}^N\right]\right)\,\middle|\, S'=L\right] \tag{6.40}$$

$$= \rho_{dl}\mathbb{E}_{S,K_L}\left[\mathcal{Q}_{l0}^S\left((K_L-1)\mathbb{E}\left[\eta_{lk}^L\mathcal{G}_k(M)\right] + K_N\mathbb{E}\left[\eta_{lk}^N\right]\right)\,\middle|\, S'=L\right], \tag{6.41}$$

since we have a finite number of MTs, the number of interfering MTs in LoS and NLoS are not independent. Then uncoditioning from the LoS probability of MT_0, we determine $\mathcal{I}_M$ as

$$\mathcal{I}_M = \rho_{dl}\mathbb{E}_S\left[\mathcal{I}_M^{LoS}\right] \tag{6.42}$$

$$= \rho_{dl}\left(p_L\mathcal{Q}_{l0}^L + p_N\mathcal{Q}_{l0}^N\right)\mathbb{E}_{K_L}\left[\left((K_L-1)\mathbb{E}\left[\eta_{lk}^L\mathcal{G}_k(M)\right] + K_N\mathbb{E}\left[\eta_{lk}^N\right]\right)\right] \tag{6.43}$$

Moreover, the interference gain from LoS MTs, $\mathcal{G}_k(M)$, is independent of the distance and the number of LoS MTs. Thus, we can get its expectation independently from η_{lk}^L as

follows

$$(6.43) = \rho_{dl}\left(p_L\mathcal{Q}_{l0}^{L} + p_N\mathcal{Q}_{l0}^{N}\right)\left(\left(p_AM + p_{NA}G_k(M)\right)\mathbb{E}_{K_L}\left[(K_L-1)\mathbb{E}_{R_{lk}}\left[\eta_{lk}^{L}\right]\right] + \mathbb{E}_{K_L}\left[K_N\mathbb{E}_{R_{lk}}\left[\eta_{lk}^{N}\right]\right]\right) \tag{6.44}$$

We can express the expectation of the power control coefficient of interfering MTs in either LoS or NLoS as follows

$$\mathbb{E}_{R_{lk}}\left[\eta_{lk}^{S}\right] = \frac{\mathbb{E}_{R_{lk}}\left[(\beta_{lk}^{S})^{-1}\right] + \rho_{dl}}{K\rho_{dl} + K_L\bar{\Upsilon}(\alpha_L) + K_N\bar{\Upsilon}(\alpha_N)}, \tag{6.45}$$

substituting this expression in (6.44) we get the following

$$\begin{aligned}(6.44) = \left(p_L\mathcal{Q}_{l0}^{L} + p_N\mathcal{Q}_{l0}^{N}\right)\Bigg(&\left(p_AM + p_{NA}G_k(M)\right)\mathbb{E}_{K_L}\left[(K_L-1)\frac{\bar{\Upsilon}(\alpha_L)+\rho_{dl}}{K\rho_{dl}+K_L\bar{\Upsilon}(\alpha_L)+K_N\bar{\Upsilon}(\alpha_N)}\right]\\ &+\mathbb{E}_{K_L}\left[K_N\frac{\bar{\Upsilon}(\alpha_N)+\rho_{dl}}{K\rho_{dl}+K_L\bar{\Upsilon}(\alpha_L)+K_N\bar{\Upsilon}(\alpha_N)}\right]\Bigg)\end{aligned} \tag{6.46}$$

$$\begin{aligned}&= \rho_{dl}\left(p_L\mathcal{Q}_{l0}^{L} + p_N\mathcal{Q}_{l0}^{N}\right)\Bigg(\left(p_AM + p_{NA}G_k(M)\right)\left(\bar{\Upsilon}(\alpha_L)+\rho_{dl}\right)\\ &\times\left(\mathbb{E}_{K_L}\left[\frac{K_L}{K\rho_{dl}+K_L\bar{\Upsilon}(\alpha_L)+K_N\bar{\Upsilon}(\alpha_N)}\right] - \mathbb{E}_{K_L}\left[\frac{1}{K\rho_{dl}+K_L\bar{\Upsilon}(\alpha_L)+K_N\bar{\Upsilon}(\alpha_N)}\right]\right)\\ &+\left(\bar{\Upsilon}(\alpha_N)+\rho_{dl}\right)\left(\mathbb{E}_{K_L}\left[\frac{K}{K\rho_{dl}+K_L\bar{\Upsilon}(\alpha_L)+K_N\bar{\Upsilon}(\alpha_N)}\right]\right.\\ &\left.-\mathbb{E}_{K_L}\left[\frac{K_L}{K\rho_{dl}+K_L\bar{\Upsilon}(\alpha_L)+K_N\bar{\Upsilon}(\alpha_N)}\right]\right)\Bigg)\end{aligned} \tag{6.47}$$

$$\begin{aligned}&= \rho_{dl}\left(p_L\mathcal{Q}_{l0}^{L} + p_N\mathcal{Q}_{l0}^{N}\right)\Bigg(\left(p_AM + p_{NA}G_k(M)\right)\left(\bar{\Upsilon}(\alpha_L)+\rho_{dl}\right)\left(\mathcal{L}^{*}-\mathcal{L}\right)\\ &+\left(\bar{\Upsilon}(\alpha_N)+\rho_{dl}\right)\left(K\mathcal{L}-\mathcal{L}^{*}\right)\Bigg),\end{aligned} \tag{6.48}$$

where we define $\mathcal{L}^{*} \triangleq \mathbb{E}_{K_L}\left[\frac{K_L}{K\rho_{dl}+K_L\bar{\Upsilon}(\alpha_L)+K_N\bar{\Upsilon}(\alpha_N)}\right]$, ending the proof. □

The number of MTs in LoS state can be represented by a binomial random variable $K_L \sim B(K, p_L)$ with probability mass function (PMF), $f_{K_L}(k) = \binom{K}{k}p^k(1-p)^{K-k}$, and the number of NLoS MTs is $K_N = K - K_L$. We determine the expressions of $\mathcal{L}$ and $\mathcal{L}^{*}$ in the following lemma.

Lemma 6. *The expressions of $\mathcal{L}$ defined in theorem 3, $\mathcal{L}^*$ defined in theorem 5, and $\mathcal{L}^{**}$ defined in theorem 8 in the following section below, can be expressed as follows*

$$\mathcal{L} = \frac{(1-p_L)^K}{K(\rho_{dl} + \bar{\Upsilon}(\alpha_N))} \, {}_2F_1\left(-K, \frac{K(\rho_{dl} + \bar{\Upsilon}(\alpha_N))}{\bar{\Upsilon}(\alpha_L) - \bar{\Upsilon}(\alpha_N)}; \frac{K\rho_{dl} + \bar{\Upsilon}(\alpha_L) + (K-1)\bar{\Upsilon}(\alpha_N)}{\bar{\Upsilon}(\alpha_L) - \bar{\Upsilon}(\alpha_N)}; \frac{p_L}{p_L - 1}\right), \tag{6.49}$$

$$\begin{aligned}\mathcal{L}^* = &\frac{Kp_L(1-p_L)^{K-1}}{K\rho + (K-1)\bar{\Upsilon}(\alpha_N) + \bar{\Upsilon}(\alpha_L)} \\ &\times {}_2F_1\left(1-K, \frac{\bar{\Upsilon}(\alpha_L) + (K-1)\bar{\Upsilon}(\alpha_N) + K\rho}{\bar{\Upsilon}(\alpha_L) - \bar{\Upsilon}(\alpha_N)}; \frac{2\bar{\Upsilon}(\alpha_L) + (K-2)\bar{\Upsilon}(\alpha_N) + K\rho}{\bar{\Upsilon}(\alpha_L) - \bar{\Upsilon}(\alpha_N)}; \frac{p_L}{p_L - 1}\right),\end{aligned} \tag{6.50}$$

and

$$\begin{aligned}\mathcal{L}^{**} = &\frac{Kp_L(1-p_L)^{K-1}\Gamma\left(\frac{\Upsilon(\bar{\alpha}_L) + (K-1)\Upsilon(\bar{\alpha}_N) + K\rho}{\Upsilon(\bar{\alpha}_L) - \Upsilon(\bar{\alpha}_N)}\right)}{\Upsilon(\bar{\alpha}_L) - \Upsilon(\bar{\alpha}_N)} \\ &\times {}_3\tilde{F}_2\left(2, 1-K, \frac{\Upsilon(\bar{\alpha}_L) + (K-1)\Upsilon(\bar{\alpha}_N) + K\rho}{\Upsilon(\bar{\alpha}_L) - \Upsilon(\bar{\alpha}_N)}; 1, \frac{2\Upsilon(\bar{\alpha}_L) + (K-2)\Upsilon(\bar{\alpha}_N) + K\rho}{\Upsilon(\bar{\alpha}_L) - \Upsilon(\bar{\alpha}_N)}; \frac{p_L}{p_L - 1}\right).\end{aligned} \tag{6.51}$$

Proof. The number of LoS MTs, K_L, follows a binomial distribution in $\mathfrak{B}$. Following from proposition 1, we can write

$$\mathcal{L} = \mathbb{E}_{K_L}\left[\frac{1}{K\rho_{dl} + K_L\bar{\Upsilon}(\alpha_L) + (K-K_L)\bar{\Upsilon}(\alpha_N)}\right] \tag{6.52}$$

$$\overset{(a)}{=} \sum_{x=0}^{K} \frac{1}{K\rho_{dl} + x\bar{\Upsilon}(\alpha_L) + (K-x)\bar{\Upsilon}(\alpha_N)} \binom{K}{x} p_L^x (1-p_L)^{K-x} \tag{6.53}$$

Where (a) comes from the expectation of a function of a binomial random variable. The sum in this expression has the form of a hypergeometric function defined as ${}_2F_1(a,b;c;z) = \sum_{n=0}^{\infty} \frac{z^n (a)_n (b)_n}{n!(c)_n}$, where $(x)_n \equiv \frac{\Gamma(x+n)}{\Gamma(x)}$ is the Pochhammer symbol. Similarly for $\mathcal{L}^*$ and $\mathcal{L}^{**}$,

$$\mathcal{L}^* = \sum_{x=0}^{K} \frac{x}{K\rho_{dl} + x\bar{\Upsilon}(\alpha_L) + (K-x)\bar{\Upsilon}(\alpha_N)} \binom{K}{x} p_L^x (1-p_L)^{K-x}, \tag{6.54}$$

and

$$\mathcal{L}^{**} = \sum_{x=0}^{K} \frac{x^2}{K\rho_{dl} + x\bar{\Upsilon}(\alpha_L) + (K-x)\bar{\Upsilon}(\alpha_N)} \binom{K}{x} p_L^x (1-p_L)^{K-x}. \tag{6.55}$$

Substituting the equations accordingly gives (6.49) and (6.50) concluding the proof. □

Theorem 7. *We present the expression of the expected value of the inter-cell interference*

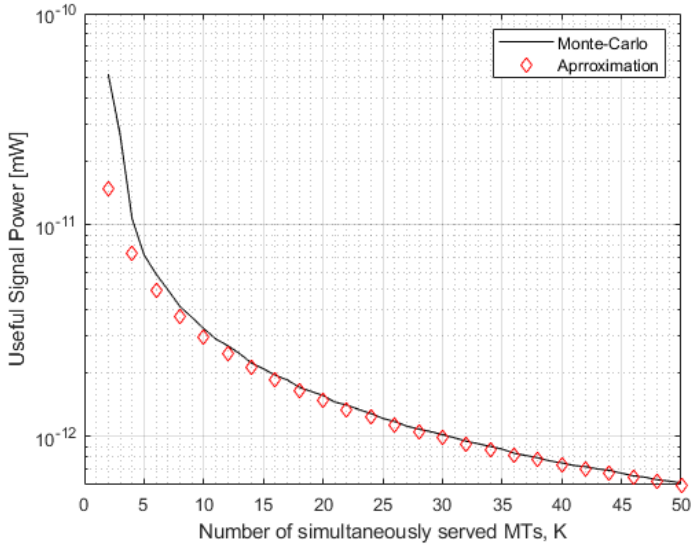

Figure 6.2: Verification of the power control coefficient by comparison between the a Monte-Carlo simulation of the useful signal power and the proposed asymptotic approximation in 6.25

at the nearest MT to BS_l, MT_0, as follows

$$\mathcal{I}_I = 2\pi\lambda_{BS}\rho_{dl}\left(\frac{d^{2-\alpha_N}}{2} + \frac{d^{2-\alpha_N}}{\alpha_N - 2}\right) - \left(p_L\mathcal{Q}_{l0}^L + p_N\mathcal{Q}_{l0}^N\right) \tag{6.56}$$

Proof. This expression can be simply determined by applying Campbell's theorem for sums over stationary PPP [92] as follows

$$\mathcal{I}_I = \rho_{dl}\mathbb{E}\left[\sum_{i\in\Phi_{BS}\setminus\{l\}} \beta_{i0}\right] \tag{6.57}$$

$$= \rho_{dl}\mathbb{E}\left[\sum_{i\in\Phi_{BS}} \beta_{i0} - \beta_{l0}^S\right] \tag{6.58}$$

$$\overset{\text{PGFL}}{=} 2\pi\rho_{dl}\lambda_{BS}\left(\int_0^d d^{-\alpha_N} r \, \mathrm{d}r + \int_d^\infty r^{1-\alpha_N} \, \mathrm{d}r\right) - \left(p_L\mathcal{Q}_{l0}^L + p_N\mathcal{Q}_{l0}^N\right), \tag{6.59}$$

solving the integrations gives (6.56) and concludes the proof. □

6.4 Exposure to SIR Ratio

Cellular network design is usually optimized to maximize the coverage probability, which is directly related to the received SIR at the MT. The exposure to SIR ratio will give insight on how the exposure varies in a massive MIMO cell when the SIR varies due to changes in different network parameters. We determine the PDF of the ratio between

the total power received and the SIR at MT_0 for either LoS and NLoS networks in the following theorem. In this section, we consider only the multi-user interference in the cell for two reasons; the first being that it has the most contribution to the exposure, and the other being the simplification of the formulation. We define the expectation of the ratio between the total power received and the SIR in the following theorem, and we present its derivation in the rest of this section.

Theorem 8. *The expectation of the ratio of the exposure to SIR at the nearest MT to the serving BS is presented as follows*

$$\begin{aligned}\mathfrak{R}_{l0} = \mathcal{I}_M + \frac{\rho_{dl}}{M}\Bigg(& \left(K\mathcal{L} - \mathcal{L}^*\right)\left(\rho_{dl} + \bar{\Upsilon}(2\alpha_N)\right) + \left(\left(K^2 + K - \mathrm{Var}[K_L]\right)\bar{\Upsilon}(\alpha_N) + \mathcal{L}^{**} - 2K\mathcal{L}^*\right) \\ & + \mathbb{E}\left[G_k(M)^2\right]\left(\left(\mathcal{L}^{**} - \mathcal{L}^*\right)\bar{\Upsilon}(\alpha_L) + \mathcal{L}^*\bar{\Upsilon}(2\alpha_L) + \mathrm{Var}[K_L]\mathcal{L}\bar{\Upsilon}(\alpha_L)\right)\Bigg) \\ & \times \frac{2^{\frac{\alpha+2}{\alpha}}K}{\alpha R^2}\int_0^\infty x\left(\frac{\rho^2x^2+2x}{\sqrt{x\left(\rho^2x+4\right)}} + x\right)\left(\sqrt{x\left(\rho^2x+4\right)} + x\right)^{-\frac{\alpha+2}{\alpha}} \\ & \times \left(1 - \frac{4^{1/\alpha}\left(\sqrt{x\left(\rho^2x+4\right)} + x\right)^{-2/\alpha}}{R^2}\right)^{K-1}\end{aligned} \tag{6.60}$$

where $\mathbb{E}\left[G_k(M)^2\right] = p_A M^2 + p_{NA}G_k(M)$, $\mathrm{Var}[K_L] = Kp_L\left(1-p_L\right)$*) is the variance of the binomial random variable* K_L*, and* $\mathcal{L}^{**} \triangleq \mathbb{E}\left[\frac{K_L^2}{\nu_S(K_L)}\right]$ *previously determined in lemma 6.*

Proof. The proof is provided in the rest of this section below. □

Proposition 2. *We can express the expectation of the ratio* $\mathcal{R}_{l0}$ *as follows*

$$\mathfrak{R}_{l0} = \mathcal{I}_M + \frac{\rho_{dl}}{M}\mathbb{E}\left[\frac{1}{\nu_S\left(K_L\right)}\mathbb{E}\left[\mathfrak{I}(\beta_{lk}^S)^2\middle|K_L\right]\right]\mathbb{E}\left[\frac{\left(\beta_{l0}^S\right)^2}{\rho_{dl}\beta_{l0}^S + 1}\right] \tag{6.61}$$

Proof. We define the ratio of the exposure to SIR at MT_0 as follows

$$\mathcal{R}_{l0} \triangleq I(\beta_{l0}, \beta_{lk}) + \frac{I(\beta_{l0}, \beta_{lk})^2}{S(\beta_{l0})}. \tag{6.62}$$

To simplify this expression, we separate the path-loss coefficient of MT_0, β_{l0}, and that of the interfering MTs, β_{lk} in I by defining the random variable $\mathfrak{I}(\beta_{lk}) = \frac{I(\beta_{l0},\beta_{lk})}{\beta_{l0}}\frac{\nu_S(K_L)}{\rho_{dl}}$, it can be expressed as follows

$$\mathfrak{I}(\beta_{lk}) = \sum_{k\in\Phi_{MT}^S\setminus\{X_0\}}\left(\rho_{dl} + (\beta_{lk}^{S_k})^{-1}\right)\mathcal{G}_k(M). \tag{6.63}$$

$\mathcal{R}_{l0}$ can then be expressed by

$$\mathcal{R}_{l0} = \mathfrak{I}(\beta_{lk})\beta_{l0} + \frac{\rho_{dl}}{M\nu_S\left(K_L\right)}\frac{\left(\mathfrak{I}(\beta_{lk})\beta_{l0}\right)^2}{\rho_{dl}\beta_{l0}+1} \tag{6.64}$$

The expectation of (6.64) between the total power received and the SIR at MT_0 can be written as follows

$$\mathfrak{R}_{l0} = \mathbb{E}\left[\mathfrak{I}(\beta_{lk})\beta_{l0} + \frac{\rho_{dl}}{M\nu_S\left(K_L\right)}\frac{\left(\mathfrak{I}(\beta_{lk})\beta_{l0}\right)^2}{\rho_{dl}\beta_{l0}+1}\right]. \tag{6.65}$$

Since β_{l0} and $\mathfrak{I}$ are independent, and conditioning on the number of MTs in LoS, we can write

$$\mathfrak{R}_{l0} = \mathcal{I}_M + \frac{\rho_{dl}}{M}\mathbb{E}\left[\frac{1}{\nu_S\left(K_L\right)}\mathbb{E}\left[\mathfrak{I}(\beta_{lk}^S)^2\middle|K_L\right]\right]\mathbb{E}\left[\frac{\left(\beta_{l0}^S\right)^2}{\rho_{dl}\beta_{l0}^S+1}\right], \tag{6.66}$$

completing the proof. □

First, we derive the expression of the second expectation in (6.66), $\mathbb{E}\left[\frac{\left(\beta_{l0}^S\right)^2}{\rho_{dl}\beta_{l0}^S+1}\right]$. This can be expressed by integrating its PDF as follows

$$\mathbb{E}\left[\frac{\left(\beta_{l0}^S\right)^2}{\rho_{dl}\beta_{l0}^S+1}\right] = \int_0^\infty x f_{\frac{\left(\beta_{l0}^S\right)^2}{\rho_{dl}\beta_{l0}^S+1}}(x)\,\mathrm{d}x. \tag{6.67}$$

We determine the expression of the PDF of β_{l0} in the following lemma, and the PDF of $\frac{\left(\beta_{l0}^S\right)^2}{\rho_{dl}\beta_{l0}^S+1}$ in the corollary following it.

Lemma 9. *The PDF of the path-loss coefficient at MT_0, $f_{\beta_{l0}}$, can be expressed as follows*

$$f_{\beta_{l0}}(x) = \frac{2Kx^{-\frac{2}{\alpha_S}-1}\left(1-\frac{x^{-2/\alpha_S}}{R^2}\right)^{K-1}}{\alpha_S R^2} \tag{6.68}$$

Proof. We determine the CDF of the path-loss fading from (6.2) at MT_0 as

$$\begin{aligned} F_{\beta_{l0}}(x) &= P\left(\max\left(d, R_{l0}^S\right)^{-\alpha_S} < x\right) && (6.69)\\ &= 1 - P\left(\max\left(d, R_{l0}^S\right) < x^{-1/\alpha_S}\right) && (6.70)\\ &= \bar{F}_{R_{l0}}(x^{-1/\alpha_S}), \quad \forall\, x > d^{-\alpha_S} && (6.71)\\ &= \left(1-\frac{x^{-2/\alpha}}{R^2}\right)^K, \quad \forall\, x > d^{-\alpha_S} && (6.72) \end{aligned}$$

The PDF can then be obtained by differentiating $F_{\beta_{l0}}(x)$ with respect to x giving (6.68) and completing the proof. □

Corollary 9.1. *The PDF of* $Y = \frac{\left(\beta_{l0}^S\right)^2}{\rho_{dl}\beta_{l0}^S+1}$ *in proposition 2 can be expressed as follows*

$$f_Y(x) = \frac{2^{\frac{\alpha+2}{\alpha}}K}{\alpha R^2}\left(\frac{\rho^2x^2+2x}{\sqrt{x\left(\rho^2x+4\right)}}+x\right)\left(\sqrt{x\left(\rho^2x+4\right)}+x\right)^{-\frac{\alpha+2}{\alpha}} \times\left(1-\frac{4^{1/\alpha}\left(\sqrt{x\left(\rho^2x+4\right)}+x\right)^{-2/\alpha}}{R^2}\right)^{K-1} \tag{6.73}$$

Proof. We first determine the CDF of $Y = \frac{\left(\beta_{l0}^S\right)^2}{\rho_{dl}\beta_{l0}^S+1}$ as follows

$$F_Y(x) = \Pr\left[\frac{\left(\beta_{l0}^S\right)^2}{\rho_{dl}\beta_{l0}^S+1} < x\right] \tag{6.74}$$

$$= \Pr\left[\beta_{l0}^S < \frac{\rho_{dl}x+\sqrt{x(4+\rho_{dl}^2x}}{2}\right] \tag{6.75}$$

$$= F_{\beta_{l0}^S}\left(\frac{\rho_{dl}x+\sqrt{x(4+\rho_{dl}^2x}}{2}\right), \tag{6.76}$$

and substituting in (6.68) and differentiating for x completes the proof. □

To determine the expectation of the square of the random sum in the interference part in $\mathfrak{R}_{l0}$, we first present a theorem simplifying the expression below. This theorem

Theorem 10. *Where* N *is a random variable, we can write*

$$\mathbb{E}\left[\left(\sum_{i=1}^{N}X_i\right)^2\right] = \mathbb{E}[X_i]^2\big(\mathbb{E}[N]^2-\mathbb{E}[N]\big)+\mathbb{E}[N]\mathbb{E}\big[X_i^2\big] \tag{6.77}$$

Proof. We define the random variable $Y = \sum_{i=1}^{N}X_i$, so we can then write

$$\mathbb{E}\left[Y^2\right] = \mathrm{Var}[Y]+\mathbb{E}[Y]^2 \tag{6.78}$$

we determine the variance of Y as

$$\mathrm{Var}[Y] = \mathrm{Var}\left[\sum_{i=1}^{N}X_i\right] \tag{6.79}$$

$$\overset{(a)}{=} \mathbb{E}_N\left[\mathrm{Var}\left[\sum_{i=1}^{N}X_i\middle|N\right]\right] \tag{6.80}$$

$$= \mathbb{E}[N]\,\mathrm{Var}[X_i]+\mathrm{Var}[N]\mathbb{E}[X_i] \tag{6.81}$$

$$= \mathbb{E}[N]\big(\mathbb{E}\big[X_i^2\big]-\mathbb{E}[X_i]^2\big)+\mathrm{Var}[N]\mathbb{E}[X_i] \tag{6.82}$$

where (a) follows from conditioning and unconditioning on N and the fact that X_i are iid random variables. We can then write (6.78) as follows

$$\mathbb{E}\left[Y^2\right] = \mathbb{E}[N]\big(\mathbb{E}\left[X_i^2\right] - \mathbb{E}[X_i]^2\big) + \mathrm{Var}[N]\mathbb{E}[X_i] + \mathbb{E}[N]^2\mathbb{E}[X_i]^2, \tag{6.83}$$

and completing the proof. □

Using the result from theorem 10, we can determine a closed-form expression of the first expectation in (6.66) as presented in the following lemma.

Lemma 11. *The expectation of the square of the interference divided by the path-loss coefficient of MT_0 can be expressed as follows*

$$\begin{aligned}\mathbb{E}\left[\mathfrak{I}(\beta_{lk}^S)^2\right] = &\left(\rho_{dl}^2 + 2\rho_{dl}\mathbb{E}\left[\left(\beta_{lk}^N\right)^{-1}\right] + \mathbb{E}\left[\left(\beta_{lk}^N\right)^{-2}\right]\right)K_L + \left(\rho_{dl} + \mathbb{E}\left[\left(\beta_{lk}^N\right)^{-1}\right]\right)\left(K_L^2 - K_L\right) \\ &+ \left(\rho_{dl} + \mathbb{E}\left[\left(\beta_{lk}^N\right)^{-1}\right]\right)\mathrm{Var}[K_N] \\ &+ \mathbb{E}\big[\mathcal{G}_k(M)^2\big]\Bigg(\left(\rho_{dl}^2 + 2\rho_{dl}\mathbb{E}\left[\left(\beta_{lk}^N\right)^{-1}\right] + \mathbb{E}\left[\left(\beta_{lk}^N\right)^{-2}\right]\right)K_L \\ &+ \left(\rho_{dl} + \mathbb{E}\left[\left(\beta_{lk}^N\right)^{-1}\right]\right)\left(K_L^2 - K_L\right) + \left(\rho_{dl} + \mathbb{E}\left[\left(\beta_{lk}^N\right)^{-1}\right]\right)\mathrm{Var}[K_N]\Bigg) \\ &+ 2\,\mathbb{E}\left[\mathcal{G}_k(M)K_L(K - K_L)\right]\mathbb{E}\left[\left(\rho_{dl} + (\beta_{lk}^N)^{-1}\right)\left(\rho_{dl} + (\beta_{lk}^L)^{-1}\right)\middle|K_L\right]\Bigg]\end{aligned} \tag{6.84}$$

Proof. Using the result in theorem 10, we can write

$$\mathbb{E}\left[\mathfrak{I}(\beta_{lk}^S)^2\middle|K_L\right] = \mathbb{E}\left[\left(\sum_{k\in\Phi_{MT}^S\setminus\{X_0\}}\left(\rho_{dl} + (\beta_{lk}^{S_k})^{-1}\right)\mathcal{G}_k(M)\right)^2\middle|K_L\right] \tag{6.85}$$

Separating the MTs in LoS and in NLoS of the BS, the expression becomes

$$(6.85) = \mathbb{E}\left[\left(\sum_{k\in\Phi_{MT}^N\setminus\{X_0\}}\left(\rho_{dl} + (\beta_{lk}^N)^{-1}\right) + \sum_{k\in\Phi_{MT}^L\setminus\{X_0\}}\left(\rho_{dl} + (\beta_{lk}^L)^{-1}\right)\mathcal{G}_k(M)\right)^2\middle|K_L\right], \tag{6.86}$$

and expanding the square of the sum we get

$$= \mathbb{E}\Bigg[\left(\sum_{k \in \Phi^N_{MT} \setminus \{X_0\}} \left(\rho_{dl} + (\beta^N_{lk})^{-1} \right) \right)^2 + \left(\sum_{k \in \Phi^L_{MT} \setminus \{X_0\}} \left(\rho_{dl} + (\beta^L_{lk})^{-1} \right) \mathcal{G}_k(M) \right)^2 + 2 \left(\sum_{k \in \Phi^N_{MT} \setminus \{X_0\}} \left(\rho_{dl} + (\beta^N_{lk})^{-1} \right) \right) \left(\sum_{k \in \Phi^L_{MT} \setminus \{X_0\}} \left(\rho_{dl} + (\beta^L_{lk})^{-1} \right) \mathcal{G}_k(M) \right) \Bigg| K_L \Bigg] \tag{6.87}$$

$$= \mathbb{E}\left[\left(\sum_{k \in \Phi^N_{MT} \setminus \{X_0\}} \left(\rho_{dl} + (\beta^N_{lk})^{-1} \right) \right)^2 \Bigg| K_L \right] + \mathbb{E}\left[\left(\sum_{k \in \Phi^L_{MT} \setminus \{X_0\}} \left(\rho_{dl} + (\beta^L_{lk})^{-1} \right) \mathcal{G}_k(M) \right)^2 \Bigg| K_L \right] + 2\,\mathbb{E}\left[\left(\sum_{k \in \Phi^N_{MT} \setminus \{X_0\}} \left(\rho_{dl} + (\beta^N_{lk})^{-1} \right) \right) \left(\sum_{k \in \Phi^L_{MT} \setminus \{X_0\}} \left(\rho_{dl} + (\beta^L_{lk})^{-1} \right) \mathcal{G}_k(M) \right) \Bigg| K_L \right]. \tag{6.88}$$

And since the conditional sums over the MTs in LoS and NLoS are independent of each other, we can separate the expectation of their products as such

$$= \mathbb{E}\left[\left(\sum_{k \in \Phi^N_{MT} \setminus \{X_0\}} \left(\rho_{dl} + (\beta^N_{lk})^{-1} \right) \right)^2 \Bigg| K_L \right] + \mathbb{E}\left[\left(\sum_{k \in \Phi^L_{MT} \setminus \{X_0\}} \left(\rho_{dl} + (\beta^L_{lk})^{-1} \right) \mathcal{G}_k(M) \right)^2 \Bigg| K_L \right] + 2\,\mathbb{E}\left[\mathcal{G}_k(M) K_L (K - K_L) \right] \mathbb{E}\left[\left(\rho_{dl} + (\beta^N_{lk})^{-1} \right) \left(\rho_{dl} + (\beta^L_{lk})^{-1} \right) \middle| K_L \right] \tag{6.89}$$

$$= \mathbb{E}\left[\left(\sum_{k \in \Phi^N_{MT} \setminus \{X_0\}} \left(\rho_{dl} + (\beta^N_{lk})^{-1} \right) \right)^2 \Bigg| K_L \right] + \mathbb{E}\left[\left(\sum_{k \in \Phi^L_{MT} \setminus \{X_0\}} \left(\rho_{dl} + (\beta^L_{lk})^{-1} \right) \mathcal{G}_k(M) \right)^2 \Bigg| K_L \right] + 2\,\mathbb{E}\left[\mathcal{G}_k(M) K_L (K - K_L) \right] \mathbb{E}\left[\left(\rho_{dl} + (\beta^N_{lk})^{-1} \right) \left(\rho_{dl} + (\beta^L_{lk})^{-1} \right) \middle| K_L \right]. \tag{6.90}$$

Following from theorem 10 we can write

$$\begin{aligned} \mathbb{E}\left[\left(\sum_{k \in \Phi^N_{MT} \setminus \{X_0\}} \left(\rho_{dl} + (\beta^N_{lk})^{-1} \right) \right)^2 \Bigg| K_L \right] &= \mathbb{E}\Big[\left(\rho_{dl} + (\beta^N_{lk})^{-1} \right)^2 \Big] K_N \\ &+ \mathbb{E}\Big[\left(\rho_{dl} + (\beta^N_{lk})^{-1} \right) \Big] \left(K_N^2 - K_N \right) \\ &+ \mathbb{E}\Big[\left(\rho_{dl} + (\beta^N_{lk})^{-1} \right) \Big] \mathrm{Var}[K_N], \end{aligned} \tag{6.91}$$

and similarly

$$\mathbb{E}\left[\left(\sum_{k\in\Phi_{MT}^{L}\setminus\{X_0\}}\left(\rho_{dl}+(\beta_{lk}^{L})^{-1}\right)\mathcal{G}_k(M)\right)^2\middle| K_L\right]=\mathbb{E}\left[\mathcal{G}_k(M)^2\right]\Bigg(\mathbb{E}\left[\left(\rho_{dl}+(\beta_{lk}^{L})^{-1}\right)^2\right]K_L + \mathbb{E}\left[\left(\rho_{dl}+(\beta_{lk}^{L})^{-1}\right)\right]\left(K_L^2-K_L\right) + \mathbb{E}\left[\left(\rho_{dl}+(\beta_{lk}^{L})^{-1}\right)\right]\mathrm{Var}[K_L]\Bigg). \tag{6.92}$$

Substituting in the expressions in (6.90) completes the proof. □

The expression of the ratio can then be represented by an almost closed-form equation by substituting the expressions obtained in corollary 9.1 and lemma 11, and by further averaging for K_L giving the result presented in theorem 8.

6.5 Numerical Results

In this section, we present the numerical results of the proposed frameworks with their validations using Monte-Carlo simulations. We present the results of the average power received first, and then we present those of the exposure per SIR ratio.

6.5.1 Simulation Setup

We verify the analytical framework by comparing it to a Monte-Carlo simulation. This simulation was performed assuming K MTs distributed in a circle centered around the BS of the zero-cell, and the BSs being distributed following a PPP with intensity λ_{BS} with an average of 2000 BS in the network. The received power is the sum of the transmitted powers from all BSs subject to the path loss model previously introduced. The beamforming gains and power control coefficients are modeled as presented in (6.10) and (6.12) respectively. We also assume the proposed approximation of LoS gain where the gain of the interference power from serving non-aligned MTs corresponds to the adjacent beams' gain, which will produce a conservative scenario. The simulation was performed over 10^5 iteration and took around 30 minutes to complete. The parameters used for the simulation are summarized in table 6.2.

6.5.2 Average Power Received

In Fig. 6.3, we plot the average received power as function of the the number of antenna elements, M, for different LoS probabilities and for different number of served MTs. We notice in Fig. 6.3a that the average power received at MT_0 increases with M,

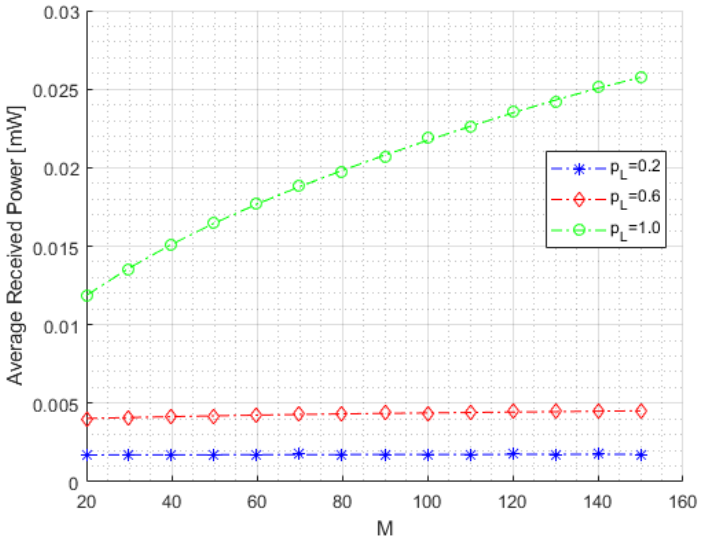

(a)

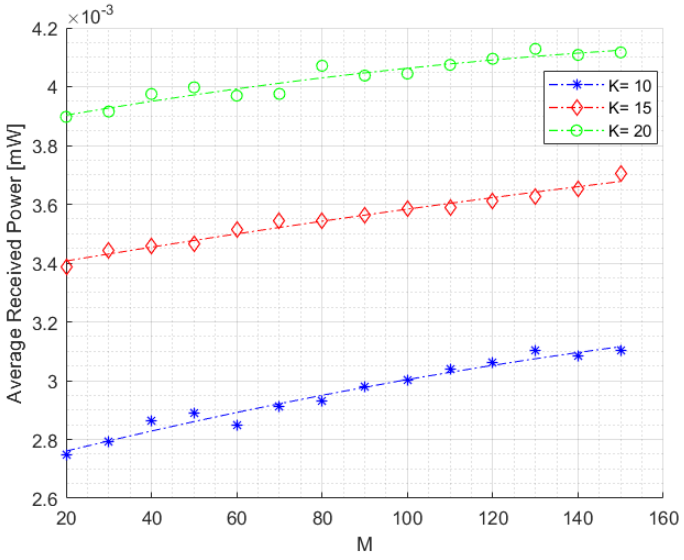

(b)

Figure 6.3: Average power received as function of the number of antenna elements M for different values of (a) p_L for $K = 15$ and (b) K for $M = 256$. Markers represent the Monte-Carlo simulation results and the dotted line represents the result from the analytical framework.

Parameter	Value
λ_{BS}	10^{-4}
K	10
ρ_{dl}	1 mW
M	256
R	$1/\left(\sqrt{2\pi\lambda_{BS}}\right)$
α_L, α_N	3, 4
d	5 m
p_L	0.5
Number of realisations	10^5

Table 6.2: Summary of default parameters used in the Monte-Carlo simulations (unless otherwise stated)

and at a much higher rate the higher p_L is, even though the interference gain is lower for LoS channels, and it is inversely proportionate to the number of antenna elements M. The number of antenna elements affects mainly the gain of the useful signal towards MT_0, and on a smaller scale, the gain of the aligned interference when the interferer is in LoS to the BS and is aligned with MT_0. The small increase with M for lower p_L indicates that the major contributing factor to the exposure at MT_0 with this high number of served MTs, is not the useful signal, but the interference, thus the path-loss exponent contributes more to the exposure than the transmission gain. Similarly, in Fig. 6.3b, we see that the average power received is increasing with M even with. However, it also increases with the density of served MTs the cell λ^0_{MT}, where the average distance of MT_0 to the serving BS is higher, even though the high-gain useful signal power decreases with K increasing.

In Fig. 6.4 we see similar behavior to Fig. 6.3 concerning LoS probability, however for different reasons. Denser networks will increase the possibility of MTs being close to the serving BS. Even though the power control will lower the received signal power at closer distances to keep a uniform SIR throughout the cell, the increased interference power will produce higher power received while degrading the signal quality.

To determine the effect of increasing the number of served MTs in the cell, and thus the number of multi-user interferers, we increase K while maintaining a fixed MT density in the cell without affecting the distance of MT_0 to its BS. We do this simply by changing the BS density λ_{BS}, and thus changing the radius of the cell. The BS density will satisfy $\lambda_{BS}(K) = \frac{K_0}{K}\lambda^0_{BS}$ where K_0 and λ^0_{BS} are the initial number of MTs and the initial BS density producing the MT density to maintain. In Fig. 6.5, we plot the expectation of the total received power as function of the number of antenna elements M under these conditions. We notice, as expected, that increasing the number of served MTs decreases the total received power in both LoS and NLoS, and at similar rate.

Setting $p_L = 0.5$, in Fig. 6.6, we notice that the power received is higher for larger

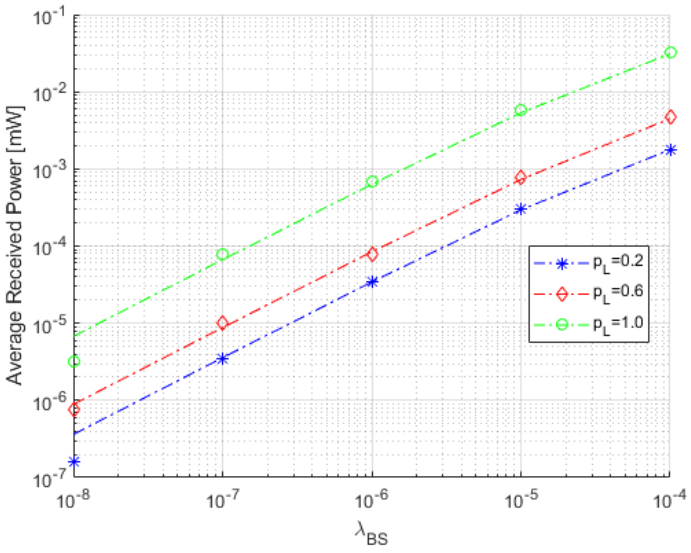

(a)

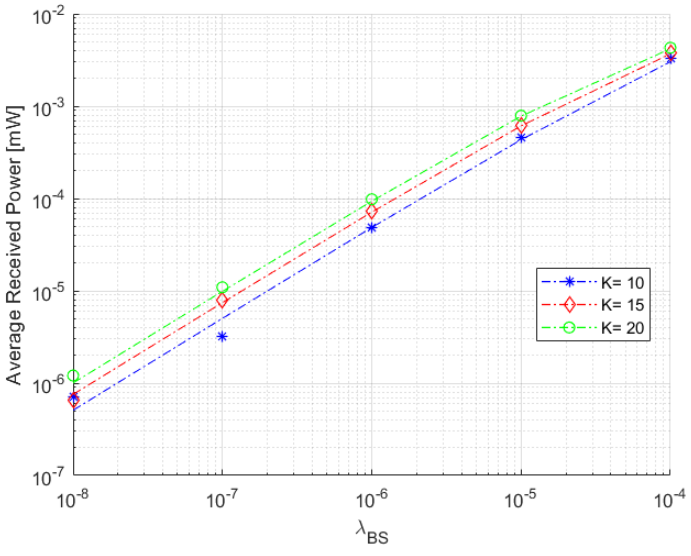

(b)

Figure 6.4: Average power received as function of the BS density for different values of (a) p_L for $K = 15$ and (b) K in LoS. Markers represent the Monte-Carlo simulation results and the dotted line represents the result from the analytical framework.

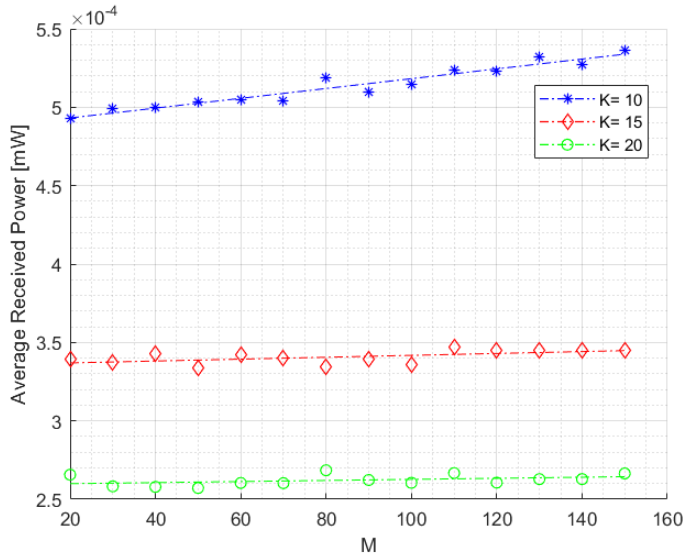

(a)

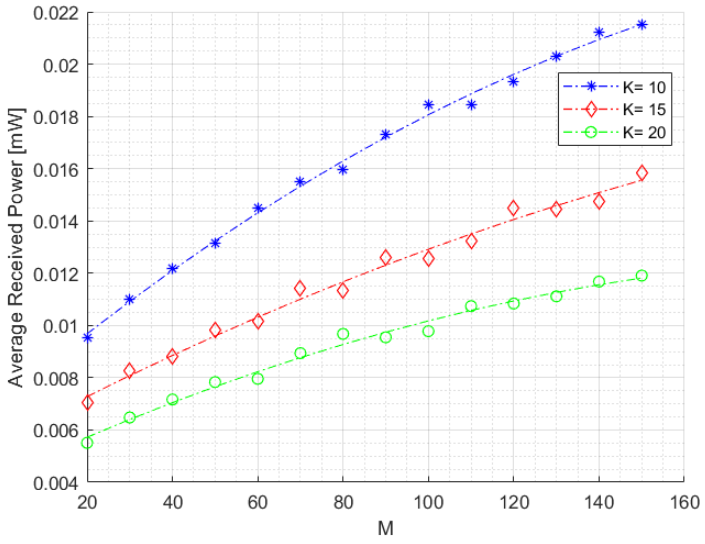

(b)

Figure 6.5: Average power received as function of the number of antenna elements M for different values of K where the MT density in the cell is constant in (a) NLoS and (b) LoS. Markers represent the Monte-Carlo simulation results and the dotted line represents the result from the analytical framework.

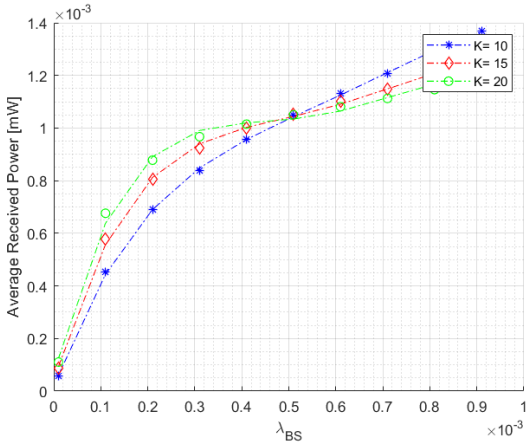

(a)

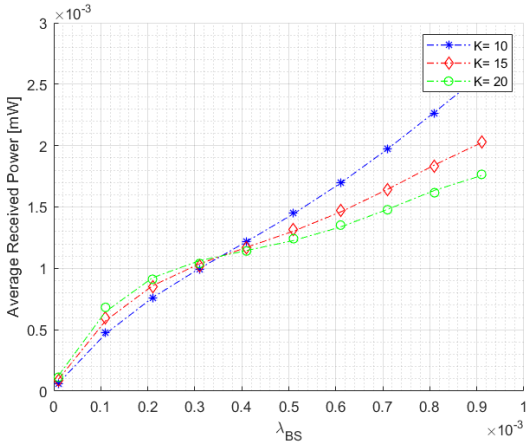

(b)

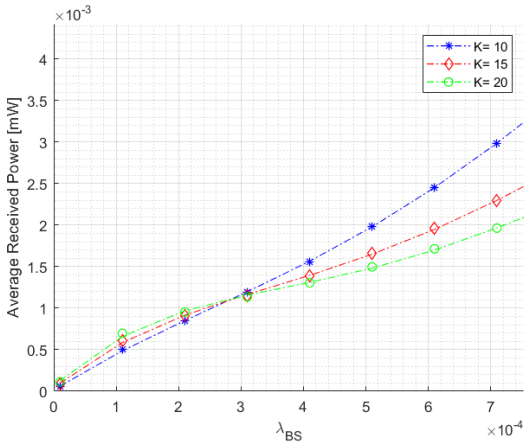

(c)

Figure 6.6: Expectation of the total power received at MT_0 as function of the BS density λ_{BS} and different number of served MTs K, for $M = 16$ (a), $M = 64$ (b), and $M = 128$ (c) antenna array elements. Markers represent the Monte-Carlo simulation results and the dotted line represents the result from the analytical framework.

numbers of served MTs in denser networks. However for sparse networks, this behavior changes and the power received decreases with the number of served MTs. We also notice, from the different sub-figures, that the BS density at which this change occurs depends on the value of M, and thus the beamforming gain. The higher number of antenna elements, the denser the network is when behavior changes.

6.5.3 Exposure to SIR Ratio

In this section we analyze the ratio between the total power received and the SIR at MT_0. This ratio gives insight on how different network parameters and transmission scenarios jointly affects both the EMF exposure and the coverage in the cell. It represents how many milliwatts of total power is received at MT_0 per unit SIR.

In Fig. 6.7, we plot the expectation of the ratio $\mathcal{R}_{l0}$ as function of the transmit power in mW in a LoS (b) and an NLoS (a) environment. The plot in 6.7 shows that the ratio grows linearly with the increase in transmit power and with an equal slope for all values of K. However, the increase in $\mathcal{R}_{l0}$ increases with the increase of K. This is, as explained before, due to the increase in the MT density in the cell, thus lower distance of MT_0. Just like for the average power received, the same behavior can be expected from increasing the BS density λ_{BS} since it will reduce the cell radius R and thus increasing λ_{MT}.

In Fig. 6.8, we evaluate the ratio as function of the antenna elements, M. We notice that the ratio decreases with M, and it decreases further in mostly NLoS environments compared to LoS ones. This decrease indicates that the SIR gained by increasing the number of transmitting elements is larger than the amount of EMF exposure gained.

In Fig. 6.9, we evaluate the ratio at different user load in the cell. We plot the average ratio as function of M for different number of MTs simultaneously served in the cell taking $p_L = 0.5$. As expected, the increasing number of served MTs will degrade the communication quality by increasing the interference as well as increasing the exposure by increasing the MT density λ^0_{MT}. However, the trend of the ratio is monotonically decreasing with M, this is due to an increase in the transmission gain in the useful signal part without an increase in multi-user interference. On the contrary, a large number of antenna elements produces a lower interference gain when the interferers are in LoS of the BS and a lower alignment probability.

Just like in section 6.3, we want to study the scenario where different number of served MTs are being served without increasing λ^0_{MT}. In Fig. 6.10, we plot $\mathfrak{R}_{l0}$ under this condition and we notice that, the ratio keeps decreasing with M in both LoS and NLoS scenarios, unlike in 6.9a where the ratio increases in LoS. However, the expectation of the ratio, same as in Fig. 6.9, always increases with K.

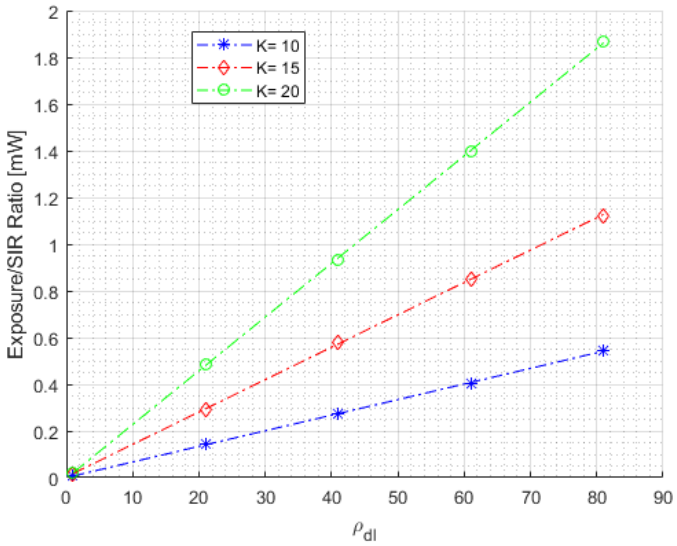

(a)

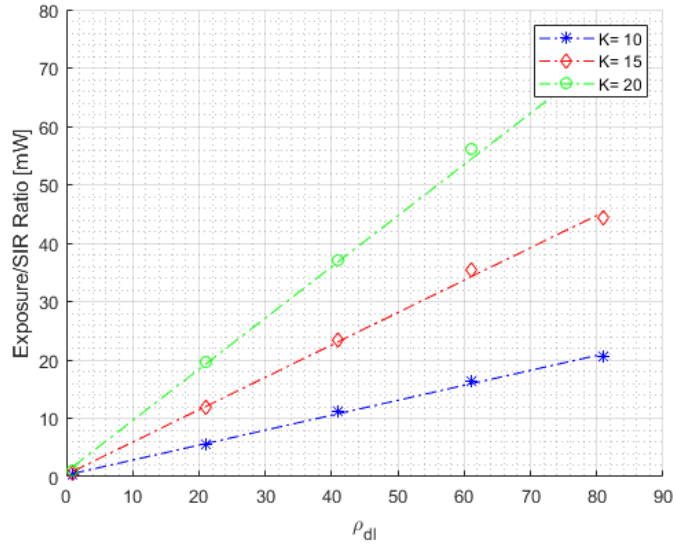

(b)

Figure 6.7: Expectation of the ratio of the exposure to SIR at MT_0 versus the transmit power, ρ_{dl}, for different number of served MTs, K in (a) NLoS and (b) LoS. Markers represent the Monte-Carlo simulation results and the dotted line represents the result from the analytical framework.

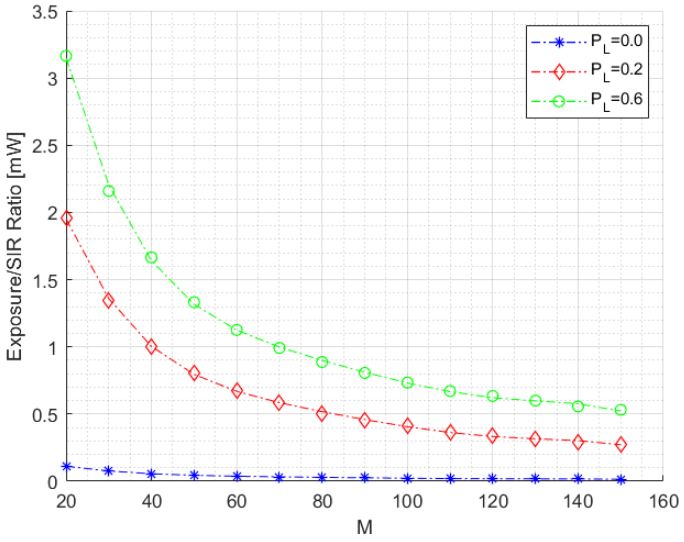

Figure 6.8: Ratio between the total power received and SIR as function of M for different p_L and $K = 15$

6.6 Conclusion

In this chapter, we have we derived the expression of the average power received at nearest MT to its serving BS, MT_0, under max-min fairness power control using stochastic geometry. We also determined the expression of the ratio of the exposure to SIR at MT_0 in a single cell scenario. We determined the closed-form expressions of the useful received signal, the multi-user interference and inter-cell interference. We proposed a tight approximation on the power control coefficient, and based on it, the framework on total received power is then validated by Monte-Carlo simulations.

The results show that the average received power at MT_0 monotonically increases as, the density of the base station, the number of antenna elements, and the MT density increases. The results also show that the more the environment is LoS, the increase of the power received is greater. In addition to that, we show that, for dense environments, the power received for different MT densities changes its trend and higher MT densities will result in lower power received. This change is also dependent on the number of antenna elements M.

As for the ratio of the exposure to SIR, we show that increasing the transmit power at the BSs will result at a higher increase in exposure than in SIR, likewise is seen in a purely LoS environment versus M. On the other hand, in the cases where the environment is not purely LoS, the results show that as M increases, the SIR increases at a higher rate than the exposure, and more so in increasingly NLoS environments. We also show that increasing the number of MTs in the cell, and increasing the number of served MTs without changing the MT density, increases the exposure more than the SIR. This increase is reduced however the higher M is. This shows that antennas with

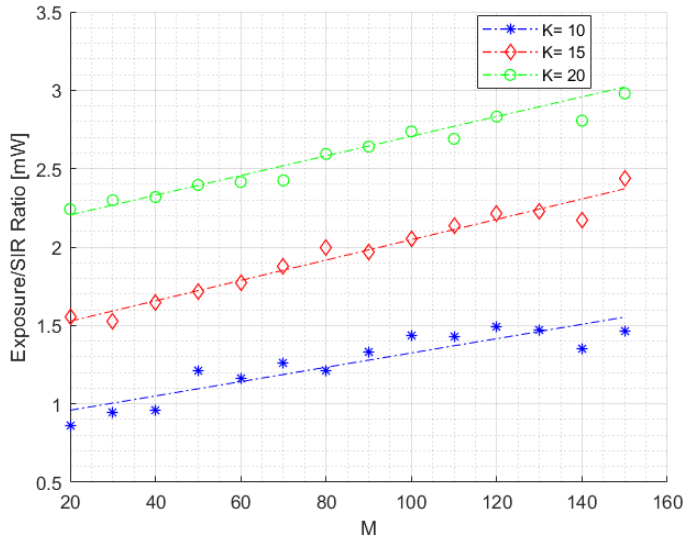

(a)

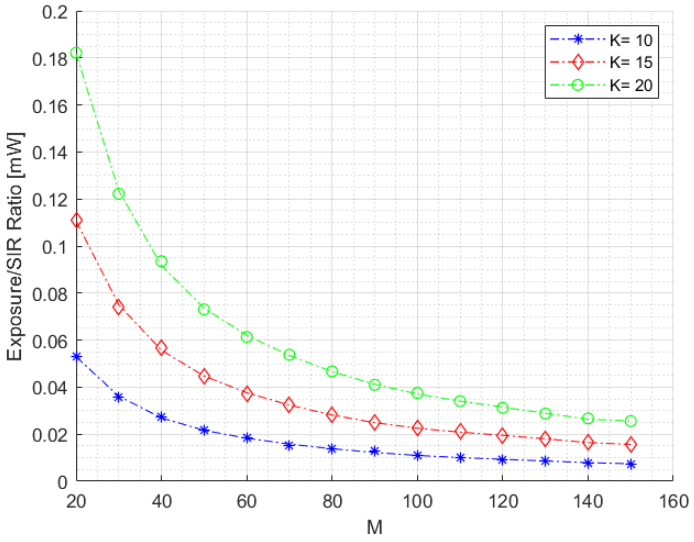

(b)

Figure 6.9: Ratio between the total power received and SIR as function of M for multiple values of K in (a) LoS and (a) NLoS. Markers represent the Monte-Carlo simulation results and the dotted line represents the result from the analytical framework.

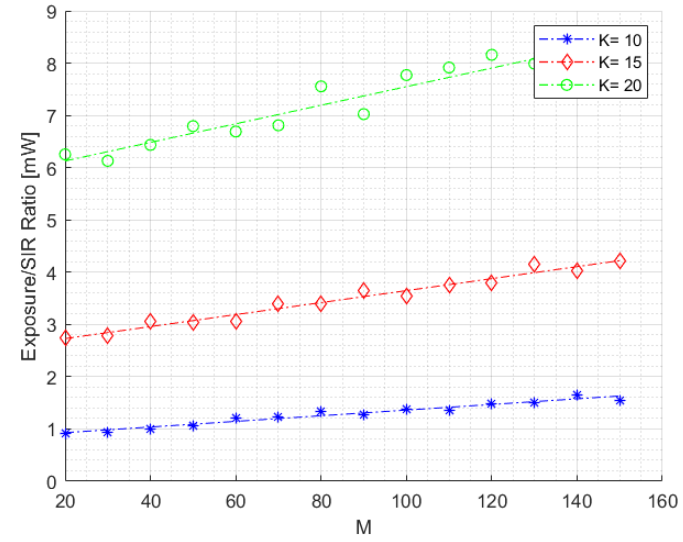

(a)

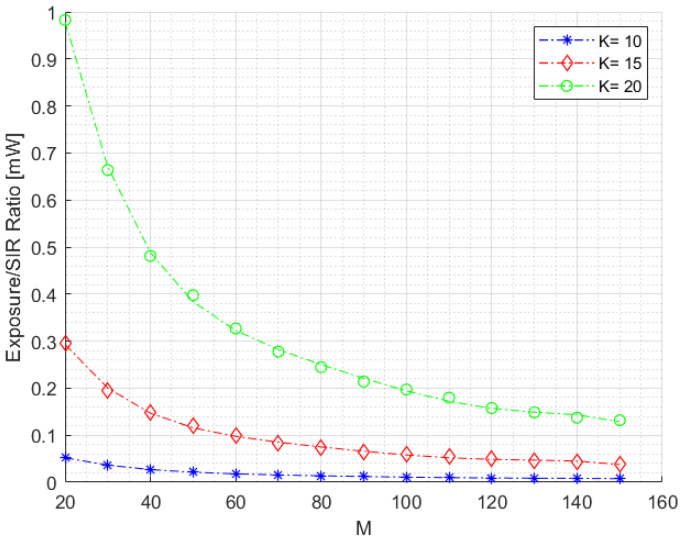

(b)

Figure 6.10: Ratio between the total power received and SIR as function of M for multiple values of K in (b) LoS and (a) NLoS, while maintaining a constant MT density in the cell. Markers represent the Monte-Carlo simulation results and the dotted line represents the result from the analytical framework.

higher antenna elements will be increasingly efficient to the coverage in the 5G network considering the EMF exposure in NLoS environments, however, decreasingly so the more LoS the environment is.

Chapter 7

Conclusions and Future Work

Contents

7.1 Conclusions

In this dissertation, we present the EMF measurement methods applied to 5G massive MIMO networks and we analyze their advantages and disadvantages in relation to the different characteristics of 5G NR. We also present a new methodology for studying the EMF exposure in a wireless network using stochastic geometry, where the different characteristics of the 5G network can be modeled mathematically and studied for different deployment scenarios.

Second, we study the 5G massive MIMO network in mmWave frequency bands. We model the cellular network's BSs as randomly placed points in the 2D space following a stationary PPP and the power is then modeled as shot-noise process. We get the statistical channel and antenna gain distributions from fitting the data obtained from the NYUSIM channel simulator which is itself based on measurements in the mmWave frequency band. These distributions were then integrated into the mathematical framework to obtain a closed-form equation of the MGF of the total received power at the typical MT in the cell. The CDF of this distribution is then analyzed for different scenarios and sensitivity analysis performed to investigate the impact of different network parameters on the total exposure, and it has been shown that the network utilization will have the highest impact on the exposure.

Third, we present a more relevant scenario in studying the EMF exposure in a 5G massive MIMO networks using stochastic geometry which is by considering the nearest MT to its associated BS, MT_0, instead of the typical MT in a MU network wehere many MTs are being served by a single BS in the same time-frequency block. We distribute the BSs following a PPP and the MTs inside a single cell following a BPP. We consider a network deploying max-min fairness power control to distribute the downlink resources fairly between the simultaneously-served MTs ensuring equal SIR throughout the cell. We consider both LoS and NLoS channels and their respective antenna gains. We determine the closed-form equation of the total power received and the expression of the exposure to SIR ratio at MT_0. We analyze the total power received for multiple network parameters and for different LoS probabilities, we also analyze the exposure to SIR ratio. We analyze the results of the power received and we deduce that, in this system, the increase of the SIR, by either network densification or by deployment of larger arrays, is always larger than the increase of the electromagnetic field (EMF) exposure.

7.2 Future work

Many extensions in the field of exposure analysis can be made based on this dissertation for analytical studies of the EMF exposure. We present some of them below.

7.2.1 Non-PPP models

We chose the stationary in this dissertation PPP for its mathematical tractability and its generality. However, many more point processes can be considered to represent different different network architectures. Clustered point processes, e.g. Matérn clustering process (MCP), can be considered to model clusters of small-cell transmitters, access points, or MT distributions. Repulsive point processes, e.g. Matérn hard-core process (MHCP) or β-Ginibre point process, can be considered to model the spatial repulsion that exists between BSs. An interesting research path would be to compare these different deployment scenarios in the context of EMF exposure jointly with the network performance.

7.2.2 Compliance boundary estimation

Compliance boundary can be equated to the exclusion zone considered for the bounded path-loss models used throughout this dissertation. This boundary is essential for constructors to define in order to deploy a certain antenna. Since for 5G systems assuming maximum radiated power in a specific beam is over-conservative and may introduce unnecessary restrictions, statistical limits can be better studied for different scenarios to get more accurate estimations.

7.2.3 Joint optimization of EMF exposure and performance

While the main focus when developing massive MIMO antennas is the spectral and energy efficiency through beamforming techniques, these need to take into consideration the EMF exposure so it doesn't exceed regulatory limits. Optimization problems can be formulated using the developed framework to improve the performance while simultaneously limiting human exposure to EMFs.

Bibliography

[1] S. Sun, G. R. MacCartney, and T. S. A. Rappaport, "Novel millimeter-wave channel simulator and applications for 5g wireless communications," *IEEE Int. Conf. Commun*, pp. 1–7,

[2] G. A. Akpakwu, B. J. Silva, G. P. Hancke, and A. M. Abu-Mahfouz, "A survey on 5g networks for the internet of things: Communication technologies and challenges," *IEEE Access*, vol. 6, pp. 3619–3647, 2018. DOI: 10.1109/ACCESS.2017.2779844.

[3] A. Zaidi, F. Athley, J. Medbo, U. Gustavsson, G. Durisi, and X. Chen, *5G Physical Layer: principles, models and technology components*. Academic Press, 2018.

[4] L. Chiaraviglio, A. Elzanaty, and M.-S. Alouini, "Health risks associated with 5g exposure: A view from the communications engineering perspective," *IEEE Open Journal of the Communications Society*, vol. 2, pp. 2131–2179, 2021.

[5] D. Colombi, P. Joshi, R. Pereira, D. Thomas, D. Shleifman, B. Tootoonchi, B. Xu, and C. Törnevik, "Assessment of actual maximum rf emf exposure from radio base stations with massive mimo antennas," in *2019 PhotonIcs Electromagnetics Research Symposium - Spring (PIERS-Spring)*, 2019, pp. 570–577. DOI: 10.1109/PIERS-Spring46901.2019.9017343.

[6] S. Aerts, L. Verloock, M. Van den Bossche, D. Colombi, L. Martens, C. Törnevik, and W. Joseph, "In-situ measurement methodology for the assessment of 5g nr massive mimo base station exposure at sub-6 ghz frequencies," *IEEE Access*, vol. 7, pp. 184 658–184 667, 2019.

[7] E. Onggosanusi, M. S. Rahman, L. Guo, Y. Kwak, H. Noh, Y. Kim, S. Faxer, M. Harrison, M. Frenne, S. Grant, R. Chen, R. Tamrakar, Gao, and Qiubin, "Modular and High-Resolution Channel State Information and Beam Management for 5G New Radio," *IEEE Communications Magazine*, vol. 56, no. 3, pp. 48–55, Mar. 2018, ISSN: 1558-1896. DOI: 10.1109/MCOM.2018.1700761.

[8] P. von Butovitsch, D. Astely, C. Friberg, A. Furuskär, B. Göransson, B. Hogan, J. Karlsson, and E. Larsson, "Advanced Antenna Systems for 5G Networks," Ericsson, Tech. Rep., Nov. 2018.

[9] J. Wang, Z. Lan, C.-S. Sum, C.-W. Pyo, J. Gao, T. Baykas, A. Rahman, R. Funada, F. Kojima, I. Lakkis, H. Harada, and S. Kato, "Beamforming codebook design and performance evaluation for 60ghz wideband wpans," in *2009 IEEE 70th Vehicular Technology Conference Fall*, 2009, pp. 1–6. DOI: 10.1109/VETECF.2009.5379063.

[10] A. Wiesel, Y. C. Eldar, and S. Shamai, "Zero-forcing precoding and generalized inverses," *IEEE Transactions on Signal Processing*, vol. 56, no. 9, pp. 4409–4418, 2008. DOI: 10.1109/TSP.2008.924638.

[11] T. Lo, "Maximum ratio transmission," *IEEE Transactions on Communications*, vol. 47, no. 10, pp. 1458–1461, 1999. DOI: 10.1109/26.795811.

[12] A. Simonsson, M. Thurfjell, B. Halvarsson, J. Furuskog, S. Wallin, S. Itoh, H. Murai, D. Kurita, K. Tateishi, A. Harada, and Y. Kishiyama, "Beamforming Gain Measured on a 5G Test-Bed," in *2017 IEEE 85th Vehicular Technology Conference (VTC Spring)*, Jun. 2017, pp. 1–5. DOI: 10.1109/VTCSpring.2017.8108648.

[13] B. Halvarsson, K. Larsson, M. Thurfjell, K. Hiltunen, K. Tran, P. Machado, D. Juchnevicius, and H. Asplund, "5G NR Coverage, Performance and Beam Management Demonstrated in an Outdoor Urban Environment at 28 GHz," in *2018 IEEE 5G World Forum (5GWF)*, Jul. 2018, pp. 416–421. DOI: 10.1109/5GWF.2018.8517035.

[14] T. S. Rappaport, S. Sun, R. Mayzus, H. Zhao, Y. Azar, K. Wang, G. N. Wong, J. K. Schulz, M. Samimi, and F. Gutierrez, "Millimeter wave mobile communications for 5g cellular: It will work!" *IEEE Access*, vol. 2013, pp. 335–349, DOI: http://dx.doi.org/10.1109/ACCESS.2013.2260813.

[15] E. Dahlman, S. Parkvall, and J. Sköld, "Chapter 24 - New 5G Radio-Access Technology," in *4G LTE-Advanced Pro and The Road to 5G (Third Edition)*, E. Dahlman, S. Parkvall, and J. Sköld, Eds., Academic Press, Jan. 2016, pp. 547–573, ISBN: 978-0-12-804575-6. DOI: 10.1016/B978-0-12-804575-6.00024-8.

[16] (). "5G — ShareTechnote," [Online]. Available: https://www.sharetechnote.com/html/5G/5G_Phy_BeamManagement.html (visited on 11/15/2021).

[17] 3GPP, "NR; Multi-connectivity; Overall description; Stage-2," 3rd Generation Partnership Project (3GPP), Technical Specification (TS) 37.340, Oct. 2021, Version 15.0.0. [Online]. Available: http://www.3gpp.org/%5C-DynaReport/%5C-38211.htm.

[18] Y. Niu, Y. Li, D. Jin, L. Su, and A. Vasilakos, "A survey of millimeter wave (mmwave) communications for 5g: Opportunities and challenges," *Wireless Networks*, vol. 21, Feb. 2015. DOI: 10.1007/s11276-015-0942-z.

[19] 3GPP, "NR; Physical channels and modulation," 3rd Generation Partnership Project (3GPP), Technical Specification (TS) 38.211, Jan. 2018, Version 15.0.0. [Online]. Available: http://www.3gpp.org/%5C-DynaReport/%5C-38211.htm.

[20] ——, "NR; Physical layer procedures for control," 3rd Generation Partnership Project (3GPP), Technical Specification (TS) 38.213, Jan. 2018, Version 15.0.0. [Online]. Available: http://www.3gpp.org/%5C-DynaReport/%5C-38213.htm.

[21] X. Lin, J. Li, R. Baldemair, J.-F. T. Cheng, S. Parkvall, D. C. Larsson, H. Koorapaty, M. Frenne, S. Falahati, A. Grovlen, and K. Werner, "5G New Radio: Unveiling the Essentials of the Next Generation Wireless Access Technology," *IEEE Communications Standards Magazine*, vol. 3, no. 3, pp. 30–37, Sep. 2019, ISSN: 2471-2833. DOI: 10.1109/MCOMSTD.001.1800036.

[22] A. Ghosh, "5G New Radio (NR) : Physical Layer Overview and Performance," p. 38, 2017.

[23] M. Giordani, M. Polese, A. Roy, D. Castor, and M. Zorzi, "A tutorial on beam management for 3gpp nr at mmwave frequencies," *IEEE Communications Surveys Tutorials*, vol. 21, no. 1, pp. 173–196, 2019. DOI: 10.1109/COMST.2018.2869411.

[24] A. Ahlbom, U. Bergqvist, J. H. Bernhardt, J. P. Cesarini, L. A. Court, M. Grandolfo, M. Hietanen, A. F. McKinlay, M. H. Repacholi, D. H. Sliney, J. a. J. Stolwijk, M. L. Swicord, L. D. Szabo, M. Taki, T. S. Tenforde, H. P. Jammet, and R. Matthes, "Guidelines for limiting exposure to time-varying electric, magnetic, and electromagnetic fields (up to 300 GHz)," *Health Physics*, vol. 74, no. 4, pp. 494–521, 1998, ISSN: 0017-9078. pmid: 9525427. [Online]. Available: https://jhu.pure.elsevier.com/en/publications/guidelines-for-limiting-exposure-to-time-varying-electric-magneti-5 (visited on 10/15/2021).

[25] H. M. Madjar, "Human radio frequency exposure limits: An update of reference levels in europe, usa, canada, china, japan and korea," in *2016 International Symposium on Electromagnetic Compatibility - EMC EUROPE*, 2016, pp. 467–473. DOI: 10.1109/EMCEurope.2016.7739164.

[26] B. Thors, A. Furuskär, D. Colombi, and C. Törnevik, "Time-Averaged Realistic Maximum Power Levels for the Assessment of Radio Frequency Exposure for 5G Radio Base Stations Using Massive MIMO," *IEEE Access*, vol. 5, pp. 19 711–19 719, 2017, ISSN: 2169-3536. DOI: 10.1109/ACCESS.2017.2753459.

[27] 3GPP, "NR; Physical layer procedures for data," 3rd Generation Partnership Project (3GPP), Technical Specification (TS) 38.214, Jan. 2018, Version 15.0.0. [Online]. Available: http://www.3gpp.org/%5C-DynaReport/%5C-38214.htm.

[28] ——, "5G; NR; User Equipment (UE) conformance specification; Radio transmission and reception; Part 1: Range 1 standalone," 3rd Generation Partnership Project (3GPP), Technical Specification (TS) 38.512-1, Dec. 2020, Version 16.5.0. [Online]. Available: http://www.3gpp.org/%5C-DynaReport/%5C-38214.htm.

[29] M. Haenggi, *Stochastic Geometry for Wireless Networks*. Cambridge: Cambridge University Press, 2012, ISBN: 978-1-139-04381-6. DOI: 10.1017/CBO9781139043816. [Online]. Available: http://ebooks.cambridge.org/ref/id/CBO9781139043816 (visited on 04/20/2021).

[30] T. Bai and R. W. Heath, "Analyzing uplink sinr and rate in massive mimo systems using stochastic geometry," *IEEE Transactions on Communications*, vol. 64, no. 11, pp. 4592–4606, 2016. DOI: 10.1109/TCOMM.2016.2591007.

[31] P. Parida and H. S. Dhillon, "Stochastic geometry-based uplink analysis of massive mimo systems with fractional pilot reuse," *IEEE Transactions on Wireless Communications*, vol. 18, no. 3, pp. 1651–1668, 2019. DOI: 10.1109/TWC.2019.2895061.

[32] N. Akbar, E. Björnson, N. Yang, and E. G. Larsson, "Max-Min Power Control in Downlink Massive MIMO with Distributed Antenna Arrays," *IEEE Transactions on Communications*, pp. 1–1, 2020, ISSN: 1558-0857. DOI: 10.1109/TCOMM.2020.3033018.

[33] Z. Chen and E. Björnson, "Channel Hardening and Favorable Propagation in Cell-Free Massive MIMO With Stochastic Geometry," *IEEE Transactions on Communications*, vol. 66, no. 11, pp. 5205–5219, Nov. 2018, ISSN: 1558-0857. DOI: 10.1109/TCOMM.2018.2846272.

[34] A. Papazafeiropoulos, P. Kourtessis, M. D. Renzo, S. Chatzinotas, and J. M. Senior, "Performance Analysis of Cell-Free Massive MIMO Systems: A Stochastic Geometry Approach," *IEEE Transactions on Vehicular Technology*, vol. 69, no. 4, pp. 3523–3537, Apr. 2020, ISSN: 1939-9359. DOI: 10.1109/TVT.2020.2970018.

[35] S. Kusaladharma, W. P. Zhu, W. Ajib, and G. Amarasuriya, "Achievable rate analysis of noma in cell-free massive mimo: A stochastic geometry approach," in *ICC 2019 - 2019 IEEE International Conference on Communications (ICC)*, 2019, pp. 1–6. DOI: 10.1109/ICC.2019.8761506.

[36] A. Papazafeiropoulos, H. Q. Ngo, P. Kourtessis, S. Chatzinotas, and J. M. Senior, "Optimal energy efficiency in cell-free massive mimo systems: A stochastic geometry approach," in *2020 IEEE 31st Annual International Symposium on Personal, Indoor and Mobile Radio Communications*, 2020, pp. 1–7. DOI: 10.1109/PIMRC48278.2020.9217353.

[37] T. Maksymyuk, M. Brych, and V. Pelishok, "Stochastic geometry models for 5g heterogeneous mobile networks," *The Smart Computing Review*, pp. 89–101, Apr. 2015. DOI: 10.6029/smartcr.2015.02.002.

[38] P. Madhusudhanan, J. G. Restrepo, Y. Liu, and T. X. Brown, "Analysis of downlink connectivity models in a heterogeneous cellular network via stochastic geometry," *IEEE Transactions on Wireless Communications*, vol. 15, no. 6, pp. 3895–3907, 2016. DOI: 10.1109/TWC.2016.2530723.

[39] J. G. Andrews, F. Baccelli, and R. K. Ganti, "A tractable approach to coverage and rate in cellular networks," *IEEE Transactions on Communications*, vol. 59, no. 11, pp. 3122–3134, 2011. DOI: 10.1109/TCOMM.2011.100411.100541.

[40] J. S. Gomez, A. Vasseur, A. Vergne, P. Martins, L. Decreusefond, and W. Chen, "A case study on regularity in cellular network deployment," *IEEE Wireless Communications Letters*, vol. 4, no. 4, pp. 421–424, 2015. DOI: 10.1109/LWC.2015.2431263.

[41] M. Di Renzo, S. Wang, and X. Xi, "Inhomogeneous double thinning—modeling and analysis of cellular networks by using inhomogeneous poisson point processes," *IEEE Transactions on Wireless Communications*, vol. 17, no. 8, pp. 5162–5182, 2018. DOI: 10.1109/TWC.2018.2838597.

[42] B. Sklar, "Rayleigh fading channels in mobile digital communication systems .i. characterization," *IEEE Communications Magazine*, vol. 35, no. 7, pp. 90–100, 1997. DOI: 10.1109/35.601747.

[43] Ö. Özdogan, E. Björnson, and E. G. Larsson, "Massive mimo with spatially correlated rician fading channels," *IEEE Transactions on Communications*, vol. 67, no. 5, pp. 3234–3250, 2019. DOI: 10.1109/TCOMM.2019.2893221.

[44] I. S. Gradshteĭn, I. M. Ryzhik, and A. Jeffrey, *Table of Integrals, Series, and Products*, 7th ed. Amsterdam ; Boston: Academic Press, 2007, 1171 pp., ISBN: 978-0-12-373637-6.

[45] J. GIL-PELAEZ, "Note on the inversion theorem," *Biometrika*, vol. 38, no. 3-4, pp. 481–482, Dec. 1951, ISSN: 0006-3444. DOI: 10.1093/biomet/38.3-4.481. eprint: https://academic.oup.com/biomet/article-pdf/38/3-4/481/718851/38-3-4-481.pdf. [Online]. Available: https://doi.org/10.1093/biomet/38.3-4.481.

[46] T. Nitsche, C. Cordeiro, A. B. Flores, E. W. Knightly, E. Perahia, and I. N. P. I. 8. Aper, "Directional 60 ghz communication for multi-gigabit-per-second wi-fi," *IEEE Commun. Mag*, pp. 132–141, DOI: http://dx.doi.org/10.1109/MCOM.2014.6979964.

[47] T. S. Rappaport, Y. Xing, G. R. MacCartney, A. F. Molisch, E. Mellios, and J. Zhang, "Overview of millimeter wave communications for fifth-generation (5g) wireless networks—with a focus on propagation models," *IEEE Trans. Antennas Propag*, pp. 6213–6230, DOI: http://dx.doi.org/10.1109/TAP.2017.2734243.

[48] I. Commission, "On non-ionizing radiation protection (icnirp)," *Guidelines for Limiting Exposure to Time-Varying Electric, Magnetic and Electromagnetic Fields (*, pp. 483–524, DOI: http://dx.doi.org/10.1097/HP.0000000000001210.

[49] I. Standard, "For safety levels with respect to human exposure to electric, magnetic, and electromagnetic fields, 0 hz to 300 ghz," *In*, vol. 95, no. 1-2019, pp. 1–312, 2019. DOI: http://dx.doi.org/10.1109/IEEESTD.2019.8859679.

[50] B. Thors, A. Furuskar, D. Colombi, and C. Tornevik, "Time-averaged realistic maximum power levels for the assessment of radio frequency exposure for 5g radio base stations using massive mimo," *IEEE Access*, pp. 19 711–19 719, DOI: http://dx.doi.org/10.1109/ACCESS.2017.2753459.

[51] P. Baracca, A. Weber, T. Wild, and C. Grangeat, "A statistical approach for rf exposure compliance boundary assessment in massive mimo systems," in *WSA 2018; 22nd International ITG Workshop on Smart Antennas*, 2018, pp. 1–6.

[52] S. Azzi, Y. Huang, B. Sudret, and J. Wiart, "Surrogate modeling of stochastic functions-application to computational electromagnetic dosimetry," *Int. J. Uncertain. Quantif*, pp. 351–363, DOI: http://dx.doi.org/10.1615/Int.J.UncertaintyQuantification.2019029103.

[53] S. Aerts, L. Verloock, M. V. D. Bossche, D. Colombi, L. Martens, C. Tornevik, and W. Joseph, "In-situ measurement methodology for the assessment of 5g nr massive mimo base station exposure at sub-6 ghz frequencies," *IEEE Access*, pp. 84 658–18 466, DOI: http://dx.doi.org/10.1109/ACCESS.2019.2961225.

[54] C.-X. Wang, J. Bian, J. Sun, W. Zhang, and M. A. Zhang, "Survey of 5g channel measurements and models," *IEEE Commun. Surv. Tutorials*, pp. 3142–3168, DOI: http://dx.doi.org/10.1109/COMST.2018.2862141.

[55] 3GPP, "Study on Channel Model for Frequencies from 0.5 to 100 GHz," 3rd Generation Partnership Project (3GPP), Technical Report (TR) 38.901, Oct. 2017, Version 14.0.0.

[56] ——, "Study of Radio Frequency (RF) and Electromagnetic Compatibility (EMC) Requirements for Active Antenna Array System (AAS) Base Station," 3rd Generation Partnership Project (3GPP), Technical Report (TR) 37.840, 2014.

[57] T. S. Rappaport, S. Sun, and M. Shafi, "Investigation and comparison of 3gpp and nyusim channel models for 5g wireless communications," in *2017 IEEE 86th Vehicular Technology Conference (VTC-Fall)*, 2017, pp. 1–5. DOI: 10.1109/VTCFall.2017.8287877.

[58] J. Ko, Y. Cho, S. Hur, T. Kim, J. Park, A. F. Molisch, K. Haneda, M. Peter, D. Park, and D. Cho, "Millimeter-wave channel measurements and analysis for statistical spatial channel model in in-building and urban environments at 28 ghz," *IEEE Trans. Wirel. Commun*, vol. 2017, pp. 5853–5868, DOI: http://dx.doi.org/10.1109/TWC.2017.2716924.

[59] J. Huang, C. Wang, R. Feng, J. Sun, W. Zhang, and Y. Yang, "Multi-frequency mmwave massive mimo channel measurements and characterization for 5g wireless communication systems," *IEEE J. Sel. Areas Commun*, pp. 1591–1605, DOI: http://dx.doi.org/10.1109/JSAC.2017.2699381.

[60] X. Zhao, S. Li, Q. Wang, M. Wang, S. Sun, W. C. M. Hong, and S. a. Modeling, "And validation at 32 ghz in outdoor microcells for 5g radio systems," *IEEE Access*, pp. 1062–1072, DOI: http://dx.doi.org/10.1109/ACCESS.2017.2650261.

[61] A. Hajj, M. Wang, S. D. Doncker, P. Oestges, C. Wiart, and J. A, "Statistical estimation of 5g massive mimo's exposure using stochastic geometry," *In Proceedings of the*, vol. 2020, pp. 1–3, Aug. 2020. DOI: http://dx.doi.org/10.23919/URSIGASS49373.2020.9232290.

[62] 3GPP, "Study of Radio Frequency (RF) and Electromagnetic Compatibility (EMC) Requirements for Active Antenna Array System (AAS) Base Station," 3rd Generation Partnership Project (3GPP), Technical Specification (TS) 37.840, Dec. 2020, Version 15.0.0. [Online]. Available: https://www.etsi.org/deliver/etsi%5C_ts/138200%5C_138299/138214/15.02.00%5C_60/ts%5C_138214v150200p.pdf.

[63] J. Venkataraman, M. Haenggi, and O. Collins, "Shot noise models for outage and throughput analyses in wireless ad hoc networks," in *Proceedings of the Military Communications Conference (MILCOM), , DC, USA, pp. 1–7*, 2006, pp. 23–25.

[64] E. Onggosanusi, S. Rahman, L. Guo, Y. Kwak, H. Noh, Y. Kim, S. Faxer, M. Harrison, M. Frenne, S. Grant, *et al.*, "Modular and high-resolution channel state information and beam management for 5g new radio," *IEEE Commun. Mag*, pp. 48–55, DOI: http://dx.doi.org/10.1109/MCOM.2018.1700761.

[65] R. Lenner, G. J. Schilero, M. L. Padilla, and A. S. A. Teirstein, "Survey on hybrid beamforming techniques in 5g: Architecture and system model perspectives," *Sarcoidosis Vasc. Diffus. Lung Dis*, pp. 143–147,

[66] J. Gil-Pelaez, "Note on the inversion theorem," *Biometrika*, DOI: http://dx.doi.org/10.1093/biomet/38.3-4.481.

[67] E. W. I. G. F. Weisstein, *MathWorld—A Wolfram Web Resource*. Available online. [Online]. Available: https://mathworld.wolfram.com/IncompleteGammaFunction.html.

[68] B. Ringn, "The law of the unconscious statistician. 2009," *p*, pp. 1–3, [Online]. Available: http://www.maths.lth.se/matstat/staff/bengtr/mathprob/unconscious.pdf.

[69] S. Azzi, B. Sudret, and J. Wiart, "Sensitivity analysis for stochastic simulators using differential entropy," *Int. J. Uncertain. Quantif*, vol. 2020, pp. 25–33, DOI: http://dx.doi.org/10.1615/Int.J.UncertaintyQuantification.2020031610.

[70] R. Vallauri, G. Bertin, B. Piovano, and P. Gianola, "Electromagnetic field zones around an antenna for human exposure assessment: Evaluation of the human exposure to emfs.," *IEEE Antennas and Propagation Magazine*, vol. 57, no. 5, pp. 53–63, 2015. DOI: 10.1109/MAP.2015.2474127.

[71] IEC 62232:2017, "Determination of rf field strength, power density and sar in the vicinity of radiocommunication base stations for the purpose of evaluating human exposure," International Electrotechnical Commission, Standard, Oct. 2017.

[72] E. Björnson, E. G. Larsson, and T. L. Marzetta, "Massive MIMO: Ten Myths and One Critical Question," en, *IEEE Communications Magazine*, vol. 54, no. 2, pp. 114–123, Feb. 2016, ISSN: 0163-6804, 1558-1896. DOI: 10.1109/MCOM.2016.7402270. arXiv: 1503.06854.

[73] Z. Chen and E. Björnson, "Channel hardening and favorable propagation in cell-free massive mimo with stochastic geometry," *IEEE Transactions on Communications*, vol. 66, no. 11, pp. 5205–5219, 2018. DOI: 10.1109/TCOMM.2018.2846272.

[74] L. Lu, G. Y. Li, A. L. Swindlehurst, A. Ashikhmin, and R. Zhang, "An overview of massive mimo: Benefits and challenges," *IEEE Journal of Selected Topics in Signal Processing*, vol. 8, no. 5, pp. 742–758, 2014. DOI: 10.1109/JSTSP.2014.2317671.

[75] R. Zhang, Z. Zhong, J. Zhao, B. Li, and K. Wang, "Channel measurement and packet-level modeling for v2i spatial multiplexing uplinks using massive mimo," *IEEE Transactions on Vehicular Technology*, vol. 65, no. 10, pp. 7831–7843, 2016. DOI: 10.1109/TVT.2016.2536627.

[76] D. W. H. Cai, T. Q. S. Quek, C. W. Tan, and S. H. Low, "Max-min sinr coordinated multipoint downlink transmission—duality and algorithms," *IEEE Transactions on Signal Processing*, vol. 60, no. 10, pp. 5384–5395, 2012. DOI: 10.1109/TSP.2012.2208631.

[77] T. Van Chien, E. Björnson, and E. G. Larsson, "Downlink power control for massive mimo cellular systems with optimal user association," in *2016 IEEE International Conference on Communications (ICC)*, 2016, pp. 1–6. DOI: 10.1109/ICC.2016.7510950.

[78] M. Di Renzo, A. Zappone, T. T. Lam, and M. Debbah, "System-level modeling and optimization of the energy efficiency in cellular networks—a stochastic geometry framework," *IEEE Transactions on Wireless Communications*, vol. 17, no. 4, pp. 2539–2556, 2018. DOI: 10.1109/TWC.2018.2797264.

[79] B. Devillers, A. Perez-Neira, and C. Mosquera, "Joint linear precoding and beamforming for the forward link of multi-beam broadband satellite systems," in *2011 IEEE Global Telecommunications Conference - GLOBECOM 2011*, 2011, pp. 1–6. DOI: 10.1109/GLOCOM.2011.6133895.

[80] T. Bai and R. W. Heath, "Coverage and Rate Analysis for Millimeter-Wave Cellular Networks," *IEEE Transactions on Wireless Communications*, vol. 14, no. 2, pp. 1100–1114, Feb. 2015, ISSN: 1558-2248. DOI: 10.1109/TWC.2014.2364267.

[81] T. Maksymyuk, M. Brych, and V. Pelishok, "Stochastic geometry models for 5G heterogeneous mobile networks," *The Smart Computing Review*, pp. 89–101, 2015. DOI: 10.6029/smartcr.2015.02.002. [Online]. Available: https://app.dimensions.ai/details/publication/pub.1073602178.

[82] Q. Gontier, L. Petrillo, F. Rottenberg, F. Horlin, J. Wiart, C. Oestges, and P. De Doncker, "A stochastic geometry approach to emf exposure modeling," *IEEE Access*, vol. 9, pp. 91 777–91 787, 2021. DOI: 10.1109/ACCESS.2021.3091804.

[83] M. Al Hajj, S. Wang, L. Thanh Tu, S. Azzi, and J. Wiart, "A Statistical Estimation of 5G Massive MIMO Networks' Exposure Using Stochastic Geometry in mmWave Bands," *Applied Sciences*, vol. 10, no. 23, p. 8753, 23 Jan. 2020. DOI: 10.3390/app10238753. [Online]. Available: https://www.mdpi.com/2076-3417/10/23/8753 (visited on 01/25/2021).

[84] S. Srinivasa and M. Haenggi, "Distance Distributions in Finite Uniformly Random Networks: Theory and Applications," *IEEE Transactions on Vehicular Technology*, vol. 59, no. 2, pp. 940–949, Feb. 2010, ISSN: 1939-9359. DOI: 10.1109/TVT.2009.2035044.

[85] T. L. Marzetta, *Fundamentals of Massive MIMO*, en. 2016.

[86] H. Q. Ngo, E. G. Larsson, and T. L. Marzetta, "Aspects of favorable propagation in Massive MIMO," in *2014 22nd European Signal Processing Conference (EUSIPCO)*, Sep. 2014, pp. 76–80.

[87] H. Yang and T. L. Marzetta, "Massive MIMO With Max-Min Power Control in Line-of-Sight Propagation Environment," *IEEE Transactions on Communications*, vol. 65, no. 11, pp. 4685–4693, Nov. 2017, ISSN: 1558-0857. DOI: 10.1109/TCOMM.2017.2725262.

[88] H. Yang and T. L. Marzetta, "Massive MIMO in Line-of-Sight Propagation," in *2017 IEEE 85th Vehicular Technology Conference (VTC Spring)*, Jun. 2017, pp. 1–5. DOI: 10.1109/VTCSpring.2017.8108333.

[89] C. A. Balanis, *Antenna Theory: Analysis and Design*, Fourth edition. Hoboken, New Jersey: Wiley, 2016, 1072 pp., ISBN: 978-1-118-64206-1.

[90] M. Loeve, *Probability Theory I*, 4th ed., ser. Graduate Texts in Mathematics, Graduate Texts MathematicsLoeve,M.:Probability Theory. New York: Springer-Verlag, 1977, ISBN: 978-0-387-90210-4. DOI: 10.1007/978-1-4684-9464-8. [Online]. Available: https://www.springer.com/gp/book/9780387902104 (visited on 09/30/2021).

[91] E. W. Weisstein, *Regularized Beta Function*, en, https://mathworld.wolfram.com/RegularizedBetaFunction.html, Text.

[92] M. Haenggi, *Stochastic geometry for wireless networks*. 2009, vol. 9781107014, pp. 1–284, ISBN: 9781139043816. DOI: 10.1017/CBO9781139043816.

ECOLE
DOCTORALE

Titre : Analyse De L'exposition Radio Fréquence Dans Les Systèmes 5G Massive MIMO

Mots clés : Télécommunications, Statistiques, 5G, Massive MIMO, Communication sans fil

Résumé : Cette thèse présente des mesures in-situ d'une antenne massive MIMO et analyse les différents paramètres pertinents pour l'estimation de l'exposition aux CEM dans un réseau 5G. De multiples méthodes sont présentées et discutées pour estimer la puissance reçue dans le réseau tout en se concentrant sur les avantages et les inconvénients de chacune d'elles.
Cette thèse propose également une nouvelle méthode analytique pour étudier l'exposition moyenne, représentée par la puissance totale reçue, dans un réseau 5G massive MIMO dana la bande mmWave. En utilisant la géométrie stochastique, une équation de forme proche de l'exposition est développée et étudiée en adaptant un modèle de canal mmWave utilisant NYUSIM dans des distributions statistiques et en modélisant les BS en tant que PPP. Une analyse de sensibilité est effectuée pour quantifier l'influence des variables d'entrée sur l'exposition.
Un autre modèle de réseau massive MIMO multi-utilisateurs déployant le précodage MRC et le contrôle de puissance max-min fairness est également développé, et où les MTs sont distribués suivant un PPP soit en LoS ou NLoS. Une expression sous forme fermée de l'espérance de la puissance totale reçue et l'expression du rapport entre la puissance totale et le SIR à la MT la plus proche de sa BS de desserte, où l'exposition est la plus élevée. L'exposition moyenne est ensuite étudiée par rapport aux paramètres du réseau en tenant compte des compromis présentés par le modèle de contrôle de puissance et les gains d'antenne. De même, le rapport entre l'exposition et le SIR est également analysé pour étudier l'augmentation de l'exposition par l'augmentation du SIR à la MT la plus proche de sa BS. Et il est montré que plus le nombre d'éléments d'une antenne massive MIMO est élevé, plus elle est efficace en termes de SIR considérant l'exposition produite.

Title : Radio Frequency Exposure Analysis In 5G Massive MIMO Systems

Keywords : Telecommunications, Statistics, 5G, Massive MIMO, Wireless Communications

Abstract : This dissertation presents in-situ measurements of a massive MIMO antenna and analyses the different parameters pertinent to the estimation of the EMF exposure in a 5G network. Multiple methods are presented and discussed to estimate the power received in the network while focusing on the advantages and inconveniences in each of them.
This dissertation also proposes a new analytical method for studying the average exposure, presented by the total power received, in a 5G mmWave massive MIMO network. Using stochastic geometry, a close-form equation of the exposure is developed and studied by fitting a mmWave channel model using NYUSIM into statistical distributions and by modeling the BSs as a PPP. A sensitivity analysis is performed to quantify the influence of the input variables onto the exposure.
Another model for a multi-user massive MIMO network is also developed deploying maximum-ratio combining precoding and max-min fairness downlink power control, and where MTs are distributed following a PPP and can be either LoS or NLoS. A closed-form expression of the expectation of the total power received and the expression of the ratio between the total power and the SIR at the nearest MT to its serving BS, where the exposure is highest. The average exposure is then studied in relation to network parameters taking into account the trade-offs presented by the power control model and antenna gains. Likewise, the ratio between the exposure and SIR is also analyzed to study the increase of exposure per the increase of the SIR at the nearest MT to its BS. And it is shown that the higher the number of antenna elements a massive MIMO antenna has, the more efficient it is in terms of SIR considering the produced exposure.

Institut Polytechnique de Paris
91120 Palaiseau, France